

REPORT DOCUMENTATION PAGE			2		Form Approved OMB NO. 0704-0188	
<p>The public reporting burden for this collection of information is estimated to average 1 hour per response, including the time for reviewing instructions, searching existing data sources, gathering and maintaining the data needed, and completing and reviewing the collection of information. Send comments regarding this burden estimate or any other aspect of this collection of information, including suggestions for reducing this burden, to Washington Headquarters Services, Directorate for Information Operations and Reports, 1215 Jefferson Davis Highway, Suite 1204, Arlington VA, 22202-4302. Respondents should be aware that notwithstanding any other provision of law, no person shall be subject to any penalty for failing to comply with a collection of information if it does not display a currently valid OMB control number.</p> <p>PLEASE DO NOT RETURN YOUR FORM TO THE ABOVE ADDRESS.</p>						
1. REPORT DATE (DD-MM-YYYY) 31-07-2014		2. REPORT TYPE Ph.D. Dissertation		3. DATES COVERED (From - To) -		
4. TITLE AND SUBTITLE Application of optical forces in microhptonic systems				5a. CONTRACT NUMBER W911NF-09-1-0473		
				5b. GRANT NUMBER		
				5c. PROGRAM ELEMENT NUMBER 611102		
6. AUTHORS Jing Ma				5d. PROJECT NUMBER		
				5e. TASK NUMBER		
				5f. WORK UNIT NUMBER		
7. PERFORMING ORGANIZATION NAMES AND ADDRESSES University of Southern California Contracts and Grants 3720 S. Flower Street Los Angeles, CA 90089 -0701				8. PERFORMING ORGANIZATION REPORT NUMBER		
9. SPONSORING/MONITORING AGENCY NAME(S) AND ADDRESS (ES) U.S. Army Research Office P.O. Box 12211 Research Triangle Park, NC 27709-2211				10. SPONSOR/MONITOR'S ACRONYM(S) ARO		
				11. SPONSOR/MONITOR'S REPORT NUMBER(S) 56801-MS-PCS.12		
12. DISTRIBUTION AVAILABILITY STATEMENT Approved for public release; distribution is unlimited.						
13. SUPPLEMENTARY NOTES The views, opinions and/or findings contained in this report are those of the author(s) and should not contrued as an official Department of the Army position, policy or decision, unless so designated by other documentation.						
14. ABSTRACT Optical forces represent an exciting new approach for manipulating microphotonic devices. In this thesis, the overall goal is to invent and demonstrate novel microphotonic device functionalities based on optical forces. There are two major tasks. One is to explore how optical forces can be used to achieve highly tunable, on-chip photonic devices. The other task is to utilize optical forces for light assisted, template self-assembly of nanoparticles.						
15. SUBJECT TERMS optical forces, microphotonics, optomechanics, optical trapping, light-assisted self assembly						
16. SECURITY CLASSIFICATION OF:			17. LIMITATION OF ABSTRACT	15. NUMBER OF PAGES	19a. NAME OF RESPONSIBLE PERSON	
a. REPORT	b. ABSTRACT	c. THIS PAGE			Michelle Povinelli	
UU	UU	UU	UU		19b. TELEPHONE NUMBER 213-740-8682	

Report Title

Application of optical forces in microhptonic systems

ABSTRACT

Optical forces represent an exciting new approach for manipulating microphotonic devices. In this thesis, the overall goal is to invent and demonstrate novel microphotonic device functionalities based on optical forces. There are two major tasks. One is to explore how optical forces can be used to achieve highly tunable, on-chip photonic devices. The other task is to utilize optical forces for light assisted, template self-assembly of nanoparticles.

Optical forces are numerically investigated in different configurations. Attractive forces exist between a suspended one-dimensional periodic photonic crystal waveguide and underlying substrate in a silicon-on-insulator platform. It is shown that the optical force can be enhanced by designing the waveguide cross section to make the mode approach the band edge or substrate light line. For periodic waveguides, the optical force is non-monotonic with waveguide-substrate separation. This effect may enable the design of compact, integrated optical power limiters. An analytical method is proposed to calculate optical forces between silicon waveguides based on the perturbation of effective index at fixed frequency. The method is used to investigate the mechanical Kerr effect in a coupled-waveguide system with bipolar forces. It is shown that positive mechanical Kerr coefficient results from either an attractive or repulsive force. An enhanced mechanical Kerr coefficient several orders of magnitude larger than the intrinsic Kerr coefficient is obtained in waveguides for which the optical mode approaches the air light line, given appropriate design of the waveguide dimensions.

Optical forces are proposed to tune phase and group birefringence in parallel silicon strip waveguides. Widely tunable phase and group birefringence can be achieved by varying the pump power, with maximum values of 0.026 and 0.13, respectively. The giant phase birefringence allows linear to circular polarization conversion within 30 μm for a pump power of 67 mW. The group birefringence gives a tunable differential group delay of 6 fs between orthogonal polarizations.

A novel photonic crystal lattice is proposed for assembling a two-dimensional array of particles by optical forces with low power. The lattice is created by introducing a rectangular slot in each unit cell of the Suzuki-Phase lattice to enhance the light confinement of guided resonance modes. Large quality factors on the order of 10^5 are predicted in the lattice. A significant decrease of the optical power required for optical trapping can be achieved compared to the previous design based on square lattice. Experiments are carried out to optically characterize the high-Q guided resonance modes with slot confinement. The evolution of the measured wavelengths and quality factors follows the trend predicted by the simulations.

The intrinsic, radiation loss of a coupled resonator optical waveguide (CROW) is studied by the tight binding approximation (TBA). The TBA predicts that the quality factor of the CROW increases with that of the isolated cavity. The results provide a method to design CROWs with low intrinsic loss across the entire waveguide band. The method may facilitate the design of large-area, coupled-cavity modes with high quality factor that nevertheless couple to normally-incident radiation for assembly.

APPLICATION OF OPTICAL FORCES IN MICROPHOTONIC SYSTEMS

by

Jing (Maggie) Ma

A Dissertation Presented to the
FACULTY OF THE GRADUATE SCHOOL
UNIVERSITY OF SOUTHERN CALIFORNIA
In Partial Fulfillment of the
Requirements for the Degree
DOCTOR OF PHILOSOPHY
(ELECTRICAL ENGINEERING)

May 2013

Copyright 2013

Jing (Maggie) Ma

Dedication

To my family, Jian Ma, Xiaoxia Tong, and Xiaoyang Wang

For the greatest support with love, encouragement, and trust

Acknowledgements

I would like to express my deepest gratitude to my advisor, Professor Michelle Povinelli, for supporting me with knowledge, patience and encouragement during my Ph.D study. Other than technical insight, she has taught me personal lessons which will be very important in my professional career. I have spent the last five years, a highlight of my life, in her group on exploring fascinating topics of science. Thanks for giving me such a great time!

My work would have not been possible without the help provided by my fellow Nanophotonics Group members — Luis Javier Martínez, who collaborated with me on designing and demonstrating novel devices for lower-power optical trapping; Eric Jaquay, who trained me for multiple equipments in USC cleanroom; Chenxi Lin, who helped with simulations and experimental setup; Ningfeng Huang, who put in effort with improving simulation algorithms and software; Camilo Mejia, who provided great insight on modeling; Roshni Biswas, who helped with scientific software; Duke Anderson, who helped with my English writing.

I also would like to thank members of the CSL, especially Tingwei Yeh, Yunchu Li, and Lawrence Stewart. I would like to thank Prof. Wu for helpful discussion on device fabrication, Prof. Steier, Prof. Dapkus, Prof. Cronin, and Prof. Armani who participated on my qualifying committees.

Last but not least, I would like to express my deepest love to my family — my husband Xiaoyang Wang, my parents Xiaoxia Tong and Jian Ma, for their love, trust, and support on my inclination towards science.

Table of Contents

DEDICATION	i
ACKNOWLEDGEMENTS	ii
LIST OF FIGURES	vi
ABSTRACT	xii
 CHAPTER 1 INTRODUCTION	 1
1.1 Background	1
1.2 Optical Forces in Microphotonic Systems.....	2
1.2.1 Early Experiments	4
1.2.2 Other Configurations.....	5
1.3 Applications for On-chip Manipulation of Light Signals.....	10
1.3.1 Tunable Directional Coupler.....	11
1.3.2 Wavelength Filtering	12
1.3.3 Self-adaptive Microcavity.....	14
1.3.4 Slow Light	15
1.3.5 Tunable lasers.....	16
1.3.6 Our Contributions.....	17
1.4 Applications for Assembly of Nanoparticles.....	18
1.5 Force Calculation.....	22
1.5.1 Maxwell Stress Tensor.....	22
1.5.2 Derivative Method.....	23
1.6 Thesis Overview.....	25
1.7 Chapter References.....	27
 CHAPTER 2 EFFECT OF PERIODICITY ON OPTICAL FORCES..	 35
2.1 Background.....	35
2.2 Band Edge Effects	36
2.3 Potential Application.....	41
2.4 Chapter References.....	41
 CHAPTER 3 MECHANICAL KERR NONLINEARITY	 45
3.1 Background.....	45
3.2 Coupled Waveguides Exhibiting Bipolar Optical Forces.....	46
3.3 Calculation of Optical Force.....	48
3.4 Calculation of Mechanical Kerr Coefficient.....	51
3.5 Symmetric Mode	54

3.6	Antisymmetric Mode	56
3.7	Discussion.....	57
3.8	Summary.....	59
3.9	Chapter References.....	60
 CHAPTER 4 LARGE TUNING OF BIREFRINGENCE		62
4.1	Background.....	62
4.2	Design Method.....	65
4.3	Tunable Phase Birefringence.....	70
4.3.1	Tunable Relative Phase-shift.....	71
4.3.2	Other tuning configurations.....	73
4.4	Tunable Group Birefringence.....	74
4.5	Thermal Effects	76
4.6	Summary.....	78
4.7	Chapter References.....	79
 CHAPTER 5 TRAPPING IN A SLOT-SUZUKI-PHASE LATTICE...		82
5.1	Background.....	82
5.2	Structure Design.....	83
5.3	Optical Forces.....	89
5.4	Summary	95
5.5	Chapter References.....	95
 CHAPTER 6 CHARACTERIZATION OF HIGH-Q SLOT MODES....		99
6.1	Background.....	99
6.2	Structure Design.....	100
6.3	Fabrication and Optical Characterization.....	104
6.4	Summary.....	109
6.5	Chapter References.....	109
 CHAPTER 7 RADIATION LOSS IN PHOTONIC CRYSTAL CROW		112
7.1	Background.....	112
7.2	Theoretical Formulation in the Tight-binding Approximation.....	114
7.2.1	Light Line Picture	116
7.2.2	Tight-binding Approximation	118
7.3	Numerical Validation of the Tight Binding Approximation.....	121
7.4	Factors Influencing the CROW Quality Factor.....	126

7.5	Summary.....	128
7.6	Chapter References.....	129
 BIBLIOGRAPHY		133
 APPENDIX		146

List of Figures

Figure 1-1	Optical forces between parallel waveguides. (a) schematic structure; multicolored arrow indicates the direction of light propagation. (b) calculated, normalized, optical force as a function of waveguide separation. Insets show modal profiles, with red/blue indicating positive/negative values of the electric field component parallel to the air gap	3
Figure 1-2	Optical forces (a) between waveguide and substrate, and (b) between vertically-stacked microrings. Light is coupled into the rings by a bus waveguide. For both (a) and (b), the structure is shown on top, with a multicolored arrow labeling the direction of light propagation. The modal profiles are shown on the bottom, with red/blue indicating positive/negative values of the electric field component perpendicular to the air gap. Yellow arrows show the direction of the optical force. The system in (a) has an attractive mode only, whereas (b) has both symmetric (attractive) and anti-symmetric (repulsive) modes	4
Figure 1-3	Schematic of photonic crystal cavities showing opto-mechanical coupling. (a) “zipper” cavity, (b) nanobeam cavity, and (c) double-layer photonic crystal slab cavities. In (a) and (b), the lattice constant near the center of the device is decreased slightly (not shown) to form a microcavity.....	5
Figure 1-4	Guided-resonance optomechanical devices: (a) double-layer photonic crystal slab supporting guided resonances, and (b) asymmetric guided resonant structure composed of photonic crystal slab and silicon-silica substrate.....	7
Figure 1-5	Optical forces generated in plasmonic devices: (a) finite-thickness metal waveguides separated by a dielectric gap, (b) semi-infinite metal plates separated by a dielectric gap, and (c) a hybrid plasmonic system with a dielectric waveguide and a metallic substrate.....	9
Figure 1-6	Optically-tunable directional coupler, in which the effective index of each arm is tuned via an adjustable slot width.	12
Figure 1-7	Schematic design of a self-tuning resonator.....	14
Figure 1-8	Schematic of light-assisted, templated self-assembly. Incident light from below excites a guided-resonance mode of a photonic-crystal slab, giving rise to optical forces on nanoparticles in solution. Under the influence of the forces, the nanoparticles self assemble into	

	regular, crystalline patterns	19
Figure 1-9	Light-assisted, templated self-assembly of 520 nm diameter particles above a photonic-crystal slab. (a–c) Sequential snapshots taken with the light beam on. (d) Snapshot taken after the beam is turned off.....	21
Figure 2-1	(a) Patterned, 1D-periodic photonic crystal Si waveguide with period a is separated from the SiO_2 substrate by a distance $d = 100$ nm. r is the hole radius. (b) Dispersion relation for TM (blue solid curve) and TE (red dashed curve) modes in waveguide with $r = 0.3a$, and $h = w = a$. The gray region shows the substrate light cone. The point where the TE/TM mode crosses the light line is indicated by an orange/yellow circle.....	37
Figure 2-2	The attractive force per length per unit power as a function of period a for (a) TM and (b) TE modes at wavelength $\lambda = 1550$ nm. One period of the waveguide (wv.) is a cube of side length a with a circular air hole of radius $r = 0.3a$. The separation d between the suspended waveguide and substrate is 100 nm.....	38
Figure 2-3	The attractive force per length per unit power as a function of distance d for (a) TM and (b) TE modes at wavelength $\lambda = 1550$ nm...	40
Figure 3-1	(a) Two coupled silicon waveguides, each with cross section $w \times h$, separated by a distance d and resting on a SiO_2 substrate with suspended length L . (b) Dispersion relation for modes of the suspended section. The two lowest modes with electric field vectors primarily in the z -direction are plotted for separations $d = 100$ nm and $d = 1000$ nm. The cross section of each waveguide is 350×350 nm ² . The gray region shows the light cone for air.....	47
Figure 3-2	Schematic diagram showing a shift in the dispersion relation due to a change in separation between waveguides d . The solid and dashed lines represent the initial and shifted dispersion relation, respectively.....	48
Figure 3-3	For fixed wavelength 1550 nm and waveguide dimensions $h = w = 350$ nm: (a) Symmetric mode: n_{eff} as a function of d (black curve); $F/(LP)$ calculated by the MST method (red curve) and by Equation (3-8) (red triangles). (b) Antisymmetric mode: n_{eff} as a function of d (black curve); $F/(LP)$ calculated by the MST method (red curve) and by Equation (3-8) (red triangles).....	51
Figure 3-4	Symmetric mode: (a) Band structure. The gray region represents the air light cone. The red line shows fixed wavelength 1550 nm (frequency 193.55 THz). (b) Attractive force per length per unit	

- power $F/(LP)$. The initial separation $d=100$ nm, suspended length $L=20$ μm , optical power $P = 10$ mW, and the signal wavelength is 1550 nm. (c) Mechanical Kerr coefficient n_2^m 54
- Figure 3-5 Anti-symmetric mode: (a) Band structure. The gray region represents the air light cone. The red line shows fixed wavelength 1550 nm (frequency 193.55 THz). (b) Repulsive force per length per unit power $F/(LP)$. The initial separation $d=100$ nm, suspended length $L = 20$ μm , optical power $P = 10$ mW, and the signal wavelength is 1550 nm. (c) Mechanical Kerr coefficient n_2^m 57
- Figure 4-1 (a) Two coupled Si waveguides, each with cross section $w \times h$ separated by a distance d , rest on a SiO_2 substrate with a free-standing section of length L . (b) Dispersion relation for the lowest-frequency TE mode (solid lines) and TM mode (dashed lines) of the coupled waveguides for several separations. Insets respectively show the E_y field distribution of the TE mode and the E_z field distribution of the TM mode with $d=0.2a$ at frequency $\omega a/2\pi c=0.18$ (darker shades correspond to larger magnitudes of the electric field at a snapshot in time). The yellow region shows the light cone..... 66
- Figure 4-2 (a) Normalized force per unit area for the lowest-frequency TE (red) and TM (black) modes as a function of pump light frequency, at fixed separation $d=0.35a$. (b) Force per unit area as a function of separation (red triangles), at optimized frequency $\omega_p a/2\pi c=a/\lambda_p=0.165$. The right and top axes are in physical units with incident power $P=20$ mW, $w=h=a=263.5$ nm, and $L=30$ μm . The blue solid line is the second-order polynomial fit of the force per unit area..... 68
- Figure 4-3 Displacement of the suspended section of each waveguide as a function of position along the waveguide. The cross-sectional dimension is $w=h=a=263.5\text{nm}$, the initial waveguide separation is $d=0.35a=92.2$ nm, the pump frequency is $\omega_p a/2\pi c=a/\lambda_p=0.165$, the incident power is $P=20$ mW, and the suspended length is $L=30$ μm . Note that the x and y axes differ in scale..... 70
- Figure 4-4 (a) Phase birefringence Δn_p as a function of signal frequency in the coupled waveguides with varying separations. The arrow shows that at a frequency $\omega_s a/2\pi c=0.17$, the absolute value of Δn_p increases as the waveguide separation d decreases. (b) Phase birefringence Δn_p as a function of position along the waveguides. The initial separation is $d=0.35a=92.2$ nm. The attractive force is induced by CW pump light at frequency $\omega_p a/2\pi c=a/\lambda_p=0.165$ and power $P=20$ mW. The difference between the maximum and the minimum of Δn_p is 0.026..

		71
Figure 4-6	Tuning the relative phase shift by increasing CW pump power from 20 mW to 70 mW (black squares). The waveguide length is 23.05 μm . The red line is a 2 nd -order polynomial fit of the phase shift. A power of approximately 67 mW yields a 0.5π phase difference.....	73
Figure 4-6	Phase birefringence Δn_p as a function of signal frequency in the two-waveguide system with varying separations. (a) The cross section of each waveguide is $a \times 2a$. The arrow shows that Δn_p decreases with decreasing separation. (b) The cross section of each waveguide is $a \times 0.5a$. The absolute value of Δn_p increases with decreasing separation.....	74
Figure 4-7	(a) Group birefringence Δn_g as a function of signal frequency, in the coupled waveguides with varying separations. The arrow shows that as the waveguide separation d increases, the group birefringence Δn_g increases fastest at a frequency $\omega_s a / 2\pi c = 0.17$. (b) Group birefringence Δn_g as a function of position along the waveguides. The waveguides are deformed by an attractive force induced by a CW pump at frequency $\omega_p a / 2\pi c = a / \lambda_p = 0.165$, with a power $P = 20$ mW. The difference between the maximum and the minimum of Δn_g is 0.13.....	75
Figure 5-1	(a) Diagram of the Suzuki-Phase photonic crystal lattice. (b) Normalized transmission spectra calculated by the transfer-matrix method. Red line for x -polarization, blue for y -polarization. (c) H_z -field profile (left) and E^2 (right) of $o1$ resonance. d) H_z -field profile (left) and E^2 (right) of $e2$ resonance.....	84
Figure 5-2	(a) Diagram of the Slot-Suzuki-phase hybrid lattice. (b) Normalized transmission spectra. Red line for x -polarization, blue for y -polarization. (c) H_z -field profile of $se2$ resonance. d) E^2 field profile of $se2$ resonance.....	86
Figure 5-3	(a) Evolution of the Q and wavelength λ_R as a function of slot width w_y . b) Evolution of the Q and wavelength λ_R as a function of slot length w_x . Red color indicates Q; blue color indicates wavelength. Dots correspond to calculated values; lines represent a guide for the eye.....	88
Figure 5-4	(a) Optical force F_z as a function of slot width w_y for four different particle radii. The slot length w_x is fixed to 464 nm. (b) Optical force F_z as a function of particle radius. Dots represent the calculated values. Lines represent a guide for the eye. In both (a) and (b), the particle is at $(x = 0, y = 0)$ and has its bottom edge 45 nm above the top surface of the slab.....	91

Figure 5-5	(a) Diagram of the Slot Suzuki-phase (SSP) lattice with a particle above. (b) Vertical force F_z as a function of particle position in the XY plane. (c) In-plane force F_{xy} as a function of position in the XY plane. The force magnitude is indicated by the colormap, and the force direction is shown by the blue arrows. (d) Potential map in the XY plane. To obtain the results shown in (b), (c), and (d), we assume that the particle has a radius of 25 nm and is placed such that its bottom edge is 45 nm above the top surface of the slab.....	93
Figure 5-6	(a) In-plane optical force F_{xz} for a particle with radius of 25 nm. (b) Optical potential map for the particle.....	94
Figure 6-1	(a) Diagram of the graphite photonic crystal lattice. (b) Diagram of the Slot-graphite photonic crystal lattice. The arrows represent the primitive vectors of the Bravais lattice.....	101
Figure 6-2	(a) Photonic band structure of the Graphite photonic crystal lattice. (b) Photonic band structure of the Slot-graphite photonic crystal lattice. The highlighted region represents the targeted bands. (c) H_z -field profile (left) and E^2 (right) profile of the fifth band (down) and fourth band (up) of the graphite photonic crystal lattice. (d) H_z -field profile (left) and E^2 (right) profile of the fourth band (down) and fifth band (up) of the Slot-graphite photonic crystal lattice.....	102
Figure 6-3	(a): Evolution of the Q and wavelength as function of w_y . (b): Evolution of the Q and wavelength as function of w_x . Red color for Q. Black for wavelength. Dots: Corresponds to the calculate values. Lines represents a guide for the eye.....	104
Figure 6-4	SEM image of one fabricated Slot-graphite device.....	105
Figure 6-5	(a) Diagram of experimental setup used to characterize the optical properties of the guided resonant device. Two cross polarizers (PC) are applied before and after the device to cancel out Fabry-Perot noise. TL: tunable laser; MO: microscope objective; LS: lens; TS: translation stage; PD: photodiode. (b) One measured spectrum. The right transmission peak correspond to the slot mode, and the left peak shows the dipole mode with lower Q-factor.....	107
Figure 6-6	(a): Evolution of the Q factor as function of w_y . (b): Evolution of the wavelength as function w_y . Black spheres for experimental data. Gray dashed curves for simulation. Blue stars for experimental data when w_y is increased by 10% by considering SEM system errors.....	108
Figure 7-1	(a) Schematic diagram of CROW structure L2S3. (b) Dispersion	

	curve of CROW mode in L2S2 (red), L2S3 (blue) and L2S4 (magenta). Dashed line shows the fundamental mode of the isolated L2 cavity.....	115
Figure 7-2	(a) Schematic picture of tight-binding prediction for the power spectrum of a CROW mode. (b) CROW power spectrum giving a large value of $Q(k)$ compared to the isolated cavity. (c) CROW Power spectrum giving a small value of $Q(k)$ compared to the isolated cavity.....	119
Figure 7-3	(a) Mode distribution of the real part of E_y on the x - y plane $0.2a$ above the surface of the isolated L2 cavity. (b) Power spectrum of L2 cavity. The blue circle is the light cone. (c) Power spectrum of CROW mode in L2S3 structure with $k = 0$. (d) Visual test of tight-binding approximation via comparison of CROW power spectra to that of isolated L2 cavity. The blue dashed lines indicate light lines...	122
Figure 7-4	$Q(k)$ for L2 CROWs with varying cavity separations: (a) L2S2, (b) L2S3, and (c) L2S4. Dots represent calculated values. Lines represent guides for the eye.....	125
Figure 7-5	(a) Quality factor for CROWs based on different constituent cavities. Triangles indicate $Q(0)$; circles indicate $Q(k_{Bz})$. Dashed lines show Q for single cavity. Calculations are performed using the TBA method. (b) $Q(k)$ for CROWs designed with a number of separation holes equal to the first node in (a).....	128

Abstract

Optical forces represent an exciting new approach for manipulating microphotonic devices. In this thesis, the overall goal is to invent and demonstrate novel microphotonic device functionalities based on optical forces. There are two major tasks. One is to explore how optical forces can be used to achieve highly tunable, on-chip photonic devices. The other task is to utilize optical forces for light-assisted, template self-assembly of nanoparticles.

Optical forces are numerically investigated in different configurations. Attractive forces exist between a suspended one-dimensional periodic photonic crystal waveguide and underlying substrate in a silicon-on-insulator platform. It is shown that the optical force can be enhanced by designing the waveguide cross section to make the mode approach the band edge or substrate light line. For periodic waveguides, the optical force is non-monotonic with waveguide-substrate separation. This effect may enable the design of compact, integrated optical power limiters.

An analytical method is proposed to calculate optical forces between silicon waveguides based on the perturbation of effective index at fixed frequency. The method is used to investigate the mechanical Kerr effect in a coupled-waveguide system with bipolar forces. It is shown that positive mechanical Kerr coefficient results from either an attractive or repulsive force. An enhanced mechanical Kerr coefficient several orders of magnitude larger than the intrinsic Kerr coefficient is

obtained in waveguides for which the optical mode approaches the air light line, given appropriate design of the waveguide dimensions.

Optical forces are proposed to tune phase and group birefringence in parallel silicon strip waveguides. Widely tunable phase and group birefringence can be achieved by varying the pump power, with maximum values of 0.026 and 0.13, respectively. The giant phase birefringence allows linear to circular polarization conversion within 30 μm for a pump power of 67 mW. The group birefringence gives a tunable differential group delay of 6 fs between orthogonal polarizations.

A novel photonic crystal lattice is proposed for assembling a two-dimensional array of particles by optical forces with low power. The lattice is created by introducing a rectangular slot in each unit cell of the Suzuki-Phase lattice to enhance the light confinement of guided resonance modes. Large quality factors on the order of 10^5 are predicted in the lattice. A significant decrease of the optical power required for optical trapping can be achieved compared to the previous design based on square lattice. Experiments are carried out to optically characterize the high-Q guided resonance modes with slot confinement. The evolution of the measured wavelengths and quality factors follows the trend predicted by the simulations.

The intrinsic, radiation loss of a coupled resonator optical waveguide (CROW) is studied by the tight binding approximation (TBA). The TBA predicts that the quality factor of the CROW increases with that of the isolated cavity. The results provide a method to design CROWs with low intrinsic loss across the entire waveguide band.

The method may facilitate the design of large-area, coupled-cavity modes with high quality factor that nevertheless couple to normally-incident radiation for assembly.

Chapter 1: Introduction

1.1 Background

It has long been known that light can exert a force on objects, an effect known as radiation pressure. Back in the 16th century, it was suggested that mechanical effects from solar radiation cause comet tails to point away from the sun. In 2010, Japanese Aerospace Exploration Agency successfully launched a spacecraft with radiation pressure from sunlight as propulsion force.

Under most everyday circumstances, optical forces are too weak to cause noticeable effects. For nano- and micro-scale objects, however, optical forces can have significant effects. One well-known application of optical forces is optical trapping [1, 2], a technique that uses laser light to trap and position small particles. The objective of this thesis is to explore the applications of optical forces in nano- and micro-scale region.

Dr. Povinelli [3] has introduced the idea of using optical forces to precisely control the positions of microscale optical waveguides and resonators. Optical waveguides, which act like “photonic wires,” and microresonators, devices that confine light to the scale of the wavelength, are important elements for developing photonic integrated circuits [4-6]. Ultimately, photonic integrated circuits may manipulate photons in the way that electronic circuits manipulate electrons. The development of photonic circuits that can filter, buffer, and reroute optical signals is expected to transform optical communications [7], enable high-speed optical interconnects between multi-chip computer processors [8], and provide a platform for quantum communication [9]. However, current photonic circuits are largely static; methods for reconfiguring their response are limited. Optical forces in integrated photonics, or optomechanical effects, represent

an exciting new approach for achieving flexible, all-optical tuning and reconfiguration of on-chip microphotonic devices.

1.2 Optical Forces in Microphotonic Systems

In 2005, Povinelli *et al.* theoretically investigated the optical forces between parallel waveguides [3], shown in Figure 1-1 (a). A mechanical force arises from the overlap of the guided waves propagating in the two waveguides. The sign of the force can be either attractive or repulsive, depending on the relative phase of light in the waveguides. The “bonding” mode, which is symmetric with respect to the two waveguides, gives an attractive optical force, whereas the “anti-bonding,” or anti-symmetric mode, is repulsive. By controlling which mode is input into the waveguides, input light can be used to pull the waveguides together or push them apart. Physically, the force originates from the interaction of dipoles induced in the dielectric waveguides by the electromagnetic field of the light wave. The optical force scales linearly with input power.

The calculated optical force in a typical system is shown in Figure 1-1 (b). The waveguides each have cross sections of 310 nm by 310 nm, and the wavelength in air is 1550 nm. In the figure, the force per unit length of the waveguide is divided by the input power and plotted as a function of waveguide separation. For waveguide separations larger than ~60 nm, the symmetric and antisymmetric modes correspond to attractive (positive sign) and repulsive (negative sign) forces, respectively. The magnitude of the optical force decays monotonically with increasing separation. The decay is due to reduced optical coupling between the waveguides, that is, reduced overlap between the evanescent tails of the individual waveguide modes. For smaller

waveguide separations, strong coupling between the waveguides can significantly perturb the individual waveguide modes. In this regime, the optical force of the antisymmetric mode changes sign.

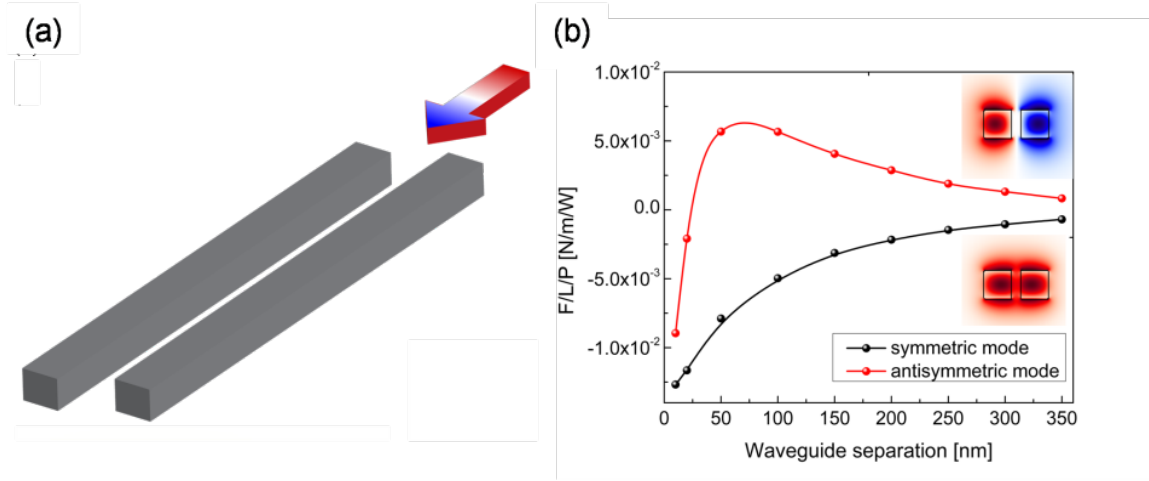


Figure 1-1 Optical forces between parallel waveguides. (a) schematic structure; multicolored arrow indicates the direction of light propagation. (b) calculated, normalized, optical force as a function of waveguide separation. Insets show modal profiles, with red/blue indicating positive/negative values of the electric field component parallel to the air gap.

In Figure 1-1 (b), it can be seen that for the symmetric (attractive) mode, the optical force increases with decreasing gap. However, if the gap is too small, the Casimir force becomes comparable to, or larger than, the optical force [10]. Devices with gaps as small as ~ 80 nm have been used in experiments [11].

Interestingly, the optical force between waveguides is in a direction *perpendicular* to the direction of light propagation. This is different than the traditional case of radiation pressure, where the optical force on a surface is parallel to the direction of light propagation. The radiation

pressure can be simply derived from momentum conservation arguments: reflection of a photon from a surface must correspond to transfer of mechanical momentum to the surface. Similarly, the optical force on the mirrors of a Fabry-Perot cavity acts perpendicular to the direction of light propagation [12]. For parallel waveguides, the situation is notably different: the momentum acquired by each individual waveguide is perpendicular to the propagation direction, and the momenta of the two waveguides are equal and opposite.

1.2.1 Early Experiments

Initial theoretical work on optical forces was followed rapidly by experimental demonstrations.

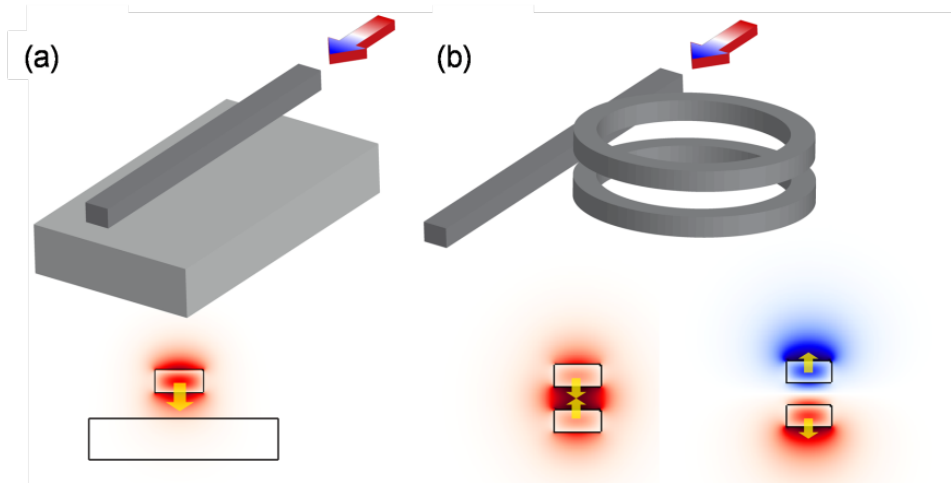


Figure 1-2 Optical forces (a) between waveguide and substrate, and (b) between vertically-stacked microrings. Light is coupled into the rings by a bus waveguide. For both (a) and (b), the structure is shown on top, with a multicolored arrow labeling the direction of light propagation. The modal profiles are shown on the bottom, with red/blue indicating positive/negative values of the electric field component perpendicular to the air gap. Yellow arrows show the direction of the optical force. The system in (a) has an attractive mode only, whereas (b) has both symmetric (attractive) and anti-symmetric (repulsive) modes.

In 2008, a suspended waveguide coupled to an underlying substrate was designed [13] and fabricated [14] by Li *et al.* A schematic is shown in Figure 1-2 (a). The authors demonstrated an attractive optical force that is induced by the overlap between the evanescent tail of waveguide mode and the underlying oxide substrate. Waveguide displacement was inferred from the optical transmission using an on-chip interferometer scheme. Further experiments demonstrated attractive and repulsive forces in coupled microresonators, shown in Figure 1-2 (b).

1.2.2 Other Configurations

Following initial work on waveguide and microresonator systems, a variety of alternate microphotonic device geometries have been investigated. Various mechanisms have been studied for enhancing the optical force. These include tailoring the overlap between photonic and mechanical modes, exploiting guided resonance modes, and incorporating plasmonic materials.

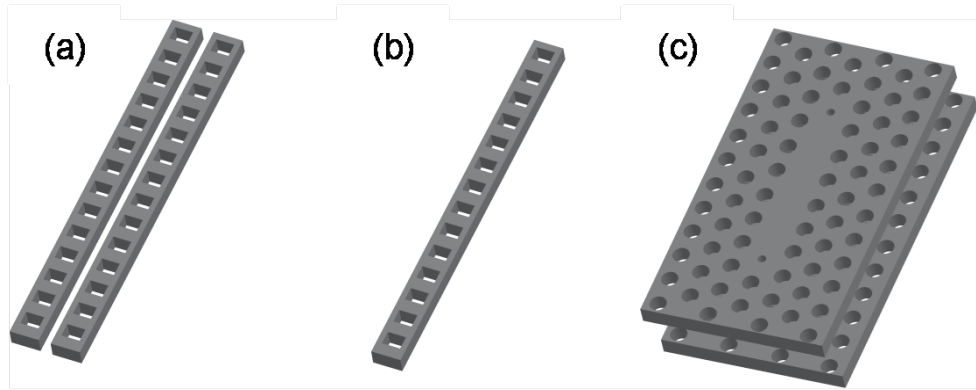


Figure 1-3 Schematic of photonic crystal cavities showing opto-mechanical coupling. (a) “zipper” cavity, (b) nanobeam cavity, and (c) double-layer photonic crystal slab cavities. In (a) and (b), the lattice constant near the center of the device is decreased slightly (not shown) to form a microcavity.

Photonic-crystal microcavities can be designed to confine light in ultra-small mode volumes and exhibit high optical quality factors, Q [15-18]. Recent work has exploited these attributes to achieve strong optomechanical effects. Painter and co-workers [19, 20] have designed and experimentally demonstrated a “zipper” system with large optomechanical coupling. The zipper is made up of two parallel, patterned nanobeams (shown in Figure 1-3 (a)) each of which is designed to support an optical microcavity mode. Coupling between the modes gives rise to attractive and repulsive forces. A relevant figure of merit in the structure is the optomechanical coupling length, $L_{OM} = \omega / g_{OM}$, where ω is the optical resonance frequency. Experimental values lower than 3 microns were obtained.

In this system, optomechanical coupling results in an “optical spring effect:” due to the presence of optical forces, the mechanical resonance frequency and spring constant are shifted. In experiments, a modified stiffness of five times the intrinsic mechanical stiffness of the nanobeam was observed.

In Reference [21], Painter and co-workers designed and experimentally demonstrated a nanobeam structure (in Figure 1-3 (b)) that confines *both* the optical modes and the mechanical vibration modes to the scale of the optical wavelength. Localized mechanical modes are created using a *phononic* band gap microcavity, analogous to the optical case. The authors suggest that the strong optomechanical coupling between optical modes (200 THz optical resonance frequency) and high-frequency mechanical modes (2 GHz mechanical resonance frequency) will allow extremely sensitive mass detection via optical readout.

Notomi and coworkers have theoretically analyzed microcavities in parallel photonic-crystal slabs [22]. A schematic double-layer cavity is shown in Figure 1-3 (c). Intriguingly, the authors

suggest that if the mechanical displacement between the structures occurs faster than the response time of the optical cavity (proportional to the optical period times the optical Q), wavelength conversion will occur [23]. This phenomenon is analogous to the frequency shifts predicted and measured in microphotonic systems with time-varying linear refractive index [24, 25].

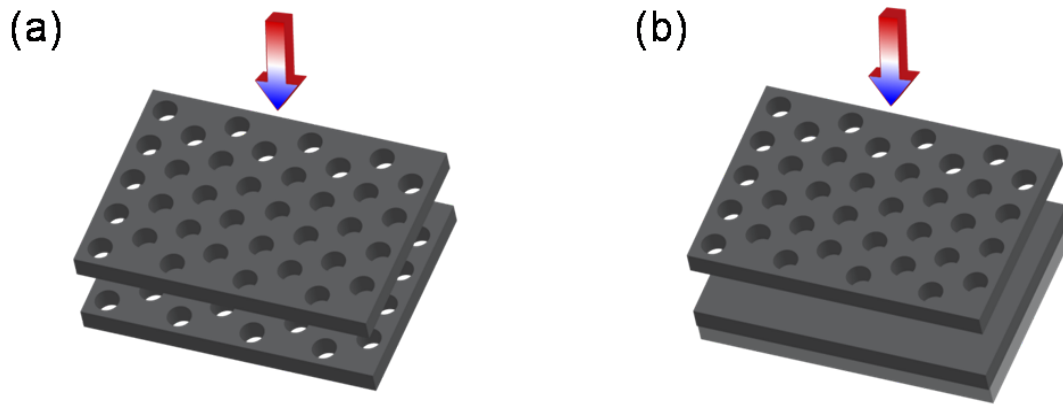


Figure 1-4 Guided-resonance optomechanical devices: (a) double-layer photonic crystal slab supporting guided resonances, and (b) asymmetric guided resonant structure composed of photonic crystal slab and silicon-silica substrate.

Other than microcavities, optical forces have been demonstrated in guided resonance systems. When light is normally incident upon a 1D- or 2D-periodically patterned slab, it can excite *guided resonance modes*, which propagate in the plane of the slab while leaking partially to the surrounding air [26]. Early work examined forces between identical, parallel photonic-crystal slabs (Figure 1-4 (a)). Liu *et al.* [27] showed theoretically that optical forces are enhanced near guided resonances. In an ideal system, infinite- Q resonances, or “dark states” can be designed, and the force will diverge as $1/Q$ near the resonant frequency. Experiments on a similar system were reported by Roh *et al.* [28]. Changes in separation between the slabs due to optical forces

were inferred from the optical reflection spectrum. Displacements of approximately 3.6 nm were obtained for ~ 20 mW of power. The force per photon, 0.051 pN/photon, was similar to values obtained in double-layer disk cavities [29] and zipper cavities [20].

Rodriguez *et al.* [30] have theoretically studied asymmetric systems consisting of a photonic-crystal slab above an unpatterned, layered substrate, shown in Figure 1-4 (b). This system may offer advantages in terms of fabrication. The asymmetric system supports both quasi-symmetric and quasi-antisymmetric modes with opposite signs of the force. As for symmetric structures, the sign of the force can be changed by tuning the frequency of the incident light. Assuming the photonic-crystal slab can move, changing the separation between slab and substrate, bistable behavior is predicted [31]. The precise conditions for bistability are affected by the Casimir force, suggesting that observations of bistability could be used to infer the magnitude of the Casimir force. In addition, the optical force might be used as a way of controlling or preventing stiction, which results from Casimir attraction.

One advantage of such guided-resonant devices is that light can be coupled into the mode at normal incidence using free-space optics, potentially allowing ease of alignment. However, the mass of guided-resonant slabs is usually bigger than that of photonic crystal cavity devices, which may reduce the mechanical resonance frequency and hence increase the characteristic response time for an optical force.

Surface Plasmon Polaritons (SPP's) are propagating electromagnetic modes formed at metallic-dielectric interfaces [32] that offer the ability to confine light to the deep subwavelength scale. There has been interest in determining whether the enhanced light intensity in SPP can be exploited to yield large optical forces. Woolf *et al.* [33] have theoretically analyzed the forces

generated by SPP's between metal slabs. They determined that semi-infinite metal waveguides separated by an air gap (MIM geometry as shown by Figure 1-5 (a)) give rise to an attractive force, while finite-thickness metal waveguides separated by an air gap (IMIMI geometry as shown by Figure 1-5 (b)) yield either attractive or repulsive forces, depending on the mode. The authors focus consideration on modes with long-range propagation characteristics, for which the field overlap with the metal, and consequently the loss, is relatively low.

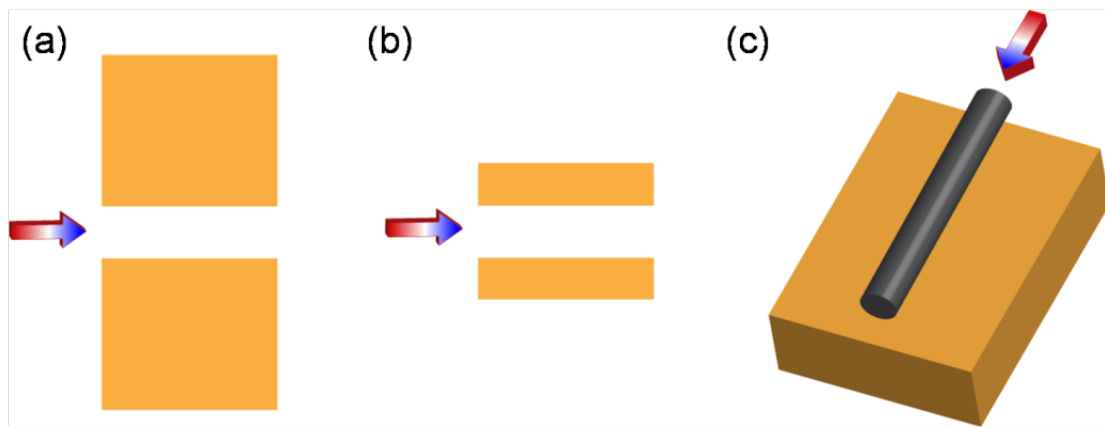


Figure 1-5 Optical forces generated in plasmonic devices: (a) finite-thickness metal waveguides separated by a dielectric gap, (b) semi-infinite metal plates separated by a dielectric gap, and (c) a hybrid plasmonic system with a dielectric waveguide and a metallic substrate.

Two papers have calculated force enhancements in hybrid plasmonic waveguides consisting of dielectric waveguides coupled to metallic substrates (Figure 1-5 (c)). References [34] and [35] show that the force between a silicon waveguide and a metal substrate is up to an order of magnitude larger than the force between the same waveguide and a dielectric substrate, given the same cross-sectional power. However, this conclusion applies only for relatively small

waveguide-substrate gaps. The plasmonic enhancement is non-resonant, and thus can be used for a broad range of wavelengths. However, due to ohmic loss, the hybrid plasmonic mode decays in the propagation direction. As a result, the enhancement will only be maintained for distances shorter than the plasmon decay length, typically on the order of 10's of microns.

In Chapter 2, the effect of slow light on optical force enhancement will be examined. The optical force is proportional to the light intensity in the propagating mode. Under conditions of fixed power input to a guided-wave mode, the light intensity scales as the input power over the group velocity. Consequently, reducing the group velocity of a mode increases the optical force for fixed input power. In the extreme case, as the light group velocity approaches zero, the optical force diverges.

1.3 Applications for On-chip Manipulation of Light Signals

As discussed above, optical forces have been calculated for a range of microphotonic device geometries, and mechanical motion arising from optical forces has been measured in a variety of experiments. This section will discuss some of the applications of these effects in on-chip information processing, such as filtering, switching, and other operations.

Optomechanical techniques offer particular advantages and disadvantages relative to other methods for tuning the response of a microphotonic system. Mechanical motion results in a large change in the effective index of a microphotonic structure, as compared to other tuning mechanisms such as thermal, electrooptic, and carrier injection. Thermal tuning through 10 degrees kelvin, for example, changes the index of silicon by less than 0.07%. Mechanical motion

changes the refractive index by order unity, due to the large index difference between silicon and air. The characteristic time scale for optomechanical effects is determined by the mechanical motion. If the device is operated in steady state, the time scale is determined by the mechanical period (proportional to the inverse mechanical resonance frequency). This number sets a lower limit on the time scale for response. If the optical signal is switched on abruptly, the mechanical displacement will equilibrate on a time scale determined by the product of the mechanical period and the mechanical quality factor.

With these general features, optomechanical effects can be used to construct novel, tunable, on-chip optical components. These include devices for wavelength filtering, self-adaptive microcavities, slow-light effects, and tunable lasers.

1.3.1. Tunable Directional Coupler

One example of a waveguide switch is a directional coupler [36]. The standard directional coupler design consists of two parallel waveguides. Light input to one waveguide transfers to the other waveguide over a characteristic length scale called the coupling length. For proper adjustment of the device length, L , all input light is transferred to the drop port. Tuning the effective index of the waveguides changes the coupling length, also changing the fraction of power that is output at the through and drop ports.

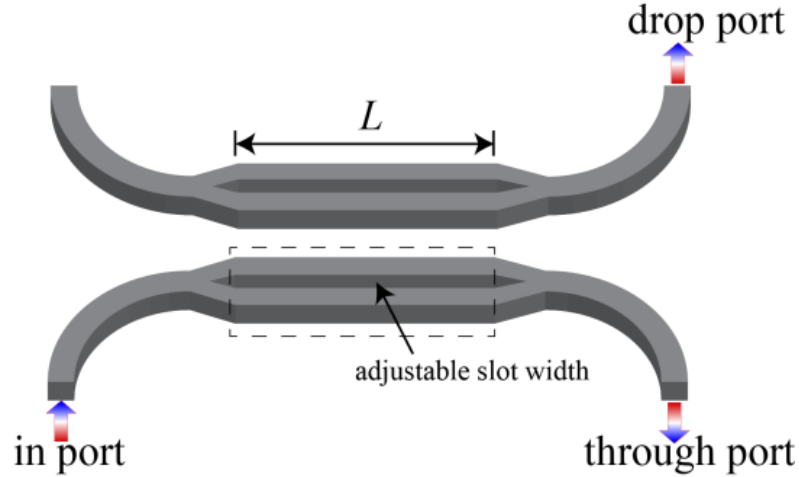


Figure 1-6: Optically-tunable directional coupler, in which the effective index of each arm is tuned via an adjustable slot width. Figure adapted from [37].

Fong et al [37] have used optical forces to demonstrate an all-optically tunable directional coupler. Each of the waveguides is a slot waveguide (Figure 1-6). An optical pump signal is used to induce an optical force, which reduces the slot width. The change in slot width causes a change in effective index of each slot waveguide, changing the behavior of the coupler. The authors demonstrated that the output power of a probe signal at the drop port could be tuned from 0.1% to 70% using 1.3 mW pump power. Dynamic modulation was also demonstrated.

1.3.2. Wavelength Filtering

Optical forces provide a method to achieve wideband tuning of microcavity resonances, with potential applications to filtering and routing.

In an early paper, Eichenfield *et al.* [38] demonstrated an all-optical tunable filter based on a high-Q silicon nitride microresonator coupled to a movable silica waveguide. The optical force

due to a strong pump beam pulls the waveguide toward the microresonator, changing the resonance frequency at a probe wavelength. The pump wavelength was tuned to change the waveguide-resonator separation, shifting the probe transmission spectrum.

Two papers have demonstrated tunable filters based on power tuning of a pump beam. Conceptually, the devices used are similar to Figure 1-2 (b); stacked microrings support coupled optical modes. The rings are mechanically supported by hub-and-spoke structures (not shown), which can be tailored to control the effective spring constant of the mechanical modes.

Rosenberg *et al.* [29] demonstrated the use of optical forces to tune the microcavity resonance in a double-ring, silica “spiderweb” structure. The optical force changes the separation between the rings, shifting the resonance. Static tuning was demonstrated with an efficiency of 2.5nm/mW. Dynamic tuning was demonstrated with a switching time less than 200 ns.

Wiederhecker *et al.* [39] later used optical forces to tune the optical resonance of a silicon nitride “double wheel” microcavity. Tuning of 30 nm was achieved with an efficiency of 2.3nm/mW. The authors argue that the tuning range is ultimately limited by the onset of mechanical regeneration.

In both these papers, the transmission line shape is a dip, or rejection filter. It has been suggested that modified devices and measurement configurations could be used to demonstrate related functions, such as routing, switching, buffering, dispersion compensation, pulse trapping and release, and tunable lasing [29]. The wide tunability suggests these functions could be achieved over the full telecom C- or L-bands [39].

1.3.3 Self-adaptive Microcavity

Rakich *et al.* [40] have proposed theoretically that optical forces can be used to design self-adaptive microcavities, cavities which tune themselves to the incident laser frequency. This behavior is achieved by careful design of the optomechanical potential in a modified, double-ring system, shown in Figure 1-7. The waveguide on the right is used to couple light into the rings. The force between rings is attractive at large separations and repulsive at small ones. As a result, the ring separation will adjust to a stable, intermediate separation value. Using the optical forces between an additional pair of coupled waveguides (shown on the left) to further shape the optomechanical potential, the system can be designed so that the stable ring separation always corresponds to a resonance frequency equal to the incident laser frequency.

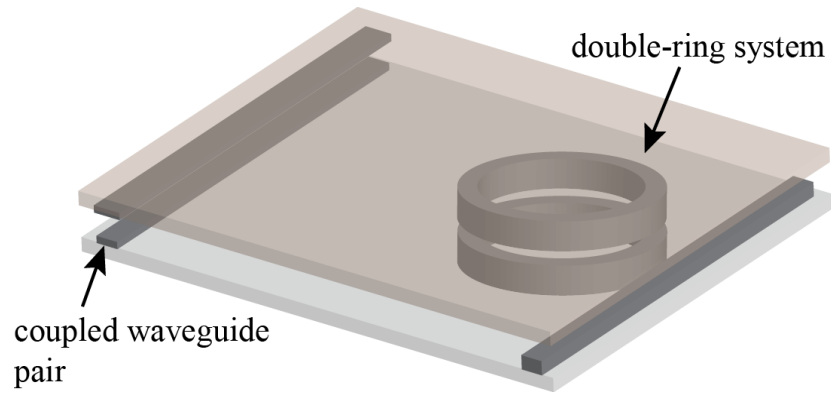


Figure 1-7 Schematic design of a self-tuning resonator, adapted from Reference [40].

The concept of a self-aligning microcavity may provide a route to more robust on-chip microcavity devices [41]. Temperature variations, fabrication error, and other factors all influence the resonant frequencies of microcavities. Using optomechanical effects, a reference

laser could be used to lock multiple microcavity devices on a chip (such as filters) to a standard frequency.

The main challenge in demonstrating self-adaptive behavior is fabrication feasibility. The design of Reference [40] requires two device layers. Each layer contains at least one waveguide and microring, and all devices within the layer must move together. Creative approaches and/or modified designs may be required to demonstrate self-adaptive concepts experimentally.

1.3.4 Slow Light

Recent papers by Painter and coworkers have suggested the use of optomechanical effects to achieve slowing of light [42, 43]. Motivated by the dramatic demonstration of stopped light in atomic gasses [44], resulting from electromagnetically-induced transparency (EIT), much recent work has attempted to demonstrate slow light in practical, on-chip microphotonic systems [45-47]. Applications of slow light, such as buffering and optical memories, are found in both classical and quantum information processing.

The maximum pulse delay that can be achieved in a slow light system is fundamentally limited by the lifetime of a “dark state,” a resonance of the system that is weakly coupled to the outside world. The dark-state lifetime scales as the product of the resonance period times the quality factor. Painter and coworkers have suggested the use of a *mechanical* resonance as the dark state; the mechanical period is typically much longer than the optical period. In Reference [42], the authors experimentally demonstrated a reflection spectrum characteristic of EIT in a optomechanical device. The structure is similar to Figure 1-3 (b), however, the microcavity is formed by changing the hole size and shape near the center of the device. At low temperature

(8.7 kelvin), an optically tunable delay of 50 nanoseconds with near-unity optical transparency was achieved. A method for tunable control of the optomechanical constant in time would further allow trapping and release of finite-bandwidth pulses.

1.3.5 Tunable Lasers

The ability to tune the operating wavelength of a semiconductor laser by mechanically modifying the optical cavity is an intriguing application of optomechanical devices. Alegre *et al.* [48] have analyzed laser tuning in photonic crystal “zipper” cavities (similar to Figure 1-3 (a)). They propose to use two optical resonances, one corresponding to a master (or pump) frequency, and the other to the slave (or lasing) frequency. The optical force resulting from pump light would be used to adjust the separation between two nanobeams that make up the zipper. The change in separation will shift the frequency of the lasing mode. A particular advantage of the zipper structure is the ability to obtain large optomechanical coupling constants [48]; the shift in the lasing frequency scales as the product of the optomechanical coupling constants for the pump and lasing modes. However, wavelength-tunable lasers could also be realized through other microscale resonant photonic topologies with optomechanically adjustable air gaps. Tradeoffs between considerations such as output power, wavelength tunability, frequency stability, and mode profile will affect the choice of design.

1.3.6. Our Contributions

In Chapter 2, 3 and 4, more applications of optical forces will be discussed. In Chapter 2, it will be proposed that optomechanical response also offers the opportunity to control or regulate transmitted power levels. Optical forces have been calculated between a periodically-patterned, movable silicon waveguide and a substrate. For a given wavelength of operation, the separation between waveguide and substrate will determine whether light propagates or falls in the photonic bandgap of the device. For proper design, increasing the optical power will pull the waveguide toward the substrate, moving the waveguide into the bandgap and prohibiting propagation. This effect should limit the total amount of power that can be transmitted through the device. The design of novel devices that perform the reverse function, only allowing transmission above certain power levels, will allow the regulation of power levels on chip. In combination with gain elements, optomechanical elements could thus provide a way to adaptively shape the average power of signal bit streams.

In Chapter 3, an effective Kerr nonlinearity will be studied in coupled coupled-waveguide systems, where the force between waveguides can be either attractive or repulsive. The essence of an optical nonlinearity is that the propagation characteristics of a device change with incident power. This is the case for optomechanical effects. Light results in a force that physically moves the device, affecting light propagation. The effective Kerr nonlinearity is named as “mechanical Kerr nonlinearity” [49]. It will be shown that either sign of the force results in a positive, giant mechanical Kerr coefficient and how the magnitude can be optimized with appropriate device parameters. The mechanical Kerr coefficient is several orders of magnitude larger than the ordinary Kerr coefficient of silicon.

In Chapter 4, it will be theoretically proposed that optomechanical effects could be used to achieve all-optically tunable birefringence. The birefringence in a system of two coupled waveguides (Figure 1-1 (a)) will be analyzed. By tuning the pump power injected in the waveguide, the separation between the waveguides can be adjusted. The change in separation affects the relative phase between TE and TM polarized modes. For appropriate values of the pump power, the device acts as a polarization converter, changing linear to circularly polarized light.

The ability to achieve mechanical Kerr effects and optically-tunable polarization rotation suggest that optomechanical effects can be used in a variety of switching configurations. The use of non-resonant devices should allow wide bandwidth response.

1.4 Applications for Assembly of Nanoparticles

The force of light on objects provides tremendous flexibility for microscale or nanoscale manipulation. As discussed above, optical forces can be used to construct novel, tunable, on-chip optical components for information processing. Other than repositioning elements of integrated photonics, optical forces can be utilized to manipulate particles. One famous example is optical tweezer [50-52], which use the optical gradient force of a focused laser.

Recent work has leveraged the strong field gradients near microphotonic devices for particle trapping [53-64]. However, such work has focused on trapping single or few particles. Our group have proposed to use optical forces near microphotonic devices for a fundamentally different purpose: to assemble periodic arrays of nanoparticles resembling synthetic, reconfigurable two dimensional (2D) crystals [65]. This approach, called light-assisted, templated self-assembly

(LATS), exploits photonic-crystal slabs to create resonantly enhanced optical forces orders of magnitude larger than radiation pressure.

The LATS process is shown schematically in Figure 1-8. Light is incident from below on a photonic-crystal slab, which consists of a silicon device layer patterned with a periodic array of air holes. The slab is designed to support guided-resonance modes, electromagnetic modes for which the light intensity near the slab is strongly enhanced [26]. The previous work has theoretically predicted [65] that when the incident laser is tuned to the wavelength of a guided-resonance mode, nanoparticles will be attracted toward the slab. The attractive, optical force arises from a strong electric-field gradient just above the slab surface. In addition, the nanoparticles will experience lateral optical forces due to the electromagnetic field structure of the guided resonance mode, resulting in the assembly of a nanoparticle array.

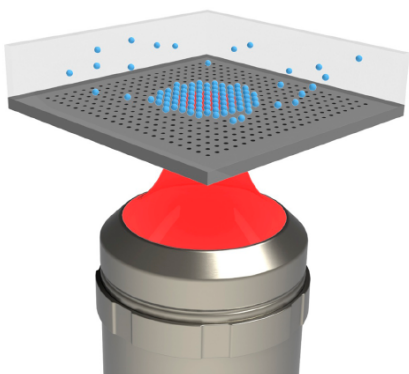


Figure 1-8 Schematic of light-assisted, templated self-assembly (LATS). Incident light from below excites a guided-resonance mode of a photonic-crystal slab, giving rise to optical forces on nanoparticles in solution. Under the influence of the forces, the nanoparticles self assemble into regular, crystalline patterns [66].

In the first experiment of LATS [66], a square array of over 100 polystyrene particles was assembled near a silicon photonic-crystal slab. The photonic crystal was fabricated on silicon-on-insulator wafer. A square lattice of 300-nm-diameter holes with periodicity of 860 nm were etched through 250-nm-deep silicon device layer. The slab was immersed in a suspension of 520-nm-diameter polystyrene particles and illuminated from below with a laser. The particles floating above the crystal were then moved into the holes by optical forces, forming a square crystal lattice measuring 13 μm on each side.

Figure 1-9 shows snapshots of the LATS process. When the laser beam is turned on, nanoparticles are attracted to the slab and begin to occupy sites of the square lattice (Figure 1-9 (a)). As time progresses, additional particles diffuse into the region where the beam intensity is high and begin to form a cluster (Figure 1-9 (b)). Eventually, a regular array of particles is formed (Figure 1-9 (c)). The square symmetry of the assembled particles is evident from the picture. When the laser beam is turned off, the particles immediately begin to disperse and diffuse away from the slab (Figure 1-9 (d)).

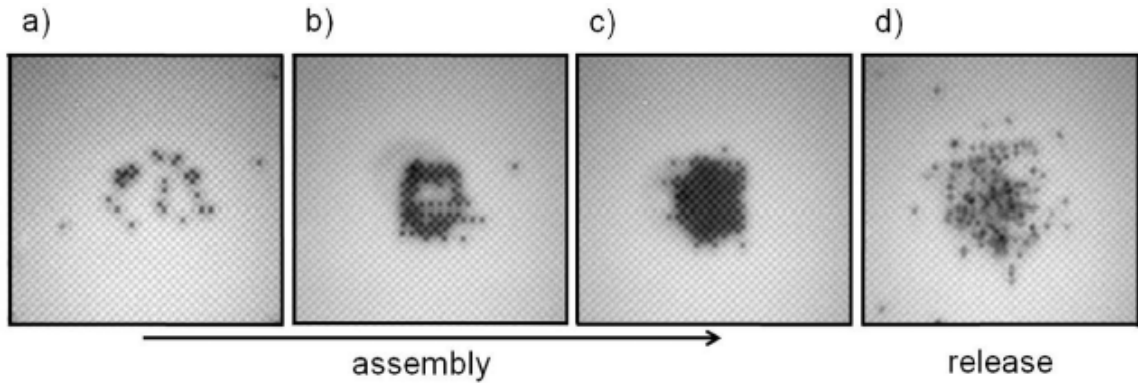


Figure 1-9 Light-assisted, templated self-assembly of 520 nm diameter particles above a photonic-crystal slab. (a–c) Sequential snapshots taken with the light beam on. (d) Snapshot taken after the beam is turned off.

Nanoparticle arrays assembled using LATS can be viewed as “programmable optical matter” [67]: turning the laser on and off will reversibly assemble or disassemble the structure. Moreover, exciting different resonance modes of the photonic crystal, by adjusting the wavelength of the input laser, should allow different crystalline structures to be formed [65].

Light-driven assembly of multiparticle patterns has previously been achieved using structured light fields generated by interference fringes, holography, spatial light modulators, or other methods [68]. The LATS approach differs crucially from previous work in that it exploits near-field, rather than farfield effects. Rather than generating a structured light beam via free-space optics, a simple, Gaussian input beam is used. The structured light field responsible for trapping is generated by the interaction of light with the photonic-crystal device. Ultimately, however, LATS could be carried out using a photonic-crystal laser, allowing the integration of the light source with the trapping device and making our approach highly suitable for on-chip

integration. Thus a wide range of applications can be expected from all-optically tunable photonic devices, to materials assembly, to biological trapping and manipulation.

In the previous work, a simple, square-lattice design for the photonic crystal is considered. It is envisioned that the LATS technique can be extended to assemble larger numbers of particles by designing the photonic-crystal slab to reduce the input power per area required for trapping. The input beam can then be spread over a larger area, resulting in a larger cluster. One approach to reducing the required power per area is to use a mode with a higher quality factor. Another approach is to strongly localize the field in the trapping regions. With these two principles, novel lattices will be proposed in Chapter 5 and 6. By judicious design, guided resonance modes with high quality factors and mode localization can be achieved in the novel photonic crystal lattice. It is expected that the new design will allow assembly of larger numbers of particles.

1.5 Force Calculation

Accurate calculations of optical forces in realistic, 3D structures can be performed using electromagnetic modeling techniques.

1.5.1. Maxwell Stress Tensor

One method for force calculation is to evaluate the Maxwell stress tensor (MST) numerically [69]. This general, flexible technique allows one to directly calculate the force based on the full electromagnetic field distributions, which can be obtained from an appropriate full-vectorial electromagnetic solver. The MST method has been used to evaluate optical forces in many

contexts [22, 70-73]. To compute the optical forces acting on a movable component, the Maxwell stress tensor is numerically integrated over a closed surface surrounding the component:

$$F_\alpha = \oint_S \sum T_{\alpha\beta} n_\beta da \quad (1-1)$$

where α and β indicate direction x , y or z , \mathbf{n} is the outward normal to the closed surface S , and the stress tensor,

$$T_{\alpha\beta} = \varepsilon E_\alpha E_\beta + \mu H_\alpha H_\beta - \frac{1}{2} \delta_{\alpha\beta} (\varepsilon \mathbf{E} \cdot \mathbf{E} + \mu \mathbf{H} \cdot \mathbf{H}).$$

Typically, the time scale for mechanical response is longer than the optical period, and the time-averaged force over the optical period may be considered [73]. The disadvantage of the MST method is that since it requires the knowledge of the full electromagnetic fields, it is computationally intensive and can become prohibitive for large system size.

1.5.2 Derivative Method

It has been shown previously [3] that for infinitely long waveguides with no radiation loss, the force between two waveguides can be calculated from the derivative of the eigenmode frequency with respect to separation. This relationship follows from expressing the force as a derivative of the electromagnetic energy U with respect to waveguide separation, g :

$$F = - \left. \frac{dU}{dg} \right|_k = - \left. \frac{d(N\hbar\omega)}{dg} \right|_k = -N\hbar \left. \frac{d\omega}{dg} \right|_k = - \frac{U}{\omega} \left. \frac{d\omega}{dg} \right|_k, \quad (1-2)$$

where N is the number of photons, ω is the eigenmode frequency, and k is the wave vector.

An optomechanical coupling constant can be defined as g_{OM} . The value of g_{OM} is proportional to the force per photon (F/N) on the mechanical system. Larger values of g_{OM} indicate a larger change in the optical properties of the system for a given mechanical displacement.

It is often convenient to consider the force per unit length of the waveguide, normalized to the input power P . Under conditions of fixed power input to a guided-wave mode, the electromagnetic field energy U scales as the input power over the group velocity: $U=PL/v_g$. The normalized force is:

$$\frac{F}{PL} = -\frac{1}{\omega v_g} \left. \frac{d\omega}{dg} \right|_k \quad (1-3)$$

Consequently, reducing the group velocity of a mode tends to increase the optical force per unit waveguide length at fixed input power. The force may alternately be written as a derivative of the effective index n_{eff} with respect to separation [13]:

$$\frac{F}{PL} = \frac{1}{v_g n_{eff}} \left. \frac{dn_{eff}}{dg} \right|_k \quad (1-4)$$

In Equations (1-3) and (1-4), the derivatives are taken at fixed wave vector.

Derivative methods generally assume that the optomechanical system is closed and does not exchange energy with the surrounding media. The force between two microcavities can also be calculated as a derivative of the cavity mode frequency with respect to separation, provided that the cavity quality factor is large [22, 74]. For microresonator systems, the optical force is proportional to the electromagnetic field energy stored in the resonators.

Rakich *et al.* have shown that for general linear, lossless systems, the force can be written in terms of the scattering matrix [75]. This method is particularly useful for systems that can be accurately described by coupled-mode theory [76], such as systems of multiple microresonators coupled to waveguides, in which full-field calculations can prove prohibitive.

Given the value of the optical force at a given optical power level, a resulting static displacement can be calculated by solving the corresponding mechanical problem. A typical approach is to use finite element software, such as COMSOL, for this purpose.

In the following chapters, the force calculation will be discussed in more detail in specific systems.

1.6 Thesis Overview

Since the initial theoretical studies on optical forces between microphotonic devices, experimental progress has been rapid. The goal of this thesis is to explore applications of optical forces in micro-photonics systems. There are two major tasks. One is to exploit effects of optical forces in highly tunable, on-chip devices, and the corresponding discussion will be in Chapter 2, 3 and 4. The other task is to utilize optical forces for light-assisted, template self-assembly (LATS) of nanoparticles. A novel photonic crystal template is designed in Chapter 5 for lower-power assembly. In Chapter 6, experiments are carried out to characterize optical performance of a new photonic crystal lattice potential for lower-power LATS. In Chapter 7, a method is proposed to predict the radiation loss of coupled resonator optical waveguides in photonic crystal slabs. The method may facilitate the design of large-area, coupled-cavity modes with high quality factor that nevertheless couple to normally-incident radiation for LATS.

In Chapter 2, the attractive optical force is numerically investigated between a suspended one-dimensional periodic photonic crystal waveguide and underlying substrate in a silicon-on-insulator platform. It is shown that the optical force can be enhanced by designing the waveguide cross section to make the mode approach the band edge or substrate light line. For periodic waveguides, the optical force is non-monotonic with waveguide-substrate separation. This effect may enable the design of compact, integrated optical power limiters.

In Chapter 3, an analytical method is proposed to calculate optical forces between silicon waveguides based on the perturbation of effective index at fixed frequency. The method is used to investigate the mechanical Kerr effect in a coupled-waveguide system with bipolar forces. It is shown that positive mechanical Kerr coefficient results from either an attractive or repulsive force. An enhanced mechanical Kerr coefficient several orders of magnitude larger than the intrinsic Kerr coefficient is obtained in waveguides for which the optical mode approaches the air light line, given appropriate design of the waveguide dimensions.

In Chapter 4, an optomechanical method is presented to tune phase and group birefringence in parallel silicon strip waveguides. The deformation of suspended, parallel strip waveguides due to optical forces is calculated. The frequency and polarization of the pump light is optimized to obtain a 9nm deformation for an optical power of 20 mW. Widely tunable phase and group birefringence can be achieved by varying the pump power, with maximum values of 0.026 and 0.13, respectively. The giant phase birefringence allows linear to circular polarization conversion within 30 μ m for a pump power of 67mW. The group birefringence gives a tunable differential group delay of 6fs between orthogonal polarizations. The tuning performance of waveguides is evaluated with different cross sections.

In Chapter 5, a novel photonic crystal lattice is proposed for trapping a two-dimensional array of particles. The lattice is created by introducing a rectangular slot in each unit cell of the Suzuki-Phase lattice to enhance the light confinement of guided resonance modes. Large quality factors on the order of 10^5 are predicted in the lattice. A significant decrease of the optical power required for optical trapping can be achieved compared to the previous design based on square lattice.

In Chapter 6, experiments are carried out to optically characterize a new photonic crystal structure. This photonic crystal device is generated by using regular graphite lattice as the base and adding a slot into the center of each unit cell for enhancing field confinement. The lattice has been optimized to obtain guided resonant modes with high quality factor over 4×10^5 . The evolution of the measured wavelengths and quality factors follows the trend predicted by the simulations.

In Chapter 7, the tight binding approximation (TBA) is used to relate the intrinsic, radiation loss of a coupled resonator optical waveguide (CROW) to that of a single constituent resonator within a light cone picture. The validity of the TBA is verified via direct, full-field simulation of CROWs based on the L2 photonic crystal cavity. The TBA predicts that the quality factor of the CROW increases with that of the isolated cavity. Moreover, the results provide a method to design CROWs with low intrinsic loss across the entire waveguide band.

1.7 Chapter References

[1]. A. Ashkin, "History of optical trapping and manipulation of small-neutral particle, atoms, and molecules," *Selected Topics in Quantum Electronics, IEEE Journal of* **6**, 841-856 (2000).

- [2]. K. C. Neuman, and S. M. Block, "Optical trapping," Rev. Sci. Instrum. **75**, 2787-2809 (2004).
- [3]. M. L. Povinelli, M. Loncar, M. Ibanescu, E. J. Smythe, S. G. Johnson, F. Capasso, and J. D. Joannopoulos, "Evanescent-wave bonding between optical waveguides," Opt. Lett. **30**, 3042-3044 (2005).
- [4]. S. Noda, K. Tomoda, N. Yamamoto, and A. Chutinan, "Full Three-Dimensional Photonic Bandgap Crystals at Near-Infrared Wavelengths," Science **289**, 604-606 (2000).
- [5]. V. R. Almeida, C. A. Barrios, R. R. Panepucci, and M. Lipson, "All-optical control of light on a silicon chip," Nature **431**, 1081-1084 (2004).
- [6]. R. A. Soref, "Silicon-based optoelectronics," Proc. IEEE **81**, 1687-1706 (1993).
- [7]. L. Pavesi, and D. J. Lockwood, *Silicon Photonics* (Springer, Berlin ; New York, 2004).
- [8]. M. Haurylau, C. Guoqing, C. Hui, Z. Jidong, N. A. Nelson, D. H. Albonesi, E. G. Friedman, and P. M. Fauchet, "On-Chip Optical Interconnect Roadmap: Challenges and Critical Directions," Selected Topics in Quantum Electronics, IEEE Journal of **12**, 1699-1705 (2006).
- [9]. A. Faraon, A. Majumdar, D. Englund, E. Kim, M. Bajcsy, and J. Vuckovic, "Integrated quantum optical networks based on quantum dots and photonic crystals," New J. Phys. **13**, 13.
- [10]. W. H. P. Pernice, M. Li, D. Garcia-Sanchez, and H. X. Tang, "Analysis of short range forces in opto-mechanical devices with a nanogap," Opt. Express **18**, 12615-12621.
- [11]. M. Li, W. H. Pernice, and H. X. Tang, "Ultrahigh-frequency nano-optomechanical resonators in slot waveguide ring cavities," Appl. Phys. Lett. **97**, 183110.
- [12]. A. Dorsel, J. D. McCullen, P. Meystre, E. Vignes, and H. Walther, "Optical Bistability and Mirror Confinement Induced by Radiation Pressure," Phys. Rev. Lett. **51**, 1550 (1983).
- [13]. W. H. P. Pernice, M. Li, and H. X. Tang, "Theoretical investigation of the transverse optical force between a silicon nanowire waveguide and a substrate," Opt. Express **17**, 1806-1816 (2009).

- [14]. M. Li, W. H. P. Pernice, C. Xiong, T. Baehr-Jones, M. Hochberg, and H. X. Tang, "Harnessing optical forces in integrated photonic circuits," *Nature* **456**, 480-484 (2008).
- [15]. J. S. Foresi, P. R. Villeneuve, J. Ferrera, E. R. Thoen, G. Steinmeyer, S. Fan, J. D. Joannopoulos, L. C. Kimerling, H. I. Smith, and E. P. Ippen, "Photonic-bandgap microcavities in optical waveguides," *Nature* **390**, 143-145 (1997).
- [16]. Y. Akahane, T. Asano, B. S. Song, and S. Noda, "High-Q photonic nanocavity in a two-dimensional photonic crystal," *Nature* **425**, 944-947 (2003).
- [17]. B. S. Song, S. Noda, T. Asano, and Y. Akahane, "Ultra-high-Q photonic double-heterostructure nanocavity," *Nat. Mater.* **4**, 207-210 (2005).
- [18]. H. Y. Ryu, M. Notomi, and Y. H. Lee, "High-quality-factor and small-mode-volume hexapole modes in photonic-crystal-slab nanocavities," *Applied Physics Letters* **83**, 4294-4296 (2003).
- [19]. J. Chan, M. Eichenfield, R. Camacho, and O. Painter, "Optical and mechanical design of a "zipper" photonic crystal optomechanical cavity," *Opt. Express* **17**, 3802-3817 (2009).
- [20]. M. Eichenfield, R. Camacho, J. Chan, K. J. Vahala, and O. Painter, "A picogram- and nanometre-scale photonic-crystal optomechanical cavity," *Nature* **459**, 550-555 (2009).
- [21]. M. Eichenfield, J. Chan, R. M. Camacho, K. J. Vahala, and O. Painter, "Optomechanical crystals," *Nature* **462**, 78-82 (2009).
- [22]. H. Taniyama, M. Notomi, E. Kuramochi, T. Yamamoto, Y. Yoshikawa, Y. Torii, and T. Kuga, "Strong radiation force induced in two-dimensional photonic crystal slab cavities," *Physical Review B* **78**, 165129 (2008).
- [23]. M. Notomi, H. Taniyama, S. Mitsugi, and E. Kuramochi, "Optomechanical wavelength and energy conversion in high-Q double-layer cavities of photonic crystal slabs," *Phys. Rev. Lett.* **97**, 4 (2006).
- [24]. S. Fan, and M. L. Povinelli, "Stopping Light via Dynamic Tuning of Coupled Resonators," in *Slow Light: Science and Applications* (CRC Press, Boca Raton, 2009).

- [25]. S. Fan, S. Sandhu, C. Otey, and M. Povinelli, "Slow and Stopped Light in Coupled Resonator Systems," in *Photonic Microresonator Research and Applications*(Springer Berlin / Heidelberg), pp. 165-180.
- [26]. S. Fan, and J. D. Joannopoulos, "Analysis of guided resonances in photonic crystal slabs," *Physical Review B* **65**, 235112 (2002).
- [27]. V. Liu, M. Povinelli, and S. H. Fan, "Resonance-enhanced optical forces between coupled photonic crystal slabs," *Optics Express* **17**, 21897-21909 (2009).
- [28]. Y. G. Roh, T. Tanabe, A. Shinya, H. Taniyama, E. Kuramochi, S. Matsuo, T. Sato, and M. Notomi, "Strong optomechanical interaction in a bilayer photonic crystal," *Physical Review B* **81**, 4 (2010).
- [29]. J. Rosenberg, Q. Lin, and O. Painter, "Static and dynamic wavelength routing via the gradient optical force," *Nat Photon* **3**, 478-483 (2009).
- [30]. A. W. Rodriguez, A. P. McCauley, P.-C. Hui, D. Woolf, E. Iwase, F. Capasso, M. Loncar, and S. G. Johnson, "Bonding, antibonding and tunable optical forces in asymmetric membranes," *Opt. Express* **19**, 2225-2241 (2011).
- [31]. A. W. Rodriguez, D. Woolf, P. C. Hui, E. Iwase, A. P. McCauley, F. Capasso, M. Loncar, and S. G. Johnson, "Designing evanescent optical interactions to control the expression of Casimir forces in optomechanical structures," *Applied Physics Letters* **98**, 3.
- [32]. S. A. Maier, *Plasmonics: Fundamentals and Applications* (Springer, New York, 2007).
- [33]. D. Woolf, M. Loncar, and F. Capasso, "The forces from coupled surface plasmon polaritons in planar waveguides," *Optics Express* **17**, 19996-20011 (2009).
- [34]. X. D. Yang, Y. M. Liu, R. F. Oulton, X. B. Yin, and X. A. Zhang, "Optical Forces in Hybrid Plasmonic Waveguides," *Nano Lett.* **11**, 321-328.
- [35]. C. G. Huang, and L. Zhu, "Enhanced optical forces in 2D hybrid and plasmonic waveguides," *Optics Letters* **35**, 1563-1565.
- [36]. B. E. A. Saleh, and M. C. Teich, *Fundamentals of Photonics* (1991).

- [37]. K. Y. Fong, W. H. P. Pernice, M. Li, and H. X. Tang, "Tunable optical coupler controlled by optical gradient forces," *Opt. Express* **19**, 15098-15108.
- [38]. M. Eichenfield, C. P. Michael, R. Perahia, and O. Painter, "Actuation of micro-optomechanical systems via cavity-enhanced optical dipole forces," *Nat Photon* **1**, 416-422 (2007).
- [39]. G. S. Wiederhecker, S. Manipatruni, S. Lee, and M. Lipson, "Broadband tuning of optomechanical cavities," *Opt. Express* **19**, 2782-2790.
- [40]. P. T. Rakich, M. A. Popovic, M. Soljacic, and E. P. Ippen, "Trapping, corralling and spectral bonding of optical resonances through optically induced potentials," *Nat Photon* **1**, 658-665 (2007).
- [41]. M. A. Popovic, and P. T. Rakich, "Optonanomechanical self-adaptive photonic devices based on light forces: a path to robust high-index-contrast nanophotonic circuits," in *Optoelectronic Integrated Circuits XI*, L. A. Eldada, and E. H. Lee, eds. (SPIE-Int Soc Optical Engineering, Bellingham, 2009).
- [42]. A. H. Safavi-Naeini, T. P. M. Alegre, J. Chan, M. Eichenfield, M. Winger, Q. Lin, J. T. Hill, D. E. Chang, and O. Painter, "Electromagnetically induced transparency and slow light with optomechanics," *Nature* **472**, 69-73.
- [43]. D. E. Chang, A. H. Safavi-Naeini, M. Hafezi, and O. Painter, "Slowing and stopping light using an optomechanical crystal array," *New J. Phys.* **13**, 26.
- [44]. S. E. Harris, "Electromagnetically induced transparency," *Phys. Today* **50**, 36-42 (1997).
- [45]. M. F. Yanik, W. Suh, Z. Wang, and S. H. Fan, "Stopping light in a waveguide with an all-optical analog of electromagnetically induced transparency," *Phys. Rev. Lett.* **93**, 4 (2004).
- [46]. M. F. Yanik, and S. H. Fan, "Stopping and storing light coherently," *Phys. Rev. A* **71**, 10 (2005).
- [47]. S. H. Fan, M. F. Yanik, Z. Wang, S. Sandhu, and M. L. Povinelli, "Advances in theory of photonic crystals," *J. Lightwave Technol.* **24**, 4493-4501 (2006).

- [48]. T. P. M. Alegre, R. Perahia, and O. Painter, "Optomechanical zipper cavity lasers: theoretical analysis of tuning range and stability," *Optics Express* **18**, 7872-7885.
- [49]. W. H. P. Pernice, M. Li, and H. X. Tang, "A mechanical Kerr effect in deformable photonic media," *Applied Physics Letters* **95**, 123507-123503 (2009).
- [50]. A. Ashkin, J. M. Dziedzic, J. E. Bjorkholm, and S. Chu, "Observation of a single-beam gradient force optical trap for dielectric particles," *Opt. Lett.* **11**, 288-290 (1986).
- [51]. A. Ashkin, J. M. Dziedzic, and T. Yamane, "OPTICAL TRAPPING AND MANIPULATION OF SINGLE CELLS USING INFRARED-LASER BEAMS," *Nature* **330**, 769-771 (1987).
- [52]. A. Ashkin, "Optical trapping and manipulation of neutral particles using lasers," *Proc. Natl. Acad. Sci. U. S. A.* **94**, 4853-4860 (1997).
- [53]. S. Lin, J. Hu, L. Kimerling, and K. Crozier, "Design of nanoslotted photonic crystal waveguide cavities for single nanoparticle trapping and detection," *Opt. Lett.* **34**, 3451-3453 (2009).
- [54]. K. Okamoto, and S. Kawata, "Radiation Force Exerted on Subwavelength Particles near a Nanoaperture," *Phys. Rev. Lett.* **83**, 4534-4537 (1999).
- [55]. B. K. Wilson, T. Mentele, S. Bachar, E. Knouf, A. Bendoraite, M. Tewari, S. H. Pun, and L. Y. Lin, "Nanostructure-enhanced laser tweezers for efficient trapping and alignment of particles," *Opt. Express* **18**, 16005-16013.
- [56]. M. Righini, A. S. Zelenina, C. Girard, and R. Quidant, "Parallel and selective trapping in a patterned plasmonic landscape," *Nat Phys* **3**, 477-480 (2007).
- [57]. A. N. Grigorenko, N. W. Roberts, M. R. Dickinson, and Y. Zhang, "Nanometric optical tweezers based on nanostructured substrates," *Nat. Photonics* **2**, 365-370 (2008).
- [58]. M. L. Juan, M. Righini, and R. Quidant, "Plasmon nano-optical tweezers," *Nat Photon* **5**, 349-356 (2011).

- [59]. B. J. Roxworthy, K. D. Ko, A. Kumar, K. H. Fung, E. K. C. Chow, G. L. Liu, N. X. Fang, and K. C. Toussaint, "Application of Plasmonic Bowtie Nanoantenna Arrays for Optical Trapping, Stacking, and Sorting," *Nano Lett.* **12**, 796-801 (2012).
- [60]. A. H. J. Yang, S. D. Moore, B. S. Schmidt, M. Klug, M. Lipson, and D. Erickson, "Optical manipulation of nanoparticles and biomolecules in sub-wavelength slot waveguides," *Nature* **457**, 71-75 (2009).
- [61]. S. Lin, E. Schonbrun, and K. Crozier, "Optical Manipulation with Planar Silicon Microring Resonators," *Nano Lett.* **10**, 2408-2411 (2010).
- [62]. S. Mandal, X. Serey, and D. Erickson, "Nanomanipulation Using Silicon Photonic Crystal Resonators," *Nano Lett.* **10**, 99-104 (2010).
- [63]. Y. F. Chen, X. Serey, R. Sarkar, P. Chen, and D. Erickson, "Controlled Photonic Manipulation of Proteins and Other Nanomaterials," *Nano Lett.* **12**, 1633-1637.
- [64]. C. Renaut, J. Dellinger, B. Cluzel, T. Honegger, D. Peyrade, E. Picard, F. de Fornel, and E. Hadji, "Assembly of microparticles by optical trapping with a photonic crystal nanocavity," *Applied Physics Letters* **100**, 101103-101103 (2012).
- [65]. C. A. Mejia, A. Dutt, and M. L. Povinelli, "Light-assisted templated self assembly using photonic crystal slabs," *Opt. Express* **19**, 11422-11428 (2011).
- [66]. E. Jaquay, L. J. Martinez, C. A. Mejia, and M. L. Povinelli, "Light-Assisted, Templated Self-Assembly Using a Photonic-Crystal Slab," *Nano Lett.* **13**, 2290-2294 (2013).
- [67]. M. M. Burns, J.-M. Fournier, and J. A. Golovchenko, "Optical Matter: Crystallization and Binding in Intense Optical Fields," *Science* **249**, 749-754 (1990).
- [68]. P. Korda, G. C. Spalding, E. R. Dufresne, and D. G. Grier, "Nanofabrication with holographic optical tweezers," *Rev. Sci. Instrum.* **73**, 1956-1957 (2002).
- [69]. J. D. Jackson, *Classical Electrodynamics* (Wiley, New York, 1999).

- [70]. M. L. Povinelli, M. Ibanescu, S. G. Johnson, and J. D. Joannopoulos, "Slow-light enhancement of radiation pressure in an omnidirectional-reflector waveguide," *Applied Physics Letters* **85**, 1466-1468 (2004).
- [71]. A. Mizrahi, and L. Schachter, "Mirror manipulation by attractive and repulsive forces of guided waves," *Opt. Express* **13**, 9804-9811 (2005).
- [72]. J. Ng, C. T. Chan, P. Sheng, and Z. Lin, "Strong optical force induced by morphology-dependent resonances," *Opt. Lett.* **30**, 1956-1958 (2005).
- [73]. M. I. Antonoyiannakis, and J. B. Pendry, "Electromagnetic forces in photonic crystals," *Physical Review B* **60**, 2363 (1999).
- [74]. M. L. Povinelli, S. G. Johnson, M. Loncar, M. Ibanescu, E. Smythe, F. Capasso, and J. D. Joannopoulos, "High-Q enhancement of attractive and repulsive optical forces between coupled whispering-gallery- mode resonators," *Opt. Express* **13**, 8286-8295 (2005).
- [75]. P. T. Rakich, M. A. Popovic, and Z. Wang, "General Treatment of Optical Forces and Potentials in Mechanically Variable Photonic Systems," *Optics Express* **17**, 18116-18135 (2009).
- [76]. H. A. Haus, and W. P. Huang, "Coupled-mode theory," *Proc. IEEE* **79**, 1505-1518 (1991).

Chapter 2: Effect of Periodicity on Optical Forces

2.1 Background

In the last few years, intense research has been carried out on optical forces induced by the strongly enhanced gradient of the electromagnetic field close to micro- and nanophotonic devices [1-11]. The forces provide a way to reconfigure microphotonic elements with experimentally measurable deflection [12-14]. This mechanical actuation allows a number of important device functionalities, such as all-optically controlled filters [15], wavelength routers [16], and polarization rotators [17], as well as optomechanical Kerr effects [18]. One structure that is particularly amenable to fabrication is a suspended, microbridge waveguide over a substrate [19]. For appropriately designed devices, it has been predicted and verified experimentally that the optical force is dominant over other effects, such as thermo-optical effects, Casimir and van der Waals forces [19, 20]. Previous theoretical and experimental work has demonstrated that light traveling through an unpatterned waveguide induces an attractive optical force between the waveguide and substrate [19, 21]. Introducing a periodic pattern into the waveguide to form a one-dimensional (1D) periodic photonic crystal should introduce additional flexibility in tuning the behavior of the optical force.

Here we numerically investigate the effects of periodicity on optical forces between a microphotonic waveguide and substrate. While previous work has analyzed 1D-periodic photonic crystal microcavities [22, 23], we consider light propagation in the pass band of a 1D-periodic periodic crystal. We show that the optical force on a 1D-periodic photonic crystal waveguide is enhanced due to several different physical effects: delocalization near the substrate light line, effective reduction of the waveguide refractive index, and slow-light enhancement

near the band gap. We find that, in contrast to unpatterned waveguides, the optical force shows a non-monotonic dependence with waveguide-substrate separation. The force behavior near the photonic band edge may enable the design of optical switches that transmit only below a certain power threshold, i.e. power limiters.

2.2 Band Edge Effects

We investigate the optical force between a patterned, 1D-periodic photonic crystal silicon waveguide and an underlying silica substrate, as shown in Figure 2-1 (a). In the paper, the physical wavelength is fixed to 1550 nm. We assume one period of the waveguide is a cube of side length a with a circular air hole of radius $r=0.3a$. The modes of the waveguide-substrate system can be characterized as even or odd with respect to the mirror plane at $y=0$, according to the symmetry of the vector field [24]. We refer to the y-even mode as TM; the electric field is primarily in the z -direction. We refer to the y-odd mode as TE; the electric field is primarily in the y -direction.

In Figure 2-1 (b), we plot the dispersion curves for the two lowest TM bands and the lowest TE band. The two lowest TM bands are separated by a band gap. For TE polarization, the second lowest band does not couple strongly to a linearly polarized source and is not shown in the figure. We use the MIT Photonic Bands package [25] to calculate the full vectorial electromagnetic fields for one period of the infinite structure. From the fields, we calculate the force using the Maxwell Stress Tensor [26]. We plot the force per unit length per unit power ($F/L/P$), where we assume $P = Uv_g/L$. v_g is the group velocity, and U is the electromagnetic field energy [2]. We confine our calculation to the values of the period a for which the modes are guided (lie below

the gray region in Figure 2-1(b)). All three of the modes shown give rise to an attractive optical force.

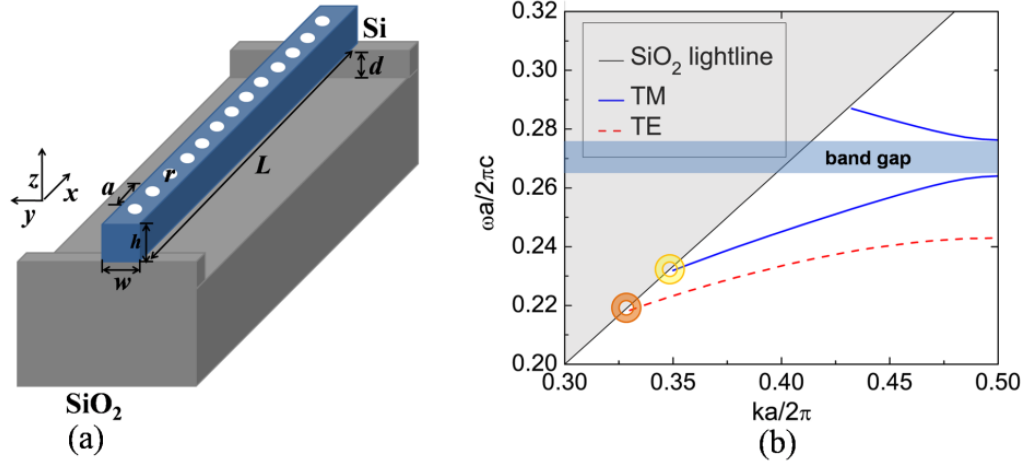


Figure 2-1 (a) Patterned, 1D-periodic photonic crystal Si waveguide with period a is separated from the SiO_2 substrate by a distance $d = 100$ nm. r is the hole radius.
 (b) Dispersion relation for TM (blue solid curve) and TE (red dashed curve) modes in waveguide with $r = 0.3a$, and $h = w = a$. The gray region shows the substrate light cone. The point where the TE/TM mode crosses the light line is indicated by an orange/yellow circle.

Figure 2-2 (a) shows force per unit length per unit power as a function of the side length a for the TM modes (blue circles). The waveguide-substrate separation $d = 100$ nm. The yellow circle indicates the value of a (~ 365 nm) for which the TM mode enters the light line. The blue box indicates the range of a for which 1550 nm light falls within the band gap of the TM modes. In this range, no light can propagate along the waveguide, and thus, no optical force is induced. We observe from the figure that the force increases near the light line and near the band edge. To understand these trends, we plot the force for an unpatterned strip waveguide with the same dimensions but no air holes (black squares). For the strip waveguide, the mode crosses the light

line at a value of $a \sim 280$ nm, shown by the yellow circle. Like the patterned waveguide, the force increases as the mode approaches the light line, due to stronger coupling between the waveguide and substrate. Overall, the force curve for the patterned waveguide is shifted to the right with respect to the strip waveguide. This effect can be interpreted as a reduction of the effective index due to the air holes. We plot the force curve for a strip waveguide with reduced index equal to 2.79 with pink triangles. Away from the band gap, the force curve for the patterned waveguide follows that of the reduced-index waveguide. Near the band gap, the enhancement of force can be interpreted as a slow-light effect [1]. For fixed power, the energy in the mode increases proportionally to $1/v_g$, where v_g is the group velocity. Since the force is proportional to mode energy, the force per length per unit power goes to infinity for an ideal slow-light waveguide.

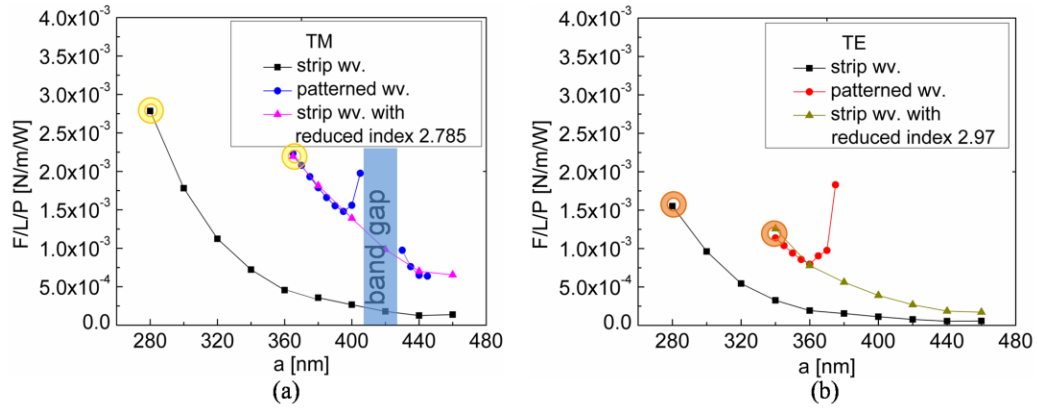


Figure 2-2 The attractive force per length per unit power as a function of period a for (a) TM and (b) TE modes at wavelength $\lambda = 1550$ nm. One period of the waveguide (wv.) is a cube of side length a with a circular air hole of radius $r = 0.3a$. The separation d between the suspended waveguide and substrate is 100 nm.

We plot the force for TE modes for values of a between 340 nm and 375 nm in Figure 2-2 (b). The light wavelength is 1550 nm. As for TM light, the force is enhanced near the light line and band edge. Away from the slow-light region, the force curve follows that of a strip waveguide with reduced refractive index equal to 2.97, (green triangles).

We next consider the dependence of the force on the waveguide-substrate separation, d . In a conventional strip waveguide, the force increases monotonically with decreasing distance [19]. In the patterned waveguide, however, a change in distance can move a mode in or out of the photonic band gap, yielding quite different force behavior.

We consider a waveguide with $a = 428\text{nm}$. From Figure 2-2 (a), we can infer that the TM mode lies just above the band gap for $d = 100\text{nm}$. We plot the force as a function of separation in Figure 2-3 (a) (blue triangles). The force initially decreases with increasing distance, then increases as the mode approaches the band edge. For $d > 120\text{nm}$, the mode lies in the band gap. The transmission, and thus force, are zero.

For a waveguide with $a = 408\text{nm}$, we can see from Figure 2-2 (a) that the mode lies just below the band gap for $d = 100\text{nm}$. The force (red circles) is zero for distances below $\sim 80\text{nm}$, where the mode falls into the band gap, and decreases as a function of distance for $d > 80\text{nm}$. The behavior should allow the design of an optical power limiter. If the device is designed with an initial waveguide-substrate distance $> 80\text{nm}$, light can be transmitted through the waveguide. As the optical power is increased, the optical force will attract the waveguide to the substrate more strongly. In the center of the double-clamped waveguide, where the displacement is largest, the local mode will approach or enter the band gap, resulting in reflection, and reducing the transmitted power.

Figure 2-3 (b) gives the force induced by near band edge TE light for a waveguide with $a=376$ nm. When a is less than 60 nm, the fundamental mode is no longer guided, and we set the force to zero. While non-negligible force values may be obtained for leaky modes with long propagation lengths, the force will decay as a function of length along the waveguide.

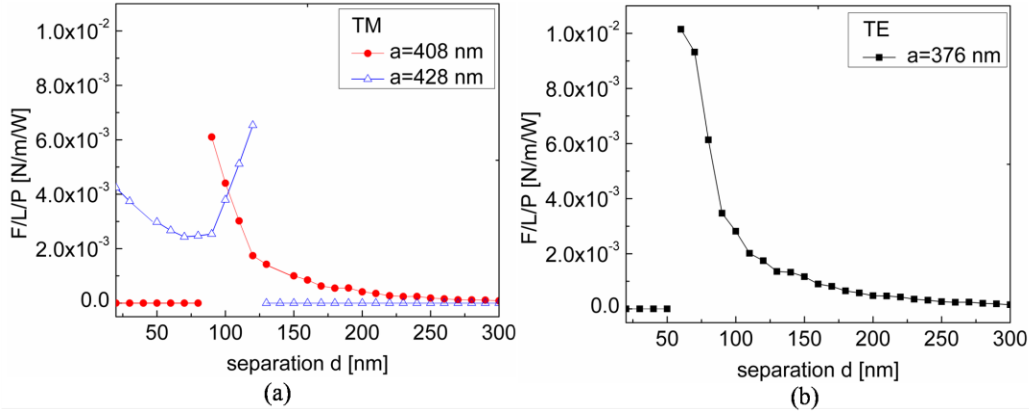


Figure 2-3 The attractive force per length per unit power as a function of distance d for (a) TM and (b) TE modes at wavelength $\lambda = 1550$ nm.

The displacement can be obtained from the calculated force values in Figure 2-3 using the analytical expression $u_m = FL^3 / 32Ewh^3$ for a doubly-clamped beam [27], where E is Young's modulus for bulk silicon. For a 60- μm long beam with cross section $376 \times 376 \text{ nm}^2$, if the waveguide-substrate separation is 100 nm, TE-polarized light with power $P=50$ mW results in a $F/L/P$ of 2.8×10^{-3} , and the displacement at the center of the waveguide is estimated to be 14.3 nm. We have verified using COMSOL finite element simulations that the displacement of the waveguide with hole radius $r=112.8$ nm is 15 nm. The discrepancy is likely due to the fact that the holes modify the beam flexibility [28].

2.3 Potential Application

In conclusion, we have studied the attractive optical force between a 1D-periodic photonic crystal waveguide and underlying silica substrate. The optical force increases as the mode approaches the light line, as for an unpatterned strip waveguide. However, the periodicity introduces two additional mechanisms for enhancing the force: reduction of the waveguide effective index and slow light enhancement near the band edge. Moreover, the shift of the waveguide mode in and out of the band gap with changes in waveguide-substrate separation give rise to non-monotonic force behavior and may enable compact optical power limiters. It is intriguing to consider whether optomechanical coupling can be used more widely to tailor optical power response. The coupling of dielectric waveguides to substrates with loss or gain, incorporating plasmonic or quantum-confined structures, may enable a variety of devices to tailor power response, such as threshold-activated switches, which only transmit above a certain power, or power regulators, which self-adjust to maintain the output transmission within a specified range.

2.4 Chapter References

- [1]. M. L. Povinelli, M. Ibanescu, S. G. Johnson, and J. D. Joannopoulos, "Slow-light enhancement of radiation pressure in an omnidirectional-reflector waveguide," *Applied Physics Letters* **85**, 1466-1468 (2004).
- [2]. M. L. Povinelli, M. Loncar, M. Ibanescu, E. J. Smythe, S. G. Johnson, F. Capasso, and J. D. Joannopoulos, "Evanescent-wave bonding between optical waveguides," *Opt. Lett.* **30**, 3042-3044 (2005).

- [3]. A. Mizrahi, and L. Schachter, "Mirror manipulation by attractive and repulsive forces of guided waves," *Opt. Express* **13**, 9804-9811 (2005).
- [4]. J. Ng, C. T. Chan, P. Sheng, and Z. Lin, "Strong optical force induced by morphology-dependent resonances," *Opt. Lett.* **30**, 1956-1958 (2005).
- [5]. M. L. Povinelli, S. G. Johnson, M. Loncar, M. Ibanescu, E. Smythe, F. Capasso, and J. D. Joannopoulos, "High-Q enhancement of attractive and repulsive optical forces between coupled whispering-gallery- mode resonators," *Opt. Express* **13**, 8286-8295 (2005).
- [6]. P. T. Rakich, M. A. Popovic, M. Soljacic, and E. P. Ippen, "Trapping, corralling and spectral bonding of optical resonances through optically induced potentials," *Nat Photon* **1**, 658-665 (2007).
- [7]. H. Taniyama, M. Notomi, E. Kuramochi, T. Yamamoto, Y. Yoshikawa, Y. Torii, and T. Kuga, "Strong radiation force induced in two-dimensional photonic crystal slab cavities," *Physical Review B* **78**, 165129 (2008).
- [8]. D. Van Thourhout, and J. Roels, "Optomechanical device actuation through the optical gradient force," *Nat Photon* **4**, 211-217 (2010).
- [9]. F. Riboli, A. Recati, M. Antezza, and I. Carusotto, "Radiation induced force between two planar waveguides," *The European Physical Journal D - Atomic, Molecular, Optical and Plasma Physics* **46**, 157-164 (2008).
- [10]. A. Mizrahi, and L. Schachter, "Electromagnetic forces on the dielectric layers of the planar optical Bragg acceleration structure," *Physical Review E* **74**, 036504 (2006).
- [11]. A. Mizrahi, and L. Schachter, "Two-slab all-optical spring," *Opt. Lett.* **32**, 692-694 (2007).
- [12]. M. Li, W. H. P. Pernice, and H. X. Tang, "Tunable bipolar optical interactions between guided lightwaves," *Nat Photon* **3**, 464-468 (2009).
- [13]. J. Roels, I. De Vlaminck, L. Lagae, B. Maes, D. Van Thourhout, and R. Baets, "Tunable optical forces between nanophotonic waveguides," *Nat Nano* **4**, 510-513 (2009).

- [14]. G. S. Wiederhecker, L. Chen, A. Gondarenko, and M. Lipson, "Controlling photonic structures using optical forces," *Nature* **462**, 633-636 (2009).
- [15]. M. Eichenfield, C. P. Michael, R. Perahia, and O. Painter, "Actuation of micro-optomechanical systems via cavity-enhanced optical dipole forces," *Nat Photon* **1**, 416-422 (2007).
- [16]. J. Rosenberg, Q. Lin, and O. Painter, "Static and dynamic wavelength routing via the gradient optical force," *Nat Photon* **3**, 478-483 (2009).
- [17]. J. Ma, and M. L. Povinelli, "Large tuning of birefringence in two strip silicon waveguides via optomechanical motion," *Opt. Express* **17**, 17818-17828 (2009).
- [18]. W. H. P. Pernice, M. Li, and H. X. Tang, "A mechanical Kerr effect in deformable photonic media," *Applied Physics Letters* **95**, 123507-123503 (2009).
- [19]. M. Li, W. H. P. Pernice, C. Xiong, T. Baehr-Jones, M. Hochberg, and H. X. Tang, "Harnessing optical forces in integrated photonic circuits," *Nature* **456**, 480-484 (2008).
- [20]. W. H. P. Pernice, M. Li, D. Garcia-Sanchez, and H. X. Tang, "Analysis of short range forces in opto-mechanical devices with a nanogap," *Opt. Express* **18**, 12615-12621.
- [21]. W. H. P. Pernice, M. Li, and H. X. Tang, "Theoretical investigation of the transverse optical force between a silicon nanowire waveguide and a substrate," *Opt. Express* **17**, 1806-1816 (2009).
- [22]. J. Chan, M. Eichenfield, R. Camacho, and O. Painter, "Optical and mechanical design of a "zipper" photonic crystal optomechanical cavity," *Opt. Express* **17**, 3802-3817 (2009).
- [23]. M. Eichenfield, R. Camacho, J. Chan, K. J. Vahala, and O. Painter, "A picogram- and nanometre-scale photonic-crystal optomechanical cavity," *Nature* **459**, 550-555 (2009).
- [24]. J. D. Joannopoulos, R. D. Meade, and J. N. Winn, *Photonic crystals : molding the flow of light* (Princeton University Press, Princeton, N.J., 1995).
- [25]. S. G. Johnson, and J. D. Joannopoulos, "Block-iterative frequency-domain methods for Maxwell's equations in a planewave basis," *Opt. Express* **8**, 173-190 (2001).

- [26]. J. D. Jackson, *Classical Electrodynamics* (Wiley, New York, 1999).
- [27]. S. Timoshenko, *Theory of elasticity* (McGraw-Hill, New York, London,, 1934).
- [28]. A. R. Day, K. A. Snyder, E. J. Garboczi, and M. F. Thorpe, "The elastic moduli of a sheet containing circular holes," *Journal of the Mechanics and Physics of Solids* **40**, 1031-1051 (1992).

Chapter 3: Mechanical Kerr Nonlinearity

3.1 Background

In the last few years, intense research has been carried out on optical forces induced by the strongly enhanced gradient of the electromagnetic field close to micro- and nanophotonic devices [1-14]. Optical forces provide a novel way to tune the properties of microphotonic devices by changing the separation between their components. This mechanical actuation allows a number of important device functionalities, such as all-optically controlled filters [15], wavelength routers [16], polarization rotators [17], and power limiters[18].

It has previously been suggested that optomechanical coupling in macroscale Fabry-Perot cavities can be viewed as an effective nonlinearity [19]. The concept can be generalized to other types of devices that move in response to optical forces. A mechanical Kerr effect has been predicted in a microphotonic Si waveguide with a suspended, movable section [20]. The mechanical Kerr coefficient n_2^m is several orders of magnitude larger than the intrinsic Kerr coefficient of silicon. The origin of the mechanical Kerr effect lies in optical coupling between the waveguide and substrate. Coupling results in an attractive optical force that pulls the waveguide closer to the substrate, changing the effective index of the waveguide mode. Since the optical force is proportional to the optical power in the waveguide, the shift in effective index depends on intensity; for this system, the mechanical Kerr coefficient is positive.

It is intriguing to explore whether microphotonic devices can be designed to tailor the value and sign of the mechanical Kerr coefficient, yielding “customizable” nonlinear materials. In this paper, we examine a coupled, two-waveguide system in which the forces can be either attractive or repulsive. We show that the mechanical Kerr coefficient scales as the optical force squared.

As a result, the mechanical Kerr coefficient is positive for either an attractive or repulsive force. The force can be expressed as a derivative of the effective index with respect to separation at fixed frequency. We calculate the mechanical Kerr coefficient numerically for varying waveguide cross sections. We find that n_2^m is greatest when the modes are neither too delocalized nor too confined in deformable waveguides. Under these conditions, the force which is enhanced by strong evanescent-wave coupling and the increased displacement give rise to the largest shift in effective index.

3.2 Coupled Waveguides Exhibiting Bipolar Optical Forces

We consider the coupled waveguides shown in Figure 3-1 (a). Two parallel, silicon strip waveguides (refractive index $n = 3.45$) are separated by a distance d . Both ends of the waveguides rest on a SiO_2 (refractive index $n = 1.5$) substrate. The suspended section has length L . Each waveguide has a cross section of dimensions $w \times h$. From previous work [2], it is known that optical coupling between the waveguides gives rise to a mechanical force. The magnitude of the force is proportional to the optical power, and the sign is either attractive or repulsive, depending on the relative phase of light in the two waveguides. The force per unit length in the suspended section can be calculated from the full-vectorial eigenmodes of the coupled waveguides using the Maxwell Stress Tensor method, as in Reference [2].

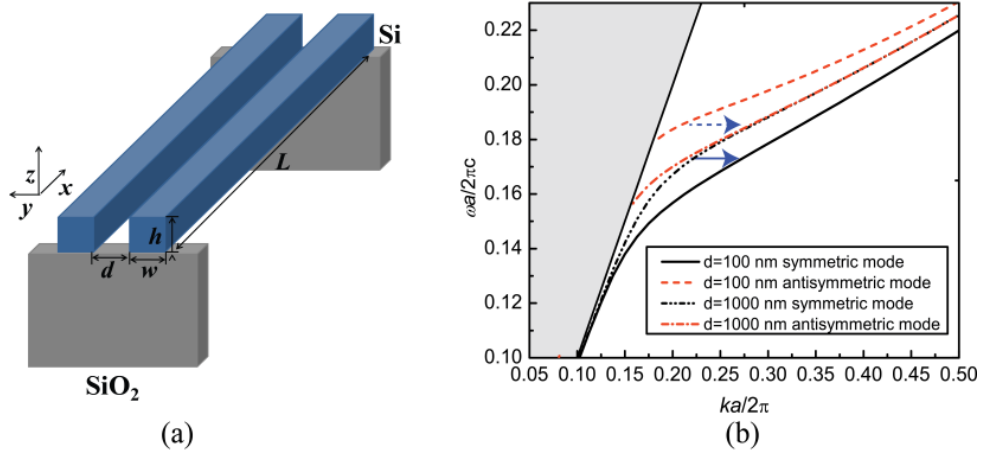


Figure 3-1 (a) Two coupled silicon waveguides, each with cross section $w \times h$, separated by a distance d and resting on a SiO_2 substrate with suspended length L . (b) Dispersion relation for modes of the suspended section. The two lowest modes with electric field vectors primarily in the z -direction are plotted for separations $d=100$ nm and $d=1000$ nm. The cross section of each waveguide is $350 \times 350 \text{ nm}^2$. The gray region shows the light cone for air.

Figure 3-1 (b) shows the dispersion relation for the two lowest-order modes that have an electric field primarily in the z -direction. Calculations were performed using the MIT Photonic Bands (MPB) package [21]. To illustrate the dependence on waveguide separation, the dispersion relation is plotted for a smaller (100nm) and larger (1000nm) value of separation d . For the lowest mode, the electric field component E_z is symmetric in the two waveguides. The symmetric mode corresponds to an attractive force. Decreasing separation shifts the dispersion relation to a larger k value, in the direction shown by the blue, solid arrow. For the second lowest mode, E_z is antisymmetric and the force is repulsive. Increasing separation also shifts the dispersion relation to larger k value, in the direction shown by the blue, dashed arrow. Below, we relate the shift in dispersion relation at fixed frequency to the optical force.

Figure 3-2 introduces notation to describe the shift in dispersion relation $\omega(k)$ resulting from a small change in waveguide separation δd . The solid and dashed lines are the initial and shifted bands, respectively. For constant frequency operation at frequency ω_0 , the magnitude of the wave vector shifts from k_0 to k_2 . If we consider a constant wave vector k_0 , the dispersion relation shifts from ω_0 to ω_1 .

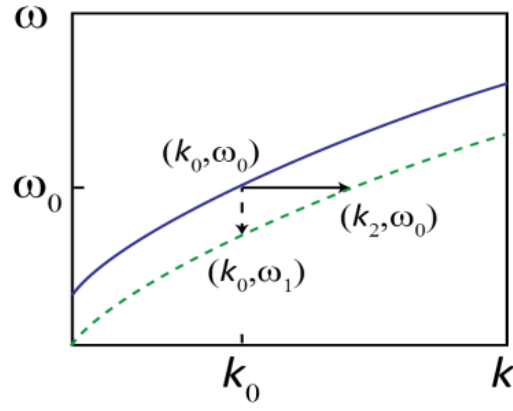


Figure 3-2 Schematic diagram showing a shift in the dispersion relation due to a change in separation between waveguides d . The solid and dashed lines represent the initial and shifted dispersion relation, respectively.

3.3 Calculation of Optical Force

For infinitely long waveguides with no radiation loss, the optical force may be calculated as a derivative of the eigenmode frequency with respect to separation [2]:

$$\frac{F}{LP} = -\frac{1}{c} \frac{n_g}{\omega} \frac{\partial \omega}{\partial d} \bigg|_k, \quad (3-1)$$

where $F/(LP)$ represents the force per length per unit power, n_g is the group index, and c is the speed of light in vacuum. Note that the derivative is taken at constant k . Equation (3-1) has been shown to agree well with direct calculations via the Maxwell Stress Tensor (MST) [22] for the coupled waveguide system [2].

By substituting $\omega = ck/n_{\text{eff}}$ into Equation (3-1), the force may alternately be expressed as a function of the effective index n_{eff} [23]:

$$\frac{F}{LP} = \frac{1}{c} \frac{n_g}{n_{\text{eff}}} \left. \frac{\partial n_{\text{eff}}}{\partial d} \right|_k. \quad (3-2)$$

We may recast the force in terms of a derivative at fixed frequency as follows. As shown by the dashed arrow in Figure 3-2, for fixed wave vector k_0 , a small change in separation δd moves the eigenmode from (k_0, ω_0) to (k_0, ω_1) , corresponding to a shift of n_{eff} :

$$\delta n_{\text{eff}}|_k = ck_0 \left(\frac{1}{\omega_1} - \frac{1}{\omega_0} \right) = ck_0 \frac{-\delta\omega}{(\omega_0 + \delta\omega)\omega_0}, \quad (3-3)$$

where $\delta\omega = \omega_1 - \omega_0$. For fixed frequency ω_0 , the shift of the dispersion relation changes the wave vector from k_0 to k_2 . The change of n_{eff} for fixed ω is:

$$\delta n_{\text{eff}}|_\omega = \frac{c}{\omega_0} (k_2 - k_0) = \frac{c}{\omega_0} \delta k, \quad (3-4)$$

where $\delta k = k_2 - k_0$. By comparing Equation (3-3) and (3-4), we find:

$$\frac{\delta n_{\text{eff}}|_k}{\delta n_{\text{eff}}|_\omega} = -\frac{\delta\omega}{\delta k} \frac{k_0}{(\omega_0 + \delta\omega)} \approx -\frac{\delta\omega}{\delta k} \frac{k_0}{\omega_0}. \quad (3-5)$$

If the band is shifted by a small amount, the ratio $\delta\omega / \delta k$ can be estimated by $-c/n_g$. (The negative sign results from the fact that $\delta\omega = \omega_1 - \omega_0$ is defined to be negative in Figure 3-2. Equation (3-5) can then be rewritten as:

$$\frac{\delta n_{\text{eff}}|_k}{\delta n_{\text{eff}}|_\omega} \approx \frac{n_{\text{eff}}}{n_g}. \quad (3-6)$$

For finite shift, Equation (3-2) can be approximated by

$$\frac{F}{LP} \approx \frac{1}{c} \frac{n_g}{n_{\text{eff}}} \frac{\delta n_{\text{eff}}}{\delta d} \bigg|_k. \quad (3-7)$$

Substituting Equation (3-6) into Equation (3-7) and taking the limit as $\delta d \rightarrow 0$ yields the result

$$\frac{F}{LP} = \frac{1}{c} \frac{\partial n_{\text{eff}}}{\partial d} \bigg|_\omega, \quad (3-8)$$

showing that the optical force can be calculated in terms of the effective index $n_{\text{eff}}(d)$ at a fixed optical frequency. Negative values here correspond to attractive forces. Reference [13] used a different derivation, based on energy and photon-number conservation, to arrive at the same expression.

We compared force values calculated with Equation (3-8) to those calculated using the MST method. The wavelength was fixed to 1550 nm and the waveguide dimensions to $h=w=350$ nm. The derivative in Equation (3-8) was approximated as a finite difference, using values of $n_{\text{eff}}(d)$ calculated with the MPB package. Figure 3-3 (a) shows $n_{\text{eff}}(d)$ for the symmetric mode (black line). The force calculated using Equation (3-8) is plotted in Figure 3-3 (a) (red triangles). It agrees well with the force calculated using the MST method (red curve). The MST was evaluated using the full vectorial eigenmodes obtained from MPB. As predicted by Equation (3-8), the force is attractive (negative), corresponding to a decreasing $n_{\text{eff}}(d)$.

Figure 3-3 (b) shows n_{eff} (black curve) and $F/(LP)$ for the antisymmetric mode. Forces calculated by Equation (3-8) (red triangles) agree well with values calculated using the MST

method (red curve). Note that the value of n_{eff} first decreases and then increases as a function of d . Correspondingly, the derivative $\partial n_{\text{eff}} / \partial d|_{\omega}$ turns from negative to positive, and the optical force changes from negative (attractive) to positive (repulsive) as a function of separation. We emphasize that the sign of the force can be easily inferred from the slope of n_{eff} .

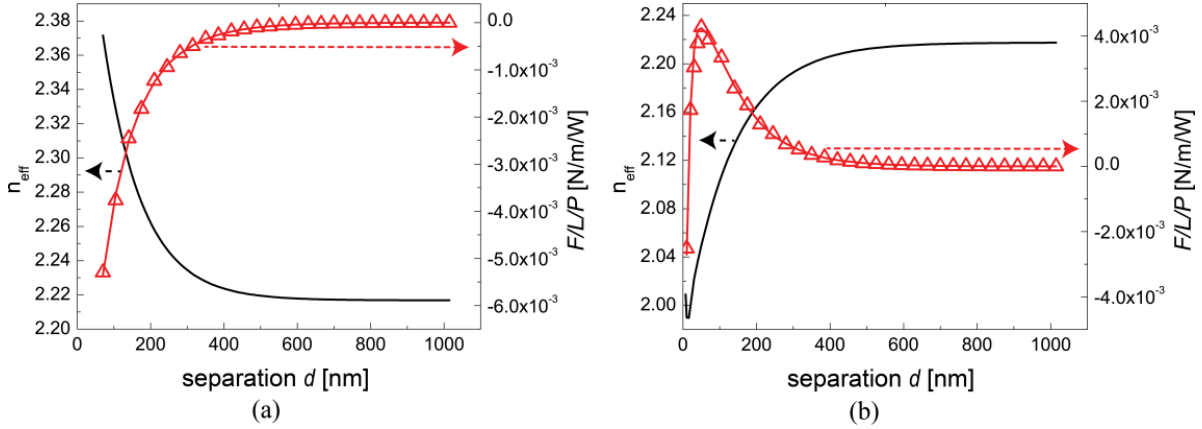


Figure 3-3 For fixed wavelength 1550 nm and waveguide dimensions $h=w=350$ nm: (a) Symmetric mode: n_{eff} as a function of d (black curve); $F/(LP)$ calculated by the MST method (red curve) and by Equation (3-8) (red triangles). (b) Antisymmetric mode: n_{eff} as a function of d (black curve); $F/(LP)$ calculated by the MST method (red curve) and by Equation (3-8) (red triangles).

3.4 Calculation of Mechanical Kerr Coefficient

The mechanical Kerr effect arises from the change in effective index due to waveguide deformation. We consider static deformations. The optical force between the waveguides is proportional to the power, P , and causes the waveguides to deform. For the symmetric mode, the force is attractive and the waveguides are pulled together. For the antisymmetric mode, the force is repulsive and the waveguides are pushed apart. The maximum deformation will be at the center of the waveguide, since the ends of the waveguides are fixed to the silica substrate. We

consider the case where the deformation is small compared to the initial separation. The magnitude of the deformation is also much smaller than the length of the suspended region, L . Under deformation, the effective index n_{eff} varies along the length of the waveguides, according to the local separation. Following Reference [10], we define the mechanical Kerr coefficient n_2^m through the relation $\Delta n_{\text{eff}}(I) = n_2^m I$, where $\Delta n_{\text{eff}}(I)$ is the change in the effective index at the center of the suspended region, and I is the light intensity. Specifically, we take $I = P/A$, where A is the mode area, equal to $\left(\iint \epsilon(y,z) |E|^2 dydz \right) / \max(\epsilon |E|^2)$.

Using Equation (3-8), which relates the force to the derivative of the effective index with respect to separation, we can show that either an attractive or repulsive force gives rise to a positive mechanical Kerr coefficient. Figure 3-3 (a) shows that for the symmetric mode, n_{eff} decreases with d . From Equation (3-8), the force is negative (attractive) and pulls the waveguides closer together. The separation at the center of the suspended length decreases, resulting in an increase in n_{eff} . The mechanical Kerr coefficient n_2^m is thus positive. For the antisymmetric mode, in the region where n_{eff} decreases with d , the same argument shows that n_2^m is positive. In the region where n_{eff} increases with d , the force is positive (repulsive), which increases the separation at the center of the suspended region and increases n_{eff} . Again, a positive mechanical Kerr coefficient n_2^m is obtained.

The mechanical Kerr coefficient can be evaluated numerically from the value of the optical force. When the deformation is small with respect to the initial separation, the change of the effective index for a signal with fixed frequency can be approximated by:

$$\Delta n_{\text{eff}} = \Delta d \times \left. \frac{\partial n_{\text{eff}}}{\partial d} \right|_{\omega}, \quad (3-9)$$

where Δd is the change in separation, equal to twice the deformation of a single waveguide, which can be modeled as a double-clamped beam [24]:

$$\Delta d = 2 \times (F L^3 / 32 E h w^3), \quad (3-10)$$

where E is the Young's modulus of silicon. By manipulating Equations (3-8), (3-9) and (3-10), we get

$$\Delta n_{\text{eff}} = \frac{1}{c} \left(\frac{\partial n_{\text{eff}}}{\partial d} \right)^2 \frac{P L^4}{16 E h w^3}, \quad (3-11)$$

or

$$\Delta n_{\text{eff}} = c \left(\frac{F}{L P} \right)^2 \frac{P L^4}{16 E h w^3}. \quad (3-12)$$

The mechanical Kerr coefficient is

$$n_2^m = \frac{\Delta n_{\text{eff}}}{I} = c \left(\frac{F}{L P} \right)^2 \frac{L^4}{16 E h w^3} A. \quad (3-13)$$

Note that $F/(LP)$ depends on the initial separation d and the waveguide cross section parameters, h and w . The parameter n_2^m also explicitly depends on the waveguide geometry parameters h , w , and L .

Note that Equation (3-13) provides another means of seeing that both attractive and repulsive forces give positive mechanical Kerr coefficient: n_2^m depends on $(F/(LP))^2$.

3.5 Symmetric Mode

In this section, we discuss how to design the waveguide cross section parameters h and w to enhance $F/(LP)$ and n_2^m for the symmetric mode. We set $\lambda = 1550$ nm, $L = 20$ μm , initial separation $d = 100$ nm, and $P = 10$ mW.

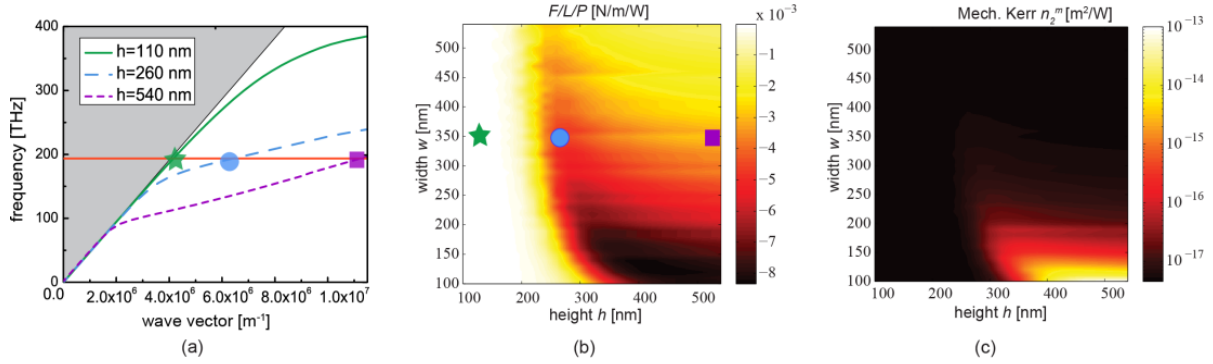


Figure 3-4 Symmetric mode: (a) Band structure. The gray region represents the air light cone. The red line shows fixed wavelength 1550 nm (frequency 193.55 THz). (b) Attractive force per length per unit power $F/(LP)$. The initial separation $d=100$ nm, suspended length $L=20$ μm , optical power $P = 10$ mW, and the signal wavelength is 1550 nm. (c) Mechanical Kerr coefficient n_2^m .

Figure 3-4 (b) shows $F/(LP)$ for the symmetric mode in waveguides with various heights and widths.

The strongest attractive force is shown by the darkest region, which corresponds to waveguides with large heights and small widths. To understand the mechanism behind the force enhancement, we plot the dispersion relation of the mode in Figure 3-4 (a). For a waveguide with $h = 260$ nm and $w = 350$ nm, marked by the circle in Figure 3-4 (b), $F/(LP)$ has a relatively large, negative value of -4.1×10^{-3} N/m/W. The corresponding point in the dispersion relation is below and close to the air light line, as indicated by the circle in Figure 3-4 (a).

Figure 3-4 (b) shows that if the waveguide cross section is too large, the attractive force is decreased (yellow region). As marked by the square in Figure 3-4 (b), when $h = 540$ nm and $w = 350$ nm, $F/(LP)$ is reduced to -2.7×10^{-3} N/m/W. The mode in such a system is well below the air light line. The light is confined in the two waveguides, with minimal optical coupling between them, and the magnitude of the force is decreased.

The white region of Figure 3-4 (b) shows that when the waveguide cross section is too small, the force magnitude is less than 10^{-3} N/m/W. For example, $F/(LP)$ on the waveguide with $h = 110$ nm and $w = 350$ nm (marked by the star) is on the order of 10^{-5} N/m/W. Figure 3-4 (a) shows that the mode is on the asymptote of the light line. The mode energy spreads into the surrounding air, giving rise to a small force. In order to achieve a larger attractive force, we can design the waveguide cross section to make the optical mode approach the air light line but not overlap with the light line, as indicated by the circle in Figure 3-4 (a).

The mechanical Kerr coefficient n_2^m can be determined from the force by using Equation (3-13) and is shown in Figure 3-4 (c). The biggest n_2^m in Figure 3-4 (c) is over 40,000 times bigger than the intrinsic Kerr coefficient of silicon, equal to 4.5×10^{-18} m²/W. The value of n_2^m is largest when the optical force is strong and the waveguide width is small. A thin waveguide is more deformable to the optical force along the y direction. For example, $F/(LP)$ for a waveguide of $h = 400$ nm and $w = 200$ nm is -6.7×10^{-3} N/m/W, which has the same order of magnitude as $F/(LP) = -7.2 \times 10^{-3}$ N/m/W for a waveguide of $h = 400$ nm and $w = 100$ nm. However, by reducing w from 200 nm to 100 nm, we can increase n_2^m from 2.4×10^{-14} m²/W to 1.7×10^{-13} m²/W.

3.6 Antisymmetric Mode

We calculated $F/(LP)$ and n_2^m for the antisymmetric mode for waveguides with various heights and widths. We only consider guided (non-leaky) modes, lying underneath the light cone.

Figure 3-5 (b) shows $F/(LP)$. The force is positive (repulsive). The bright region indicates the combination of waveguide heights and widths that result in relatively large optical force for 1550-nm light. The blue curve indicates the conditions for mode cutoff: a guided mode exists only above and to the right of the curve. Large forces can be obtained by choosing cross-sectional parameters on the upper, right boundary of the curve. For example, for $h = 320$ nm and $w = 250$ nm, marked by the circle in Figure 3-5 (b), $F/(LP)$ is 9.5×10^{-3} N/m/W. The corresponding mode in the dispersion relation lies close to and below the light line, as indicated by the circle in Figure 3-5 (a).

The repulsive force decreases for waveguides with cross-sectional dimensions much larger than cutoff. As marked by the square in Figure 3-5 (b), when $h = 540$ nm and $w = 250$ nm, $F/(LP)$ is reduced to 5.7×10^{-3} N/m/W. The mode energy is confined in the waveguides, and the light intensity in the air gap is reduced, decreasing the optical force. If the waveguide cross-sectional dimension is too small, as marked by the star in Figure 3-5 (b) for $h = 110$ nm and $w = 250$ nm, the mode becomes leaky.

Figure 3-5 (c) shows that the sign of n_2^m induced by a repulsive force is positive for various cross-sectional dimensions. In order to increase n_2^m , we should choose dimensions on the right boundary of the blue curve and reduce w to make the waveguides more deformable. For example, if we choose $h=540$ nm and $w=140$ nm, n_2^m is approximately 8.1×10^{-13} m²/W, which is more than 150,000 times larger than the intrinsic Kerr coefficient of silicon.

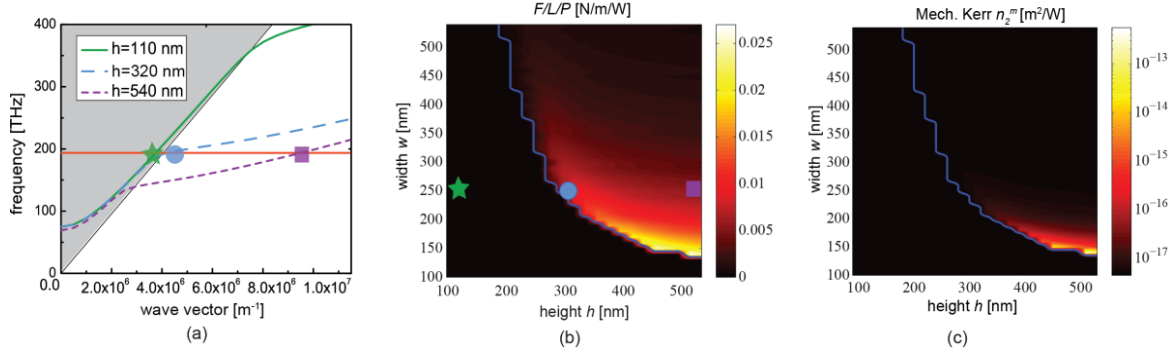


Figure 3-5 Anti-symmetric mode: (a) Band structure. The gray region represents the air light cone. The red line shows fixed wavelength 1550 nm (frequency 193.55 THz). (b) Repulsive force per length per unit power $F/(LP)$. The initial separation $d=100$ nm, suspended length $L = 20$ μm , optical power $P = 10$ mW, and the signal wavelength is 1550 nm. (c) Mechanical Kerr coefficient n_2^m .

3.7 Discussion

Above, we have shown that for fixed waveguide length and initial separation, we can increase the mechanical Kerr coefficient n_2^m by adjusting the waveguide width and height. From Equations (3-8) and (3-9), we may infer that n_2^m is proportional to the product of the optical force F and the waveguide displacement Δd . The mechanical Kerr nonlinearity can thus be enhanced by i), increasing the optical force and ii), making the waveguide more deformable.

Figures 3-4 (b) and 3-5 (b) show that the force depends on waveguide cross-section dimensions. For either the symmetric or anti-symmetric modes, decreasing the waveguide height at fixed width shifts the mode closer to the light line. For the symmetric mode, the largest force is obtained when the mode is close to, but not too close to, the light line. For the anti-symmetric mode, the largest force is obtained when the mode approaches the cut-off geometry (blue line), where the mode crosses the light line. We may interpret both these conditions as meaning that

the modes should be neither too delocalized in the surrounding air, nor too confined inside the waveguides, to optimize coupling between the waveguides and produce a large force. Meanwhile, the waveguide can also be made more deformable by adjusting waveguide dimensions. Equation (3-10) indicates that Δd is inversely proportional to hw^3 . Overall, the largest n_2^m values are obtained for small values of the width w (Figures 3-4 (c) and 3-5 (c)).

We have presented results for both the symmetric and anti-symmetric mode. Both modes give positive mechanical Kerr coefficients n_2^m , and the maximum values are both on the order of $10^{-13} \text{ m}^2/\text{W}$. Comparing Figures 3-4 (c) and 3-5 (c), we observe that the symmetric mode has a bigger, brighter region representing n_2^m greater than $10^{-14} \text{ m}^2/\text{W}$. In other words, to realize the same value of n_2^m , there is greater flexibility in waveguide dimensions using the symmetric mode. Another reason to choose the symmetric mode is that exciting the antisymmetric mode increases device complexity; for example, it has been demonstrated that a Mach-Zender interferometer can be used to control the phase difference between light incident in the two waveguides [10, 14].

Note that the optical frequency is many orders of magnitude larger than the mechanical resonance frequency, which is in the MHz range. Because the instantaneous optical force oscillates much faster than the mechanical motion, we consider the effect of the time-averaged, or “smoothed,” optical force on the waveguides, where the average is taken over the optical cycle. Assume the incident power is switched on and remains fixed. Driven by the optical force, the waveguides will start to deform. A steady-state displacement will be reached after a period of time proportional to the mechanical quality factor divided by the mechanical resonance frequency. In this paper, we focus on the static mechanical Kerr coefficient n_2^m caused by the

steady-state displacement. However, for fixed power, larger displacements can be obtained by modulating the incident optical power at the mechanical resonance frequency [20]. The displacement will vary as a function of time throughout the period of mechanical vibration. At the peak displacement value, the instantaneous n_2^m reaches its maximum. The coefficient n_2^m will be increased by a factor of Q_{mech} with respect to the case of static displacement, where Q_{mech} is the mechanical quality factor. However, if the average mechanical displacement is zero, the average value of n_2^m will also be zero.

3.8 Summary

We have investigated mechanical Kerr effects in a coupled-waveguide system exhibiting both attractive and repulsive forces. The optical force can be related to the change in effective index with separation at frequency. This formulation makes it clear that either an attractive or repulsive force gives rise to a positive mechanical Kerr coefficient. Values several orders of magnitude larger than the intrinsic Kerr coefficient are obtained for waveguides in which the optical mode approaches the air light line.

Since the mechanical Kerr effect results from physical motion, the time scale for response will be slower than for the intrinsic Kerr nonlinearity. At the same time, however, the magnitude is orders of magnitude larger. This suggests the potential for the design of ultra-low threshold, integrated optical devices such as all-optical transistors and isolators [25] that use the mechanical Kerr effect. Such devices might respond to the *average* power in an optical data stream, where

the time-average is related to the time scale for mechanical response, and ultimately find use in the regulation of on-chip optical networks.

3.9 Chapter References

- [1]. M. L. Povinelli, M. Ibanescu, S. G. Johnson, and J. D. Joannopoulos, "Slow-light enhancement of radiation pressure in an omnidirectional-reflector waveguide," *Applied Physics Letters* **85**, 1466-1468 (2004).
- [2]. M. L. Povinelli, M. Loncar, M. Ibanescu, E. J. Smythe, S. G. Johnson, F. Capasso, and J. D. Joannopoulos, "Evanescent-wave bonding between optical waveguides," *Opt. Lett.* **30**, 3042-3044 (2005).
- [3]. A. Mizrahi, and L. Schachter, "Mirror manipulation by attractive and repulsive forces of guided waves," *Opt. Express* **13**, 9804-9811 (2005).
- [4]. J. Ng, C. T. Chan, P. Sheng, and Z. Lin, "Strong optical force induced by morphology-dependent resonances," *Opt. Lett.* **30**, 1956-1958 (2005).
- [5]. M. L. Povinelli, S. G. Johnson, M. Loncar, M. Ibanescu, E. Smythe, F. Capasso, and J. D. Joannopoulos, "High-Q enhancement of attractive and repulsive optical forces between coupled whispering-gallery- mode resonators," *Opt. Express* **13**, 8286-8295 (2005).
- [6]. P. T. Rakich, M. A. Popovic, M. Soljacic, and E. P. Ippen, "Trapping, corralling and spectral bonding of optical resonances through optically induced potentials," *Nat Photon* **1**, 658-665 (2007).
- [7]. H. Taniyama, M. Notomi, E. Kuramochi, T. Yamamoto, Y. Yoshikawa, Y. Torii, and T. Kuga, "Strong radiation force induced in two-dimensional photonic crystal slab cavities," *Physical Review B* **78**, 165129 (2008).
- [8]. D. Van Thourhout, and J. Roels, "Optomechanical device actuation through the optical gradient force," *Nat Photon* **4**, 211-217 (2010).

- [9]. F. Riboli, A. Recati, M. Antezza, and I. Carusotto, "Radiation induced force between two planar waveguides," *The European Physical Journal D - Atomic, Molecular, Optical and Plasma Physics* **46**, 157-164 (2008).
- [10]. M. Li, W. H. P. Pernice, and H. X. Tang, "Tunable bipolar optical interactions between guided lightwaves," *Nat Photon* **3**, 464-468 (2009).
- [11]. G. S. Wiederhecker, L. Chen, A. Gondarenko, and M. Lipson, "Controlling photonic structures using optical forces," *Nature* **462**, 633-636 (2009).
- [12]. M. Li, W. H. P. Pernice, C. Xiong, T. Baehr-Jones, M. Hochberg, and H. X. Tang, "Harnessing optical forces in integrated photonic circuits," *Nature* **456**, 480-484 (2008).
- [13]. P. T. Rakich, M. A. Popovic, and Z. Wang, "General treatment of optical forces and potentials in mechanically variable photonic systems," *Opt. Express* **17**, 18116-18135 (2009).
- [14]. J. Roels, I. De Vlaminck, L. Lagae, B. Maes, D. Van Thourhout, and R. Baets, "Tunable optical forces between nanophotonic waveguides," *Nat Nano* **4**, 510-513 (2009).
- [15]. M. Eichenfield, C. P. Michael, R. Perahia, and O. Painter, "Actuation of micro-optomechanical systems via cavity-enhanced optical dipole forces," *Nat Photon* **1**, 416-422 (2007).
- [16]. J. Rosenberg, Q. Lin, and O. Painter, "Static and dynamic wavelength routing via the gradient optical force," *Nat Photon* **3**, 478-483 (2009).
- [17]. J. Ma, and M. L. Povinelli, "Large tuning of birefringence in two strip silicon waveguides via optomechanical motion," *Opt. Express* **17**, 17818-17828 (2009).
- [18]. J. Ma, and M. L. Povinelli, "Effect of periodicity on optical forces between a one-dimensional periodic photonic crystal waveguide and an underlying substrate," *Applied Physics Letters* **97**, 151102-151103 (2010).
- [19]. P. Meystre, E. M. Wright, J. D. McCullen, and E. Vignes, "Theory of radiation-pressure-driven interferometers," *J. Opt. Soc. Am. B* **2**, 1830-1840 (1985).

- [20]. W. H. P. Pernice, M. Li, and H. X. Tang, "A mechanical Kerr effect in deformable photonic media," *Applied Physics Letters* **95**, 123507-123503 (2009).
- [21]. S. Johnson, and J. Joannopoulos, "Block-iterative frequency-domain methods for Maxwell's equations in a planewave basis," *Opt. Express* **8**, 173-190 (2001).
- [22]. J. D. Jackson, *Classical electrodynamics* (Wiley, New York, 1999).
- [23]. W. H. P. Pernice, M. Li, and H. X. Tang, "Theoretical investigation of the transverse optical force between a silicon nanowire waveguide and a substrate," *Opt. Express* **17**, 1806-1816 (2009).
- [24]. S. Timoshenko, *Theory of elasticity* (McGraw-Hill, New York, London,, 1934).
- [25]. M. Soljacic, C. Luo, J. D. Joannopoulos, and S. Fan, "Nonlinear photonic crystal microdevices for optical integration," *Opt. Lett.* **28**, 637-639 (2003).

Chapter 4: Large Tuning of Birefringence

4.1 Background

Optical forces have recently been investigated as a way of repositioning microphotonic elements such as waveguides [1-4] and microcavities [5-8]. In coupled waveguides or microcavities, the force can show either attractive or repulsive behavior depending on the relative phase of the incident light in each waveguide or microcavity. As a result, waveguide (or cavity) separation can be adjusted by tuning the power and/or polarization of input light.

Experiments have now demonstrated motion induced by optical forces in a variety of microphotonic systems. Eichenfield et al. [9] achieved micron-scale displacement of a micrometer-scale waveguide evanescently coupled to a high-Q optical microresonator at milliwatt optical powers. Li et al. demonstrated attractive and repulsive optical forces between a suspended waveguide and dielectric substrate, actuated by a pulsed light source [10-12]. Attractive and repulsive forces have also been observed in stacked microring structures [13], where Wiederhecker et al. achieved static displacements up to 12 nm. Optomechanical modes have been analyzed [14] and measured [15] in doubly-clamped beam structures with linear arrays of etched air holes forming optically resonant cavities. As the field of optical forces in integrated photonic devices matures, it is important to map out the novel functionalities that this relatively new form of mechanical actuation allows.

In this section, we study the use of optical forces to achieve highly tunable birefringence in a coupled waveguide system. Birefringence refers to differences in propagation between orthogonally polarized modes. Phase birefringence, the difference between the phase indices,

induces a relative phase shift between orthogonal components of incident light, which may be used for polarization rotators in optical communication systems. Group birefringence, defined as the difference between the group indices of different polarizations, leads to a polarization-dependent time delay and can be exploited to realize polarization-sensitive delay lines, splitters, and multiplexers. It has previously been observed that silicon waveguides with multiple etched slots exhibit giant birefringence behavior, with a group index difference as large as 1.5 between TE and TM polarized light [16]. The magnitude of birefringence depends on the slot width, as well as other design parameters. However, after the device is fabricated, the slot width is fixed, as is the value of the birefringence. Here, we present an optomechanically-controlled system which resembles a suspended one-slot waveguide with an adjustable slot width that depends on the optical force and exhibits highly tunable birefringence.

A variety of methods have been used to achieve tunable birefringence, including thermal and stress tuning. However, the achievable tuning range is generally small. For example, thermal tuning of polymer-filled microstructured fibers [17, 18] and photonic liquid crystal fibers [19] yields changes in birefringence on the order of 10^{-4} . For microphotonic devices, Tsia et al. [20] demonstrated dynamic control of birefringence on the order of 10^{-4} in a silicon waveguide by electrically tuning the stress on the waveguide core using an integrated piezoelectric film. Recently, Kumar et al. [21] varied the air-core thickness in a 3D hollow waveguide via MEMS actuation to offer a large birefringence of 0.012 with a tuning range of 0.01. This result points to the relatively large changes in birefringence that can be achieved using mechanical motion to physically change the waveguide geometry.

In this work, we calculate the tunable birefringence that can be achieved by using an optical force to adjust the separation between parallel, suspended, strip silicon waveguides. The force arising from the evanescent coupling between the modes of the two waveguides deforms both waveguides, changing the air-slot width. Such behavior results in all-optically adjustable giant birefringence. In Subsection 4.2, we characterize the two-waveguide system, and optimize the frequency and polarization of input light to achieve a considerable optical force at a moderate laser power. We calculate the resultant displacement of both waveguides based on the finite-element method (FEM). In Subsections 4.3 and 4.4, we respectively evaluate the performance of the optimized optical force in tuning phase and group birefringence. We show that the optomechanical approach is characterized by widely tunable birefringence. We explore the applications of the two-waveguide system for tunable linear-to-circular polarization conversion and polarization-dependent delay.

4.2 Design Method

Figure 4-1 (a) shows two parallel silicon strip waveguides (refractive index $n=3.45$) separated by a distance d . Both ends of the waveguides rest on a SiO_2 substrate, with a free-standing section of length L . Each waveguide has a cross section of dimensions $w \times h$. We consider the transverse electric (TE) mode with electric field vector primarily parallel to the air slot (\mathbf{E}_y), and the transverse magnetic (TM) mode with electric field vector primarily perpendicular to the slot (\mathbf{E}_z). We first consider the case where the cross section of each waveguide is square ($w=h=a$). Figure 4-1 (b) shows the dispersion relation calculated by the MIT Photonic Bands package for the lowest TE and TM mode for several different separations.

We only consider the guided modes lying below the light cone (yellow). The insets illustrate the E_y field distribution of the TE mode and the E_z field distribution of the TM mode, respectively. TM-polarized light is concentrated in the air region, satisfying the continuity condition on the normal component of the displacement field at the silicon-air interface [22, 23].

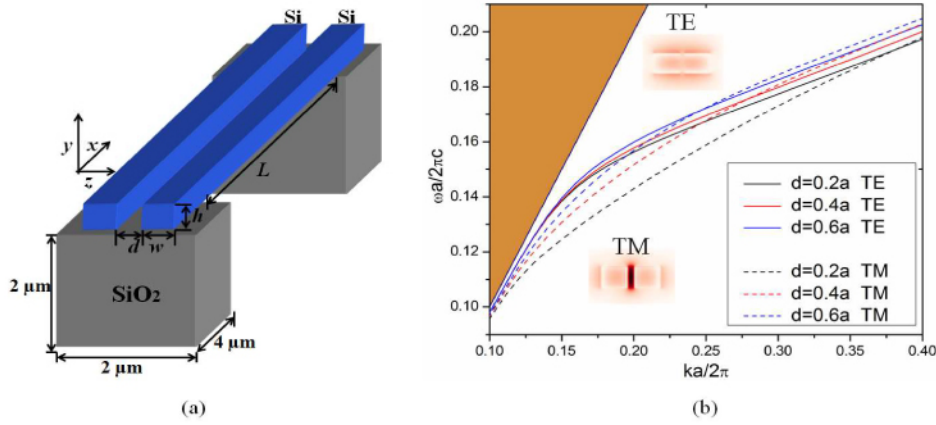


Figure 4-1 (a) Two coupled Si waveguides, each with cross section $w \times h$ separated by a distance d , rest on a SiO_2 substrate with a free-standing section of length L . (b) Dispersion relation for the lowest-frequency TE mode (solid lines) and TM mode (dashed lines) of the coupled waveguides for several separations. Insets respectively show the E_y field distribution of the TE mode and the E_z field distribution of the TM mode with $d=0.2a$ at frequency $\omega a/2\pi c=0.18$ (darker shades correspond to larger magnitudes of the electric field at a snapshot in time). The yellow region shows the light cone.

TE and TM modes have different propagation characteristics. The group birefringence is obtained by taking the difference between the group indices $\Delta n_g = n_g^{TE} - n_g^{TM}$, where n_g^{TE} and n_g^{TM} are the group indices of the TE and TM modes, respectively, at a fixed frequency ω . The group index is calculated as $n_g^{TE, TM} = c / (d\omega / dk)^{TE, TM}$ and is proportional to the reciprocal of the slope of the dispersion curve in Figure 4-1 (b). Phase birefringence is $\Delta n_p = n_p^{TE} - n_p^{TM}$, where n_p^{TE} and

n_p^{TM} respectively denote the phase indices of the TE and TM modes at a fixed frequency ω . The phase index is calculated by $n_p^{TE,TM} = ck^{TE,TM} / \omega$. For small separation ($d=0.2a$), the optical fields in the two strips are strongly coupled. The bands for TE and TM light are significantly different. It can be inferred from the figure that group and phase birefringence are relatively large in some frequency ranges. If the separation is increased ($d=0.4a$ or $d=0.6a$), the coupling between the strips becomes weaker, and the dispersion curves of TE and TM modes are closer to one another. Group and phase birefringence are reduced. For infinite waveguide separation ($d=\infty$), no coupling occurs. Modes propagate independently in each single-strip waveguide. The bands of the TE and TM modes overlap, and the birefringence vanishes.

Coupling between the strips gives rise to an optical force on the waveguides. The force depends on the frequency of light propagating in the waveguides (pump frequency), the incident power, and the waveguide separation. For fixed incident power and waveguide separation, we optimize the force magnitude by selecting an appropriate frequency and polarization of pump light. As in previous work [1], we calculate the force as a function of frequency using the Maxwell Stress Tensor formulation [24], which gives the force as an integral expression over the electric and magnetic fields of the waveguides. We solve for the full vectorial fields using the MIT Photonic Bands package. Figure 4-2 (a) shows the force magnitude as a function of the pump frequency for a waveguide separation $d = 0.35a$. We focus on the dimensionless frequency ($\omega a / 2\pi c$) range from 0.15 to 0.21. For lower frequencies, the bands are closer to the light line, and the waveguide modes spread out in the surrounding air. For frequencies larger than 0.21, there are at least two symmetric TE (or TM) modes for a single frequency, resulting in multimodal coupling. We compare the force induced by TM (red) and TE (black) modes. The

strongest force is obtained for TM-polarized light at frequency $\omega_p a / 2\pi c = 0.165$. According to Equation (4-1),

$$F = - \frac{1}{\omega} \frac{d\omega}{d\xi} \bigg|_k U \quad (4-1)$$

which indicates the mechanical force F is proportional to the derivative of frequency ω with respect to waveguide separation ξ for conserved wave vector k and energy U . In Figure 4-1 (b), we see that for a fixed wave vector k , if the waveguide separation is reduced, the frequency of the TM mode changes more than that of the TE mode. Therefore, the TM mode induces a bigger force. In the remainder of the paper, we will assume that TM pump light is used to exert force on the waveguides and deform their shape. We will consider the effects of the deformation on the propagation of both TE and TM signal light.

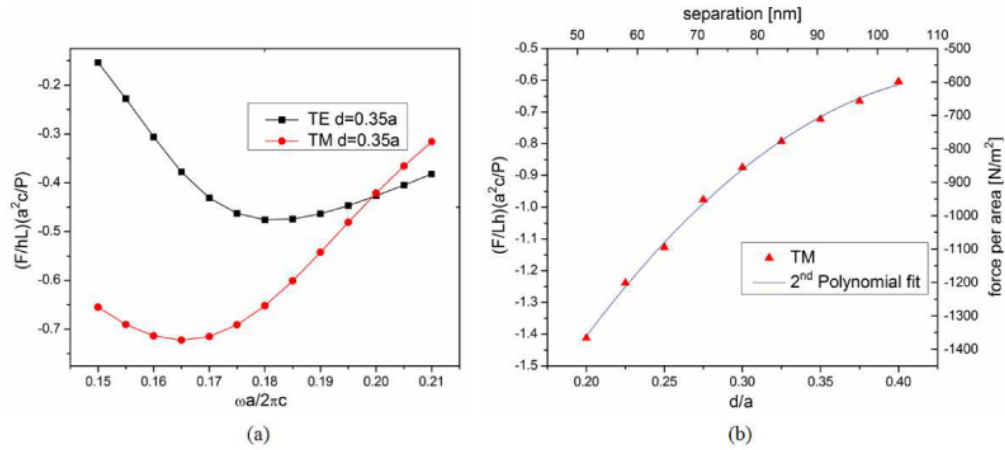


Figure 4-2 (a) Normalized force per unit area for the lowest-frequency TE (red) and TM (black) modes as a function of pump light frequency, at fixed separation $d=0.35a$. (b) Force per unit area as a function of separation (red triangles), at optimized frequency $\omega_p a / 2\pi c = a / \lambda_p = 0.165$. The right and top axes are in physical units with incident power $P=20$ mW, $w=h=a=263.5$ nm, and $L=30$ μm . The blue solid line is the second-order polynomial fit of the force per unit area.

On the left and bottom axes of Figure 4-2 (b), we plot the dimensionless force per unit area $(F/Lh)(a^2c/P)$ as a function of the normalized separation d/a at the optimized frequency $\omega_p a/2\pi c=0.165$. The symbol c represents the speed of light in vacuum, and P denotes the incident power. Substituting the values $P=20\text{mW}$, $w=h=a=263.5\text{nm}$, and pump wavelength $\lambda_p=1597\text{nm}$, we plot the force per unit area versus separation on the right and top axes in Figure 4-2 (b).

We perform FEM numerical simulations to calculate the deformation of waveguides caused by the attractive force using COMSOL Multiphysics software. We simulate the full three-dimensional structure consisting of two silicon waveguides, each with a square cross section of $263.5 \times 263.5 \text{ nm}^2$ and a length of $30\mu\text{m}$. The ends of each waveguide are fixed. We assume an initial waveguide separation $d=0.35a=92.2 \text{ nm}$. The waveguide ends are fixed at this separation. The optical force pulls the waveguides toward one another. As the waveguides deform, the magnitude of the force increases. We use a second-order polynomial to approximate the force density for waveguide separation d between $0.2a$ and $0.35a$, as shown by the solid blue line in Figure 4-2 (b). For the mechanical parameters of Si, we take the mass density $\rho=2330 \text{ kg/m}^3$ and Young's modulus $E=131 \text{ GPa}$. Figure 4-3 shows the waveguide deformation as a function of position along the waveguides with $L=30 \mu\text{m}$, $w=h=a=263.5 \text{ nm}$, $d=92.2 \text{ nm}$, and $P=20 \text{ mW}$. The biggest displacement (9 nm) is obtained at the waveguide center. The smallest distance between the two waveguides is 74.2 nm . Following [25], we estimate the van der Waals force per unit area to be approximately 25 N/m^2 between two parallel infinitely extended Si slabs of thickness 263.5 nm and separation 74.2 nm . For this separation, the van der Waals force is several orders of magnitude less than the optically-induced force and can therefore be neglected.

It is interesting to note that experiments have been done in a similar coupled system, showing that pulsed light can obtain a comparable displacement at a lower power of a few milliwatts [10].

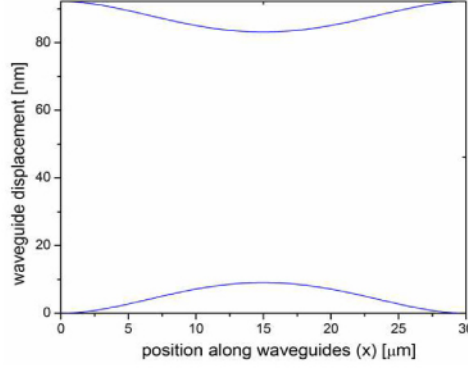


Figure 4-3 Displacement of the suspended section of each waveguide as a function of position along the waveguide. The cross-sectional dimension is $w=h=a=263.5\text{ nm}$, the initial waveguide separation is $d=0.35a=92.2\text{ nm}$, the pump frequency is $\omega_p a/2\pi c=a/\lambda_p=0.165$, the incident power is $P=20\text{ mW}$, and the suspended length is $L=30\text{ }\mu\text{m}$. Note that the x and y axes differ in scale.

4.3 Tunable Phase Birefringence

The phase birefringence is a function of the separation between the strips. We consider the birefringence experienced by light at a signal frequency ω . We assume that the signal power is much weaker than the pump power, such that the optical force due to the signal can be neglected. We calculate the phase birefringence Δn_p as a function of dimensionless signal frequency $\omega a/2\pi c$ for different separations from $0.2a$ to $0.35a$, as shown in Figure 4-4 (a). The arrow indicates that at signal frequency $\omega_s a/2\pi c=0.17$ ($a=263.5\text{ nm}$, $\lambda_s=1550\text{ nm}$), the absolute value of Δn_p increases as the waveguide separation decreases.

When the waveguides are deformed by an attractive optical force, the separation varies along the waveguide length as shown in Figure 4-3. The propagating signal experiences a spatially-varying birefringence. Figure 4-4 (b) shows the phase birefringence as a function of position

along waveguides for a CW pump at frequency $\omega_p a/2\pi c=0.165$ with power $P=20$ mW. For zero pump power (zero force), the waveguides are parallel and the birefringence is 0.067 throughout the whole free-standing section. With the pump on, the birefringence is increased. The maximum value is approximately 0.093 at the waveguide center. The difference between the maximum and the minimum of $|\Delta n_p|$ is 0.026.

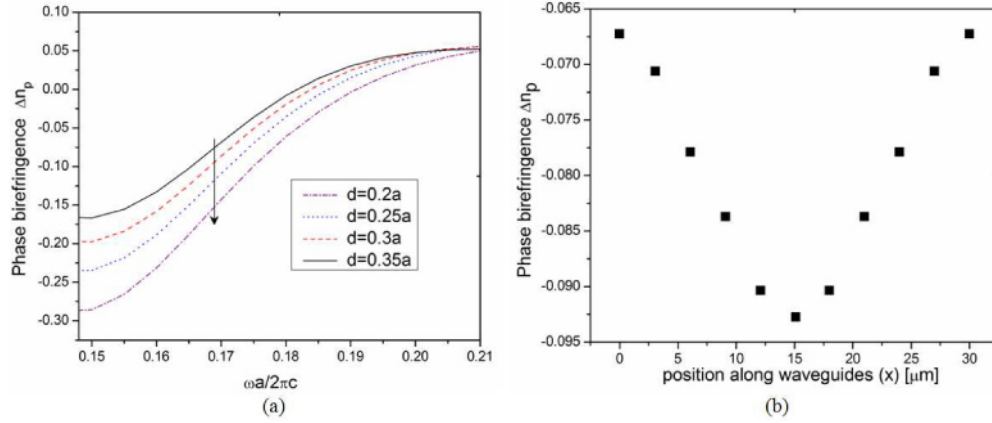


Figure 4-4 (a) Phase birefringence Δn_p as a function of signal frequency in the coupled waveguides with varying separations. The arrow shows that at a frequency $\omega_s a/2\pi c=0.17$, the absolute value of Δn_p increases as the waveguide separation d decreases. (b) Phase birefringence Δn_p as a function of position along the waveguides. The initial separation is $d=0.35a=92.2$ nm. The attractive force is induced by CW pump light at frequency $\omega_p a/2\pi c=a/\lambda_p=0.165$ and power $P=20$ mW. The difference between the maximum and the minimum of Δn_p is 0.026.

4.3.1 Tunable Relative Phase-shift

A potential application of the system is to dynamically adjust the relative phase shift between TE and TM modes. The total phase shift between TE and TM modes is calculated as:

$$\Delta\phi = \int_0^L |k^{TE}(x) - k^{TM}(x)| dx = \frac{\omega}{c} \int_0^L |n_p^{TE} - n_p^{TM}| dx = \frac{2\pi}{\lambda_s} \int_0^L |\Delta n_p| dx \quad (4-2)$$

The phase shift in two parallel waveguides with a separation of 92.2 nm is estimated to be $2\pi \times 30 \mu\text{m} \times 0.067 / 1.55 \mu\text{m} \approx 2.59\pi$, equal to 0.59π modulo 2π . When we input CW pump light with a power of 20 mW, the waveguides deform and the phase shift is changed to 3.11π , or 1.11π modulo 2π . The tuning range is about 0.5π . If we reduce the waveguide length to 23.05 μm , the total relative phase shift of a linear signal is 2π at the output of the un-deformed device. We plot the relative phase difference (phase difference modulo 2π) as a function of input pump power, as shown by black squares in Figure 4-5. By increasing the pump power, the phase difference can be adjusted from 0.12π to 0.51π . Taking the pump power to be about 67 mW, we obtain a total relative phase shift of 0.5π . Thus, an incoming signal of linear light whose E -field is at 0.25π to the y (or z) axes will emerge from the device circularly polarized.

We note that a variety of approaches exist for polarization control in fiber [26] and on-chip microphotonic systems [27-30]. In microphotonic systems in particular, polarization rotators have been designed based on tapered waveguide cores [27] and asymmetric waveguides [28-30]. Reference [31] presented a linear-to-circular polarization converter based on a high-Q dielectric microring resonator. In contrast to these approaches, we take advantage of mechanical motion to yield a widely tunable phase shift that is also broadband (non-resonant) in response. For a device with fixed length, the phase birefringence and relative phase shift can be dynamically adjusted by varying pump light power. Unlike other polarization control schemes using semiconductor optical amplifiers [32, 33] or electrooptic materials, our approach is fully compatible with SOI materials systems.

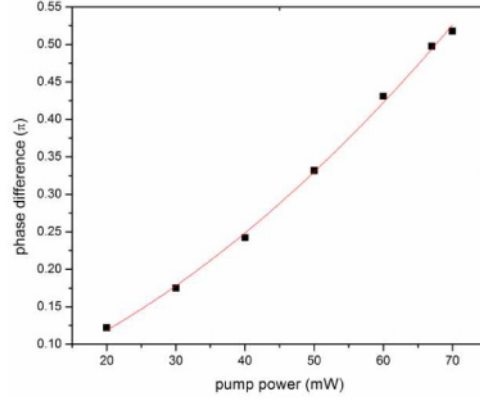


Figure 4-5 Tuning the relative phase shift by increasing CW pump power from 20 mW to 70 mW (black squares). The waveguide length is 23.05 μm . The red line is a 2nd –order polynomial fit of the phase shift. A power of approximately 67 mW yields a 0.5π phase difference.

4.3.2 Other tuning configurations

The dependence of phase birefringence on separation can be changed by altering the waveguide cross section. Figure 4-6 (a) depicts the birefringence versus signal frequency in two $a \times 2a$ waveguides. The arrow indicates that the value of Δn_p decreases with decreasing separation for frequencies from 0.11 to 0.16. The tuning trend is opposite from that in the system with two square waveguides. We can understand the trend by considering two extreme cases. For zero separation, light propagates in a square waveguide of cross section $2a \times 2a$, which has no birefringence due to spatial symmetry. For infinite separation, light propagates in a single rectangular waveguide asymmetric with respect to the y and z axes, which has large birefringence. Figure 4-6 (b) shows another waveguide structure with a cross section $a \times 0.5a$. The effective index of the TE mode is less than that of the TM mode. The absolute value of Δn_p increases with decreasing separation for frequencies from 0.20 to 0.25.

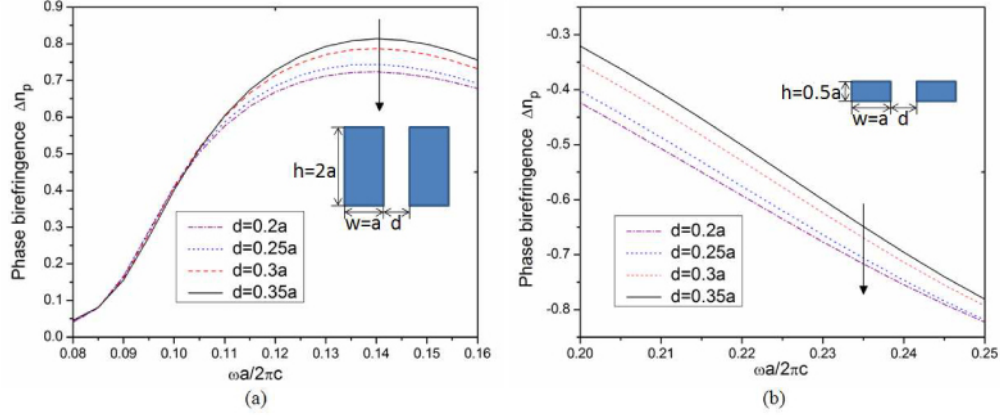


Figure 4-6 Phase birefringence Δn_p as a function of signal frequency in the two-waveguide system with varying separations. (a) The cross section of each waveguide is $a \times 2a$. The arrow shows that Δn_p decreases with decreasing separation. (b) The cross section of each waveguide is $a \times 0.5a$. The absolute value of Δn_p increases with decreasing separation.

4.4 Tunable Group Birefringence

The group birefringence also depends on waveguide separation and can be tuned by deforming the waveguides via an optical force. We plot the group birefringence Δn_g as a function of dimensionless signal frequency $\omega a / 2\pi c$, for different separations from $0.2a$ to $0.35a$ in Figure 4-7 (a). The birefringence increases with decreasing separation. The arrow indicates that the group birefringence Δn_g increases fastest at a frequency $\omega_s a / 2\pi c = 0.17$ ($a = 263.5$ nm, $\lambda_s = 1550$ nm). We consider deformation due to an attractive optical force for CW pump light at frequency $\omega_p a / 2\pi c = 0.165$ and power $P = 20$ mW, as above. Figure 4-7 (b) shows the group birefringence of signal light as a function of length along the waveguides for $L = 30$ μm . The initial value 1.09 corresponds to the birefringence of the undeformed waveguides. The peak of the birefringence is approximately 1.22 at the waveguide center. The difference between the maximum and the minimum of Δn_g is 0.13.

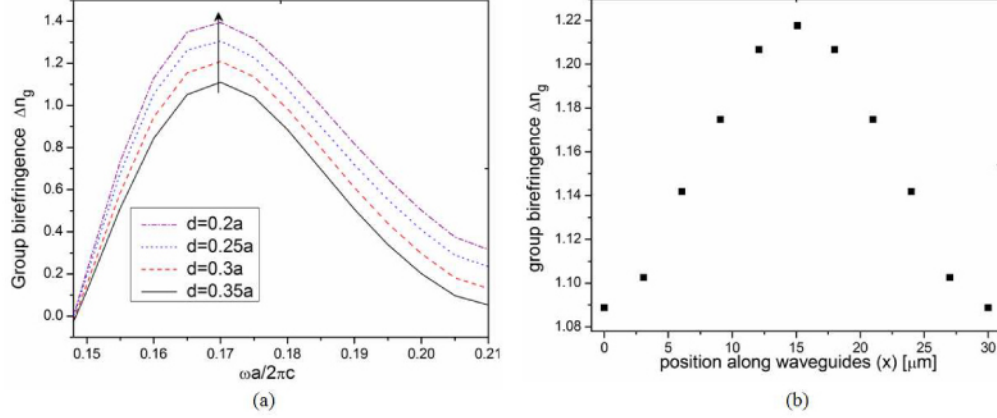


Figure 4-7 (a) Group birefringence Δn_g as a function of signal frequency, in the coupled waveguides with varying separations. The arrow shows that as the waveguide separation d increases, the group birefringence Δn_g increases fastest at a frequency $\omega_s a / 2\pi c = 0.17$. (b) Group birefringence Δn_g as a function of position along the waveguides. The waveguides are deformed by an attractive force induced by a CW pump at frequency $\omega_p a / 2\pi c = a / \lambda_p = 0.165$, with a power $P = 20$ mW. The difference between the maximum and the minimum of Δn_g is 0.13.

The system can be used to tune the polarization-selective delay between TE and TM pulses. The delay is tuned by adjusting the pump power. The differential time delay between TE and TM pulses is calculated as:

$$\Delta t = \int_0^L \left(\frac{1}{v_g^{TE}} - \frac{1}{v_g^{TM}} \right) dx = \frac{1}{c} \int_0^L (n_g^{TE} - n_g^{TM}) dx = \frac{1}{c} \int_0^L \Delta n_g dx \quad (4-3)$$

For two parallel waveguides without deformation, the differential time delay is $1.09 \times 30 \mu\text{m} / 3 \times 10^8 = 109$ fs. By inputting CW pump light at a power of 20 mW, we increase the differential time delay to 115 fs.

If we consider applications where the pulse width is comparable to the tunable delay range, we can take the pulse width $T = 6$ fs. We can estimate the dispersion length as $L_d = T^2 / \beta_2$ [34],

where the dispersion coefficient $\beta_2 = d^2k / d\omega^2$ is $2.2 \times 10^{-25} \text{ s}^2/\text{m}$. The parameter L_D is around 164 micrometers, much larger than the waveguide length. We can thus assume that minimal distortion occurs due to propagation through the 30- μm long suspended section.

The tuning range can be increased by increasing the pump power. The tuning range can also be increased by fabricating longer suspended sections, which deform more easily for fixed power, or by fabricating multiple suspended sections in series.

Note that this analysis also applies to vibrating waveguides actuated by pulsed pump light. The dynamic system experiences similar displacement as the static system for much smaller pump powers. While the waveguide beam vibrates in a period of a few hundred nanoseconds, the transmission time of a signal pulse through the 30 μm waveguide is on the order of a femtosecond. The beam can thus be treated as static in the calculation of time delay, provided that the signal pulse is much shorter than the vibration period in time.

4.5 Thermal Effects

In addition to optical forces, thermal effects may also contribute to waveguide deformation. The waveguides absorb propagating light, experience thermal expansion, and are mechanically deformed. We performed FEM (finite element method) simulations to calculate the displacement caused by the photo-thermo-mechanical effect using COMSOL Multiphysics software. We considered two silicon waveguides with identical cross section $263.5 \times 263.5 \text{ nm}^2$ and separation 92.2 nm sitting on top of a silicon dioxide substrate, as shown in Figure 4-1 (a). The free-section length of the beams is 30 μm . We used a similar simulation method to that introduced in the

supplementary methods of Reference [10]. The beams are assumed to be thermally isolated, except where they contact the substrate. The boundaries of the silicon dioxide substrate are assumed to be of constant temperature 300 K. The absorption constant of silicon α is estimated to be 0.0079 cm^{-1} at $1.597 \text{ }\mu\text{m}$ pump wavelength by using the equation $\alpha=4\pi k/\lambda$ and the value of the extinction coefficient k . With 20mW incident optical power, the absorbed power is approximately $0.474 \text{ }\mu\text{W}$. After using the RF module to solve for the pump mode profile, we define a resistive heating power of $0.474 \text{ }\mu\text{W}$ as the heating source in the thermal module. We obtain a calculated temperature profile that shows a peak temperature $T-300=0.097 \text{ K}$ near the center of the beams. The thermal simulation is followed by a mechanical simulation to solve for the mechanical stress that results from the thermal load. We are primarily concerned with the mechanical displacement in the z direction, which may introduce inaccuracy into the birefringence tuning. A peak z -displacement of 0.392 pm is reached at the waveguide center. The peak displacement in the y -direction was $<5 \text{ pm}$. The thermally induced displacement is thus negligible compared with the displacement due to the optical force of 9 nm .

Considering that the thermo-optical coefficient $1.86 \times 10^{-4} \text{ K}^{-1}$ for silicon, we estimate that the refractive index change due to our calculated temperature increase is on the order of 10^{-5} , which is far smaller than the index change caused by optomechanical deformation.

We conclude that thermal effects can be neglected in the system studied here, in agreement with the conclusions found in Reference [10] for a similar experimental system.

4.6 Summary

In this work, we present an optomechanically-controlled system which resembles a suspended one-slot waveguide with adjustable slot width depending on the optical force. The change in slot width corresponds to a change in the symmetry of the cross-section of the device, and therefore tunes both phase and group birefringence. We optimize the polarization and frequency of continuous pump light to obtain a considerable force at low operating power. The deformed 30 μm waveguide shows a maximum displacement of about 9 nm at the center for a power of 20 mW. Correspondingly, the phase (group) birefringence at the waveguide center is different from that at the clamped ends by 0.026 (0.13), which is larger than previous records. When used to tune the relative phase of two orthogonally polarized light signals, the device has a tuning range of around $\pi/2$. If the orthogonally polarized components have identical amplitudes, it is possible to rotate the polarization state from linear to circular in a distance of 30 μm . We show further that the dependence of phase birefringence on separation can be changed by altering the waveguide cross section. When used as a polarization-dependent tunable delay element, the two-waveguide system has a tuning range of 6fs. We note that the birefringence tuning trends studied here apply not only to a two-beam system deformed by an optical force, but also by other actuation methods, including static electrostatic forces used in micro-electro-mechanical systems (MEMS).

In the future, the potential to tune birefringence via an optical force may be applied to design novel microring resonator systems. Waveguide-coupled microrings exhibit a strong (static) birefringence, which can be used to realize polarization converters and polarization-sensitive delay devices [35-37]. Recent experiments have shown that the separation between vertically-

stacked microrings can be adjusted via optical forces [13]. This capability may in the future be exploited to design highly-tunable birefringent devices along similar lines as studied here.

4.7 Chapter References

- [1]. M. L. Povinelli, M. Loncar, M. Ibanescu, E. J. Smythe, S. G. Johnson, F. Capasso, and J. D. Joannopoulos, "Evanescent-wave bonding between optical waveguides," *Opt. Lett.* **30**, 3042-3044 (2005).
- [2]. M. L. Povinelli, M. Ibanescu, S. G. Johnson, and J. D. Joannopoulos, "Slow-light enhancement of radiation pressure in an omnidirectional-reflector waveguide," *Applied Physics Letters* **85**, 1466-1468 (2004).
- [3]. F. Riboli, A. Recati, M. Antezza, and I. Carusotto, "Radiation induced force between two planar waveguides," *The European Physical Journal D - Atomic, Molecular, Optical and Plasma Physics* **46**, 157-164 (2008).
- [4]. M. L. Povinelli, "Microphotonics - Under pressure," *Nat. Photonics* **1**, 370-371 (2007).
- [5]. M. L. Povinelli, S. G. Johnson, M. Loncar, M. Ibanescu, E. Smythe, F. Capasso, and J. D. Joannopoulos, "High-Q enhancement of attractive and repulsive optical forces between coupled whispering-gallery- mode resonators," *Opt. Express* **13**, 8286-8295 (2005).
- [6]. J. Ng, C. T. Chan, P. Sheng, and Z. Lin, "Strong optical force induced by morphology-dependent resonances," *Opt. Lett.* **30**, 1956-1958 (2005).
- [7]. P. T. Rakich, M. A. Popovic, M. Soljacic, and E. P. Ippen, "Trapping, corralling and spectral bonding of optical resonances through optically induced potentials," *Nat Photon* **1**, 658-665 (2007).
- [8]. H. Taniyama, M. Notomi, E. Kuramochi, T. Yamamoto, Y. Yoshikawa, Y. Torii, and T. Kuga, "Strong radiation force induced in two-dimensional photonic crystal slab cavities," *Physical Review B* **78**, 165129 (2008).
- [9]. M. Eichenfield, C. P. Michael, R. Perahia, and O. Painter, "Actuation of micro-optomechanical systems via cavity-enhanced optical dipole forces," *Nat Photon* **1**, 416-422 (2007).
- [10]. M. Li, W. H. P. Pernice, C. Xiong, T. Baehr-Jones, M. Hochberg, and H. X. Tang, "Harnessing optical forces in integrated photonic circuits," *Nature* **456**, 480-484 (2008).

- [11]. W. H. P. Pernice, M. Li, and H. X. Tang, "Theoretical investigation of the transverse optical force between a silicon nanowire waveguide and a substrate," *Opt. Express* **17**, 1806-1816 (2009).
- [12]. M. Li, W. H. P. Pernice, and H. X. Tang, "Tunable bipolar optical interactions between guided lightwaves," *Nat Photon* **3**, 464-468 (2009).
- [13]. G. S. Wiederhecker, L. Chen, A. Gondarenko, and M. Lipson, "Controlling photonic structures using optical forces," *Nature* **462**, 633-636 (2009).
- [14]. J. Chan, M. Eichenfield, R. Camacho, and O. Painter, "Optical and mechanical design of a "zipper" photonic crystal optomechanical cavity," *Opt. Express* **17**, 3802-3817 (2009).
- [15]. M. Eichenfield, R. Camacho, J. Chan, K. J. Vahala, and O. Painter, "A picogram- and nanometre-scale photonic-crystal optomechanical cavity," *Nature* **459**, 550-555 (2009).
- [16]. S. H. Yang, M. L. Cooper, P. R. Bandaru, and S. Mookherjea, "Giant birefringence in multi-slotted silicon nanophotonic waveguides," *Optics Express* **16**, 8306-8316 (2008).
- [17]. C. Kerbage, P. Steinvurzel, P. Reyes, P. S. Westbrook, R. S. Windeler, A. Hale, and B. J. Eggleton, "Highly tunable birefringent microstructured optical fiber," *Optics Letters* **27**, 842-844 (2002).
- [18]. C. Kerbage, and B. J. Eggleton, "Numerical analysis and experimental design of tunable birefringence in microstructured optical fiber," *Optics Express* **10**, 246-255 (2002).
- [19]. T. Woliński, A. Czapla, S. Ertman, M. Tefelska, A. Domański, E. Nowinowski-Kruszelnicki, and R. Dąbrowski, "Tunable highly birefringent solid-core photonic liquid crystal fibers," *Optical and Quantum Electronics* **39**, 1021-1032 (2007).
- [20]. K. K. Tsia, S. Fathpour, and B. Jalali, "Electrical tuning of birefringence in silicon waveguides," *Applied Physics Letters* **92**, 061109-061103 (2008).
- [21]. M. Kumar, T. Sakaguchi, and F. Koyama, "Wide tunability and ultralarge birefringence with 3D hollow waveguide Bragg reflector," *Opt. Lett.* **34**, 1252-1254 (2009).
- [22]. V. R. Almeida, Q. Xu, C. A. Barrios, and M. Lipson, "Guiding and confining light in void nanostructure," *Opt. Lett.* **29**, 1209-1211 (2004).
- [23]. Q. Xu, V. R. Almeida, R. R. Panepucci, and M. Lipson, "Experimental demonstration of guiding and confining light in nanometer-size low-refractive-index material," *Opt. Lett.* **29**, 1626-1628 (2004).
- [24]. J. D. Jackson, *Classical Electrodynamics* (Wiley, New York, 1999).

- [25]. V. A. Parsegian, *Van der Waals forces : a handbook for biologists, chemists, engineers, and physicists* (Cambridge University Press, New York, 2006).
- [26]. A. H. Rose, N. Feat, and S. M. Etzel, "Wavelength and Temperature Performance of Polarization-Transforming Fiber," *Appl. Opt.* **42**, 6897-6904 (2003).
- [27]. M. R. Watts, and H. A. Haus, "Integrated mode-evolution-based polarization rotators," *Opt. Lett.* **30**, 138-140 (2005).
- [28]. Y. Shani, R. Alferness, T. Koch, U. Koren, M. Oron, B. I. Miller, and M. G. Young, "Polarization rotation in asymmetric periodic loaded rib waveguides," *Applied Physics Letters* **59**, 1278-1280 (1991).
- [29]. J. J. G. M. Van der Tol, F. Hakimzadeh, J. W. Pedersen, D. Li, and H. Van Brug, "A new short and low-loss passive polarization converter on InP," *Photonics Technology Letters, IEEE* **7**, 32-34 (1995).
- [30]. K. Bayat, S. K. Chaudhuri, and S. Safavi-Naeini, "Ultra-compact photonic crystal based polarization rotator," *Opt. Express* **17**, 7145-7158 (2009).
- [31]. C. Fietz, and G. Shvets, "Nonlinear polarization conversion using microring resonators," *Opt. Lett.* **32**, 1683-1685 (2007).
- [32]. R. J. Manning, A. Antonopoulos, R. Le Roux, and A. E. Kelly, "Experimental measurement of nonlinear polarisation rotation in semiconductor optical amplifiers," *Electronics Letters* **37**, 229-231 (2001).
- [33]. H. Soto, D. Erasme, and G. Guekos, "Cross-polarization modulation in semiconductor optical amplifiers," *Photonics Technology Letters, IEEE* **11**, 970-972 (1999).
- [34]. R. W. Boyd, *Nonlinear optics* (Academic Press, Amsterdam ; Boston, 2008).
- [35]. C. Fietz, and G. Shvets, "Simultaneous fast and slow light in microring resonators," *Opt. Lett.* **32**, 3480-3482 (2007).
- [36]. F. Morichetti, A. Melloni, A. Breda, A. Canciamilla, C. Ferrari, and M. Martinelli, "A reconfigurable architecture for continuously variable optical slow-wave delay lines," *Opt. Express* **15**, 17273-17282 (2007).
- [37]. F. Morichetti, C. Ferrari, A. Melloni, and M. Martinelli, "Polarization-Selective Tunable Delay in Coupled-Resonator Optical Delay-Lines," in *Integrated Photonics and Nanophotonics Research and Applications* (Optical Society of America, 2008), p. IWG1.

Chapter 5: Trapping in a Slot-Suzuki-phase Lattice

5.1 Background

Optical trapping of objects with micro- and nano-scale dimensions has opened up novel opportunities in areas from physics to biology [1-4]. While optical tweezers make use of free-space beams, recent research has explored the use of integrated optical devices for particle trapping [5]. The strong evanescent fields in such micron-sized structures enable trapping on the sub-wavelength scale. Designs based on plasmonics [6], dielectric waveguides [7], and cavities [8-11] have been proposed and demonstrated for trapping of single particles. In a recent work [12], we have proposed a method to assemble 2D arrays of particles with particular, designable patterns. This process, which we call light assisted, templated self assembly, relies on the structured light fields above a photonic crystal slab to create an array of particle trapping locations. By changing the wavelength or polarization incident on the photonic crystal, the fields, and hence the trapping locations, can be reconfigured. This process can be used either to create tunable photonic filters or to fabricate ordered patterns of nanoparticles. In our previous work, as a proof of concept, we considered a simple, square-lattice design for the photonic crystal. The estimated power for trapping was 1mW/unit cell, limiting the feasibility of the method. However, it is known that in photonic-crystal microcavity structures, the introduction of a slot into the cavity can provide high field confinement, reducing the power required for single-particle trapping [10, 11]. In this work, we propose a novel 2D photonic crystal that exploits slot confinement to reduce the optical power for trapping of particle arrays by two orders of magnitude.

Below, we present our novel photonic crystal structure, designed for low-power optical trapping of particle arrays. The 2D periodic structure is created by introducing a rectangular slot at the center of each unit cell of the Suzuki-phase lattice [13]. When the incident light wavelength is tuned to excite a guided resonance mode (GRM), the optical field is confined and enhanced within the slot. Meanwhile, the quality (Q) factor is increased by orders of magnitude. Our numerical simulations show that for fixed incident power, the optical force on a particle above the lattice is also enhanced by orders of magnitude, significantly reducing the power required for stable trapping. For an ideal device, stable trapping of 25-nm radius particles requires a power as low as 27 μW per unit cell, around 40 times smaller than for the simple square-lattice structures studied in our previous work [12]. We predict that a particle with dimensions smaller than the slot will be pulled inside and stably trapped, with a required power of only 3 μW per unit cell, 300 times smaller than in our previous work. The novel lattice structure and corresponding low power requirements also open up an opportunity for experimental implementation in active structures. Using a 2D photonic crystal surface-emitting laser based on the slot Suzuki-phase design, we expect that self-adaptive trapping of 2D particle arrays may be demonstrated.

5.2 Structure Design

The Slot-Suzuki-phase photonic crystal lattice we propose is based on the conventional Suzuki-phase (SP) lattice shown in Figure 5-1 (a). The Suzuki-phase lattice is obtained by starting with a triangular lattice of holes and removing selected holes to generate a rectangular lattice of $H1$ cavities [13, 14]. The Suzuki-phase lattice has different periodicities in the x and y

directions, equal to $s_x = 2a$ and $s_y = \sqrt{3}a$ respectively, where a is the lattice constant of the reference triangular lattice.

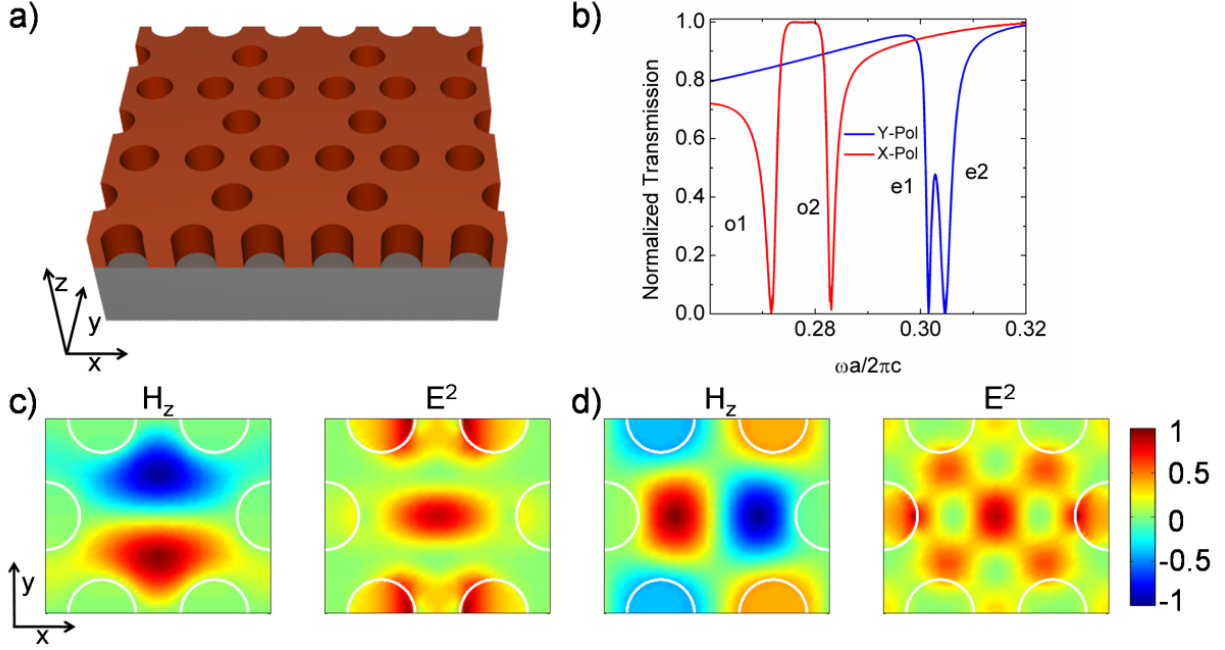


Figure 5-1 (a) Diagram of the Suzuki-Phase photonic crystal lattice. (b) Normalized transmission spectra calculated by the transfer-matrix method. Red line for x -polarization, blue for y -polarization. (c) H_z -field profile (left) and E^2 (right) of o1 resonance. d) H_z -field profile (left) and E^2 (right) of e2 resonance.

Figure 5-1 (b) illustrates the normalized transmission spectrum for vertically incident light, calculated by the Transfer Matrix Method (TMM) [15]. We assume a high-refractive index Suzuki-phase lattice with relative dielectric constant $\epsilon = 11.9$, hole radius $r/a = 0.3$ and slab thickness $t/a = 0.5$ resting on an oxide substrate ($\epsilon = 2.1$), and immersed in a fluid with dielectric constant $\epsilon_f = 1.7$. Due to the periodic modulation of the photonic crystal (PhC) slab, incident light can couple to the GRM's. Guided resonance modes are strongly confined to the slab and

appear in the transmission spectrum as Fano line shapes superimposed on a Fabry-Perot background [16]. We focus in particular on Γ -point modes that are not symmetry-forbidden [17, 18]. Figure 5-1 (b) shows the four GRM's we are interested in. We label the four modes by $o1$, $o2$, $e1$, and $e2$. Figures 5-1 (c) and (d) show the magnetic field component H_z and electric field intensity E^2 of the $o1$ and $e2$ resonance, respectively, in the $z = 0$ plane. These two, dipole-like modes are characteristic of the set. Modes were calculated by the three-dimensional (3D) finite difference time-domain (FDTD) method [19] and normalized to the maximum value in the $z = 0$ plane. The $o1$ mode exhibits odd vector symmetry [20] with respect to the $x = 0$ mirror plane (H_z is even) and couples to a plane wave with electric field polarized along the x direction; the $e1$ mode exhibits even vector symmetry with respect to the $x = 0$ mirror plane (H_z is odd) and couples to a plane wave with electric field polarized in the y direction, as has been shown experimentally [21].

We calculate Q factor for the four modes in Figure 5-1 (b) using 3D FDTD calculations. For a real photonic device with finite lateral size, the total Q factor depends on both vertical and lateral losses. However, for large enough structures and laser excitation spots, it is reasonable to consider only the effect of vertical loss on the Q factor [22, 23]. We model the PhC structure as infinitely periodic in the lateral direction by imposing periodic boundary conditions along the x and y directions of the unit cell in the FDTD simulation. The corresponding Q factors of the $o1$ and $e2$ modes are 118 and 262, respectively. In order to trap a particle in the near field of the PhC, it is desirable to concentrate the optical power in a small surface area and to have a large Q factor [5], so as to enhance the trapping force for fixed input power. However, Figures 5-1 (c) and (d) show that the electric field intensity E^2 in the $z = 0$ plane of both the x -polarized and y -polarized dipole modes is relatively spread out across the unit cell. In order to

increase the Q factor and reduce the mode area, we propose a Slot-Suzuki-phase (SSP) hybrid lattice, shown in Figure 5-2 (a). Rectangular slots with cross-sectional dimensions of $w_x \times w_y$ are positioned in the middle of each unit cell of the conventional SP lattice. The symbol w_x and w_y represent the slot length along the x and y axes, respectively. In the slot, the component of electric field normal to the slot boundary is enhanced due to the Maxwell continuity law [24, 25]. If the smaller dimension of the rectangular slot is along the y direction ($w_y < w_x$), the electric field of the y -polarized $e1$ and $e2$ modes will be enhanced. To obtain enhancement of the x -polarized $o1$ and $o2$ modes, the slot should be designed with $w_x < w_y$. In the following discussion, we focus on the case where $w_y < w_x$.

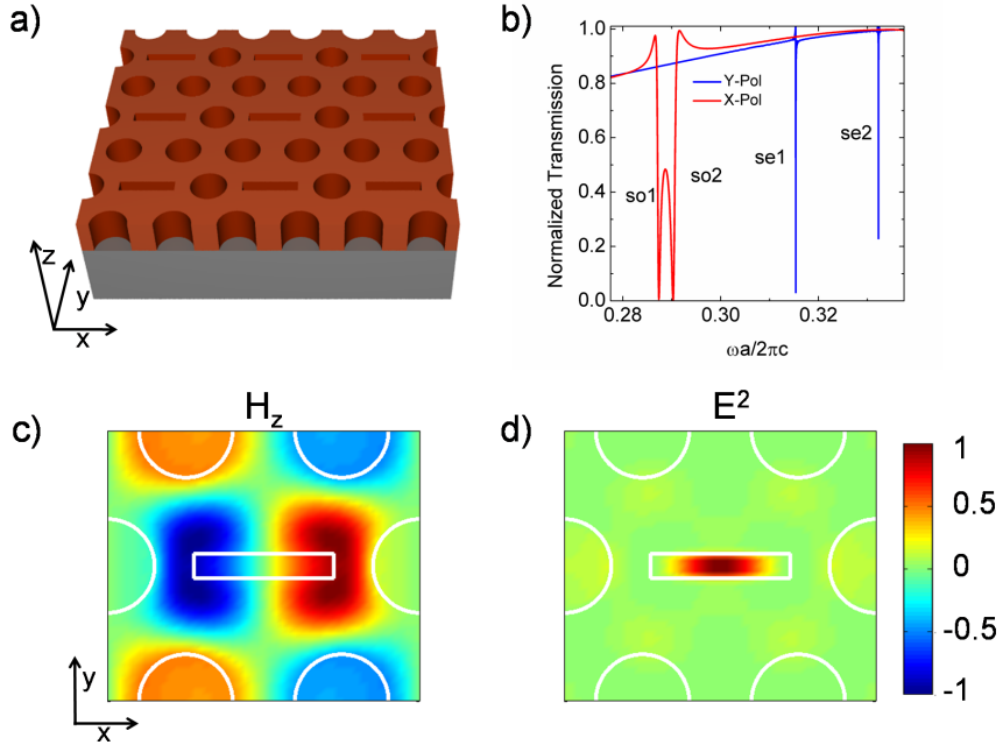


Figure 5-2 (a) Diagram of the Slot-Suzuki-phase hybrid lattice. (b) Normalized transmission spectra. Red line for x -polarization, blue for y -polarization. (c) H_z -field profile of $se2$ resonance. (d) E^2 field profile of $se2$ resonance.

In Figure 5-2 (b), we plot the transmission spectrum of the SSP lattice at normal incidence for slot dimensions $w_x/a = 0.9$ and $w_y/a = 0.16$. The other structural and material parameters are identical with the above-mentioned SP lattice. We label the four Fano transmission dips as *so1*, *so2*, *se1*, and *se2*. All four modes exhibit narrower lineshapes than those in the SP lattice (Figure 5-1 (b)). Note that the width of the frequency window is the same for Figure 5-1 (b) and Figure 5-2 (b). Thus, higher Q factors can be obtained which are inversely proportional to the resonance linewidths. We will focus our discussion of field localization on the *se2* mode. Figures 5-2 (c) and (d) plot H_z and E^2 for the *se2* mode in the $z = 0$ plane of the SSP lattice. The electric field of the *se2* mode is well confined around the center of the slot in the XY plane. In fact, the modal volume for the *se2* mode in one unit cell is $V_{eff} = 2.4 \times 10^{-2} (\lambda_R/n_f)^3$, where λ_R is the resonant wavelength and n_f is the refractive index of the fluid. The mode volume per unit cell is comparable to that in PhC microcavities containing slot features [25], indicating strong confinement of the field by the slot within each unit cell of the SSP lattice. The decay length of the field intensity, for which the value of falls to $1/e$ of the value at the slot center, are $0.28a$ in the x -direction, $0.09a$ in the y -direction, and $0.3a$ in the z -direction ($0.05a$ above the PhC slab).

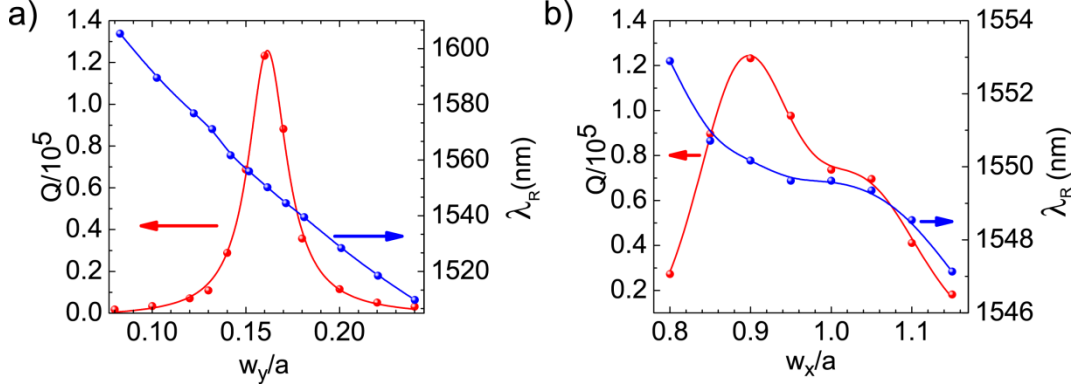


Figure 5-3 (a) Evolution of the Q and wavelength λ_R as a function of slot width w_y . b) Evolution of the Q and wavelength λ_R as a function of slot length w_x . Red color indicates Q; blue color indicates wavelength. Dots correspond to calculated values; lines represent a guide for the eye.

Adjusting the slot dimensions provides a flexible strategy for tuning the Q factor and resonant wavelength λ_R of the GRM's. Varying the slot width (w_y) can dramatically increase the Q factor of the mode. In Figure 5-3 (a), we plot the dependence of Q on w_y for fixed $w_x = 0.9a$ for the *se2* mode. In the limit where the slot vanishes, i.e., the conventional SP lattice with only circular holes, the Q factor for the *e2* mode is 262. By adding a narrow slot of $w_y = 0.08a$ in the center of each unit cell, the Q factor is increased to 1750. The Q factor is further enhanced by increasing w_y and reaches a peak value of around 123,000 at $w_y = 0.16a$. This Q value is comparable to values obtained in square PhC lattices for coupled GRM's [26]. If the slot width w_y continues to increase beyond $0.16a$, the Q factor decreases.

The slot width also affects the resonant wavelength λ_R . The blue line in Figure 5-3 (a) shows that λ_R linearly decreases from 1605 nm for $w_y = 0.08a$ to 1510 nm for $w_y = 0.24a$ with a slope of approximately -1.2. The graph is plotted assuming a fixed lattice constant a of 515 nm.

Changing the slot length (w_x) also affects the Q factor and resonant wavelength λ_R . We fix $w_y = 0.16a$ and adjust w_x . As indicated by Figure 5-3 (b), the Q factor decreases from 123,000 when w_x deviates from $0.9a$, but remains above 20,000 for w_x between $0.8a$ and $1.15a$. The blue line shows that the wavelength λ_R remains relatively stable with a shift of less than 6 nm in the same w_x range. This relatively low variation can be explained by the mode distribution shown in Figure 5-2 (d). The electric field is tightly confined in the slot with a decay length in the x direction of $0.28a$, which is less than half of the slot length ($w_x/2 = 0.45a$). Thus, the resonance profile is only lightly influenced by w_x decreasing from $1.15a$ to $0.8a$. The choice of w_x can be considered as an approach for fine-tuning of the dipole mode Q factor and wavelength.

5.3 Optical Forces

When SSP lattices with different slot dimensions are compared, the Q factor changes by orders of magnitude, while the mode profile remains similar. The component H_z has a dipole distribution and the electric field intensity is concentrated in the slot. The SSP lattice thus offers the flexibility to design a broad range of Q factors and, therefore, trapping forces. The main objective of this section is to predict the trapping capabilities of the SSP lattice with lattice constant $a = 515$ nm on a dielectric particle ($n_{poly} = 1.60$). The trapping forces exerted on the particle are computed by integrating the Maxwell stress tensor (MST) over a closed surface surrounding the particle. The forces are numerically calculated by 3D FDTD simulations. We take a rectangular solid with a surface several mesh points away from the nearest edge of the particle as the integration surface. Due to the high Q factor of the GRM, it is convenient to perform the force calculation in the time domain rather than the frequency domain. We excite the

mode using a dipole source inside the slab, record the instantaneous electromagnetic fields for several optical periods, and use them to calculate the time-dependent force. We then time-average the force and normalize it to the power P coupled to the $se2$ mode.

We calculate the optical force on a particle of radius varying from 25 nm to 100 nm. The particle is placed right above the center of the slot (at position $x = 0, y = 0$), with its bottom edge 45 nm above the top surface of the slab. Due to symmetry, the transverse force (F_{xy}) on the particle vanishes. Figure 5-4 (a) shows the vertical force F_z/P above the SSP lattice for slot dimensions $w_x = 0.9a = 464$ nm and w_y between $0.08a$ (41 nm) and $0.24a$ (124 nm). The force is negative, meaning that it is directed towards the slab. For all radii, the force magnitude increases to a peak value and then decreases with increasing slot width (w_y), following a similar trend as the Q factor. In the optimum case, a slot with $w_y = 0.16a = 82$ nm enhances the force by two orders of magnitude compared to a slot with $w_y = 0.08a = 41$ nm. The optical force increases with particle radius. For a particle of radius 25 nm, the maximum force magnitude reaches 46 pN for 1 mW power per unit cell. For a 100-nm-radius particle, the force increases to 46 pNmW^{-1} , an order of magnitude enhancement. In Figure 5-4 (b) we plot the dependence of force on particle radius for a particle which is at $(x = 0, y = 0)$ and has its bottom edge 45nm above the top surface of the slab. The force magnitude increases linearly with particle radius between 25 nm and 100 nm.

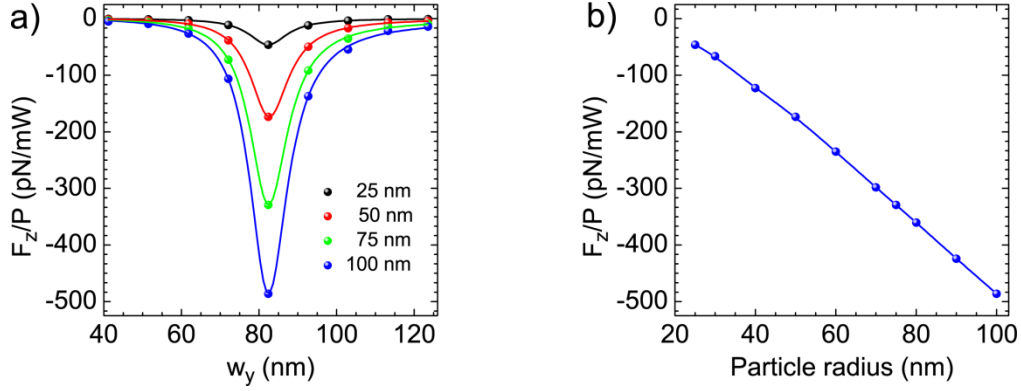


Figure 5-4 (a) Optical force F_z as a function of slot width w_y for four different particle radii. The slot length w_x is fixed to 464 nm. (b) Optical force F_z as a function of particle radius. Dots represent the calculated values. Lines represent a guide for the eye. In both (a) and (b), the particle is at $(x = 0, y = 0)$ and has its bottom edge 45 nm above the top surface of the slab.

To investigate the dependence of the force on particle position, we set the slot dimensions to $464 \text{ nm} \times 82 \text{ nm}$ ($0.9a \times 0.16a$), for which Q achieves its optimal value of 123,000. We consider a particle of radius 25 nm. The lower edge of the particle is 45 nm above the top surface of the slab (see Figure 5-5 (a)). We calculate the vertical force (F_z) and transverse force (F_{xy}) on the particle for each position in the XY plane. The results are shown in Figures 5-5 (b) and (c). The maximum magnitude of F_z is approximately 46 pNmW^{-1} , which is achieved when the particle is above the center ($x = 0, y = 0$). For all positions in the XY plane, the vertical force is directed towards the slab. The magnitude of the in-plane force F_{xy} is shown by the colormap in Figure 5-5 (c), and the force direction is indicated by blue arrows. At the center ($x = 0, y = 0$), the in-plane force vanishes. The strongest in-plane forces point toward the center. The maximum in-plane force for the particle is 14 pNmW^{-1} and is weaker than the maximum vertical force of 46 pNmW^{-1} . The ability to stably trap particles is thus limited by the in-plane values. Given the spatial map of the in-plane forces F_{xy} in Figure 5-5 (c), we can calculate a potential map in the

XY plane. We calculate the potential depth ΔU by integrating the in-plane force from a reference position to each point in the XY plane. Here, the reference position is taken to be $(-s_x/2, s_y/2)$. The choice of the reference position does not affect the relative potential depth. The potential map is shown in Figure 5-5 (d). The depth of the trapping potential is larger than $377 K_B T$ for an incident power of 1 mW per unit cell, where $K_B T$ is the thermal energy at temperature 300 K. A figure of merit in the context of optical trapping is the stability factor $S = \Delta U / K_B T$, which reaches 377 mW^{-1} per unit cell in our device. In order to achieve a stability factor equal to 10, generally considered sufficient to achieve stable trapping despite the presence of Brownian motion [27], the power needed in the SSP lattice is $27 \text{ } \mu\text{W}$ per unit cell. The power required to realize stable trapping in the SSP lattice is reduced by about 40 times compared to the power requirement in the square lattice proposed in our previous work [12]. At the equilibrium point, the trap stiffness is defined as $-\partial F_{xy} / \partial x$ along the x axis and $-\partial F_{xy} / \partial y$ along the y axis. From Figure 5-5 (c), we estimate trap stiffnesses of 0.12 and $0.28 \text{ pNnm}^{-1} \text{ mW}^{-1}$ for the 25 nm particle along the x and y axes, respectively, corresponding to a radial trap stiffness of $0.08 \text{ pNnm}^{-1} \text{ mW}^{-1}$ in the XY plane. Greater trap stiffness results in lower uncertainty in the trapping position. The stability factor and the radial trap stiffness we obtained exceed the values reported for dielectric trapping structures in previous works [5].

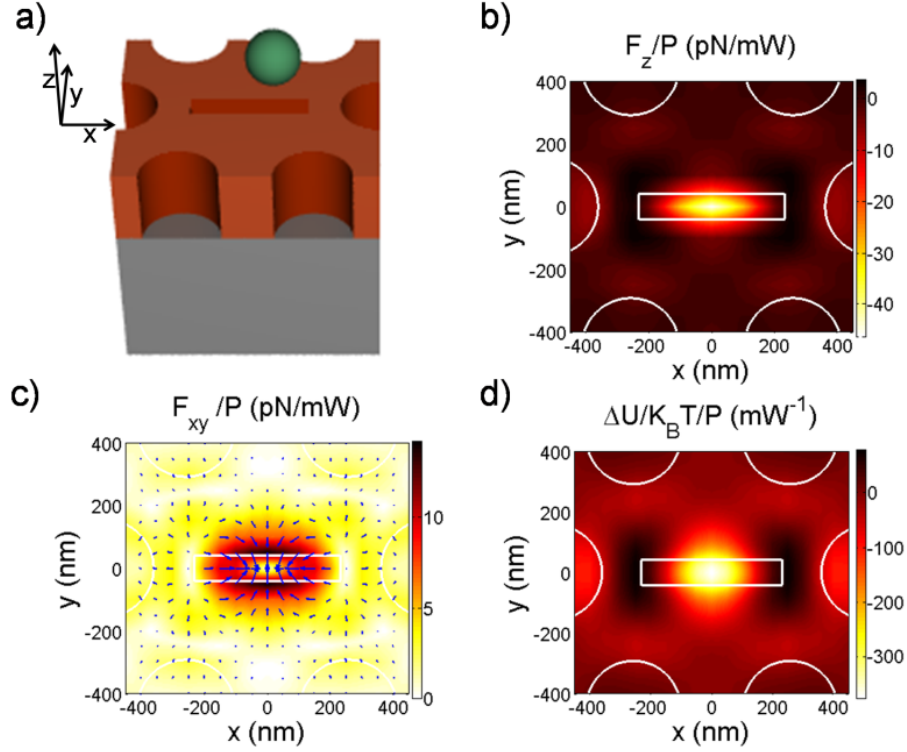


Figure 5-5 (a) Diagram of the Slot Suzuki-phase (SSP) lattice with a particle above. (b) Vertical force F_z as a function of particle position in the XY plane. (c) In-plane force F_{xy} as a function of position in the XY plane. The force magnitude is indicated by the colormap, and the force direction is shown by the blue arrows. (d) Potential map in the XY plane. To obtain the results shown in (b), (c), and (d), we assume that the particle has a radius of 25 nm and is placed such that its bottom edge is 45 nm above the top surface of the slab.

For particle diameters less than the slot width w_y , particles can be trapped inside the slot. The particle is physically confined by the slot in the y direction. We calculate the force as a function of position in the XZ plane for $y = 0$. Results are shown in Figure 5-6 (a). The force F_y , which is normal to the XZ plane, vanishes due to symmetry, and thus, we only plot the in-plane force F_{xz} . The forces point to the center of the slot at $(x = 0, z = 0)$ and have a maximum magnitude of 153 pNmW^{-1} . The corresponding potential map shown in Figure 5-6 (b) indicates that a strong trapping potential depth of more than 3500 $K_B T$ per milliwatt per unit cell is achieved within the

slot. For a particle within the slot, a power as low as 3 μW per unit cell is required for stable optical trapping. The radial trapping stiffness in the XZ plane is $-0.34 \text{ pNnm}^{-1}\text{mW}^{-1}$. Within the slot, the stability and trapping stiffness are higher than outside the slot and comparable to reported values for particle trapping in other slot structures [10, 11].

The presence of a particle in the slot can affect the resonance wavelength. Our simulations show that when every unit cell of the structure contains one particle of radius 25 nm in the center of the slot, the resonance wavelength is shifted by 0.3 nm. Nevertheless, in a real experiment, the particles are likely to be trapped one by one, with the number increasing gradually over time. In this case, any given particle will create a negligible perturbation on the mode. As larger numbers of particles are trapped, a gradual shift of the resonance wavelength will take place, requiring a slow adjustment of the excitation laser ($\Delta\lambda_R \leq 0.3 \text{ nm}$).

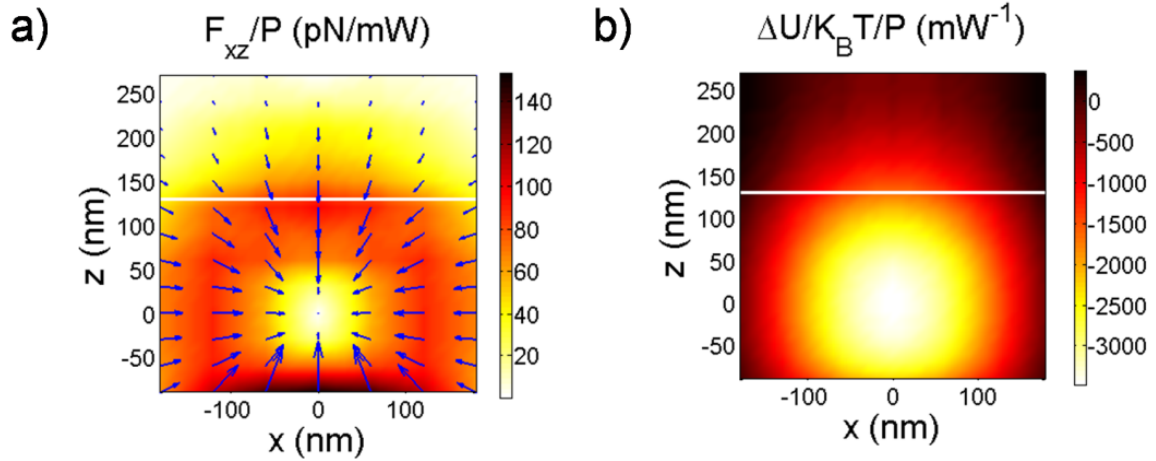


Figure 5-6 (a) In-plane optical force F_{xz} for a particle with radius of 25 nm. (b) Optical potential map for the particle.

5.4 Summary

We have proposed a new PhC lattice for optical trapping of two-dimensional arrays of nanoparticles. Our structure is created by using the 2D Suzuki-phase PhC lattice as a base and introducing a slot into each unit cell to localize the electromagnetic field. Optimizing the slot dimensions increases the Q factor of the resonance by orders of magnitude. Optical power values as low as 27 μW per unit cell are predicted for trapping of 25 nm radius beads, a reduction of power by about 40 times relative to our previous work. Once the particle is on the slot, optical power of 3 μW per unit cell is required for the stable optical trapping. Our Slot-Suzuki-Phase lattice is a promising candidate for carrying out light-assisted templated self assembly processes. The low power requirements for trapping suggest to use of active materials for this purpose. Slot photonic crystal microcavity lasers have been demonstrated with output optical power as high as 150 μW , and some evidence suggests possible optical trapping effects in such structures [28, 29]. The Slot-Suzuki-phase structure we propose here provides a way of effectively combining multiple slot PhC microcavities into a high-Q structure with extended area. Further improvement of the design can be achieved by band engineering techniques, as well as by combining the photonic crystal with a bottom Bragg reflector [30, 31]. In such a device, we expect that the laser may self adapt, adjusting its own lasing wavelength in response to the resonance shift induced by trapped particles.

5.5 Chapter References

[1]. A. Ashkin, "Acceleration and Trapping of Particles by Radiation Pressure," *Phys. Rev. Lett.* **24**, 156-159 (1970).

- [2]. K. C. Neuman, and S. M. Block, "Optical trapping," *Rev. Sci. Instrum.* **75**, 2787-2809 (2004).
- [3]. D. G. Grier, "A revolution in optical manipulation," *Nature* **424**, 810-816 (2003).
- [4]. J. Guck, R. Ananthakrishnan, H. Mahmood, T. J. Moon, C. C. Cunningham, and J. Kas, "The Optical Stretcher: A Novel Laser Tool to Micromanipulate Cells," *Biophysical Journal* **81**, 767-784 (2001).
- [5]. D. Erickson, X. Serey, Y.-F. Chen, and S. Mandal, "Nanomanipulation using near field photonics," *Lab on a Chip* **11**, 995-1009.
- [6]. M. L. Juan, M. Righini, and R. Quidant, "Plasmon nano-optical tweezers," *Nat Photon* **5**, 349-356 (2011).
- [7]. A. H. J. Yang, S. D. Moore, B. S. Schmidt, M. Klug, M. Lipson, and D. Erickson, "Optical manipulation of nanoparticles and biomolecules in sub-wavelength slot waveguides," *Nature* **457**, 71-75 (2009).
- [8]. M. Barth, and O. Benson, "Manipulation of dielectric particles using photonic crystal cavities," *Applied Physics Letters* **89**, 253114-253113 (2006).
- [9]. A. Rahmani, and P. C. Chaumet, "Optical trapping near a photonic crystal," *Opt. Express* **14**, 6353-6358 (2006).
- [10]. S. Lin, J. Hu, L. Kimerling, and K. Crozier, "Design of nanoslotted photonic crystal waveguide cavities for single nanoparticle trapping and detection," *Opt. Lett.* **34**, 3451-3453 (2009).
- [11]. X. Serey, S. Mandal, and D. Erickson, "Comparison of silicon photonic crystal resonator designs for optical trapping of nanomaterials," *Nanotechnology* **21**, 305202.
- [12]. C. A. Mejia, A. Dutt, and M. L. Povinelli, "Light-assisted templated self assembly using photonic crystal slabs," *Opt. Express* **19**, 11422-11428 (2011).
- [13]. A. R. Alija, L. J. Martinez, P. A. Postigo, J. Sanchez-Dehesa, M. Galli, A. Politi, M. Patrini, L. C. Andreani, C. Seassal, and P. Viktorovitch, "Theoretical and experimental study of

the Suzuki-phase photonic crystal lattice by angle-resolved photoluminescence spectroscopy," *Opt. Express* **15**, 704-713 (2007).

[14]. C. Monat, C. Seassal, X. Letartre, P. Regreny, M. Gendry, P. R. Romeo, P. Viktorovitch, M. L. V. d'Yerville, D. Cassagne, J. P. Albert, E. Jalaguier, S. Pocas, and B. Aspar, "Two-dimensional hexagonal-shaped microcavities formed in a two-dimensional photonic crystal on an InP membrane," *Journal of Applied Physics* **93**, 23-31 (2003).

[15]. M. Li, X. Hu, Z. Ye, K.-M. Ho, J. Cao, and M. Miyawaki, "Higher-order incidence transfer matrix method used in three-dimensional photonic crystal coupled-resonator array simulation," *Opt. Lett.* **31**, 3498-3500 (2006).

[16]. S. Fan, W. Suh, and J. D. Joannopoulos, "Temporal coupled-mode theory for the Fano resonance in optical resonators," *J. Opt. Soc. Am. A* **20**, 569-572 (2003).

[17]. T. Ochiai, and K. Sakoda, "Dispersion relation and optical transmittance of a hexagonal photonic crystal slab," *Physical Review B* **63**, 125107 (2001).

[18]. M. Galli, M. Agio, L. C. Andreani, M. Belotti, G. Guizzetti, F. Marabelli, M. Patrini, P. Bettotti, L. Dal Negro, Z. Gaburro, L. Pavesi, A. Lui, and P. Bellutti, "Spectroscopy of photonic bands in macroporous silicon photonic crystals," *Physical Review B* **65**, 113111 (2002).

[19]. A. Taflove, *Advances in computational electrodynamics : the finite-difference time-domain method* (Artech House, Boston, 1998).

[20]. J. D. Joannopoulos, R. D. Meade, and J. N. Winn, *Photonic crystals : molding the flow of light* (Princeton University Press, Princeton, N.J., 1995).

[21]. L. J. Martinez, A. R. Alija, P. A. Postigo, J. F. Galisteo-Lopez, M. Galli, L. C. Andreani, C. Seassal, and P. Viktorovitch, "Effect of implementation of a Bragg reflector in the photonic band structure of the Suzuki-phase photonic crystal lattice," *Opt. Express* **16**, 8509-8518 (2008).

[22]. X. Letartre, J. Mouette, J. L. Leclercq, P. R. Romeo, C. Seassal, and P. Viktorovitch, "Switching Devices With Spatial and Spectral Resolution Combining Photonic Crystal and MOEMS Structures," *J. Lightwave Technol.* **21**, 1691 (2003).

- [23]. L. J. Martinez, B. Alen, I. Prieto, J. F. Galisteo-Lopez, M. Galli, L. C. Andreani, C. Seassal, P. Viktorovitch, and P. A. Postigo, "Two-dimensional surface emitting photonic crystal laser with hybrid triangular-graphite structure," *Opt. Express* **17**, 15043-15051 (2009).
- [24]. V. Almeida, Q. Xu, C. Barrios, and M. Lipson, "Guiding and confining light in void nanostructure," *Optics Letters* **29**, 1209-1211 (2004).
- [25]. T. Yamamoto, M. Notomi, H. Taniyama, E. Kuramochi, Y. Yoshikawa, Y. Torii, and T. Kuga, "Design of a high-Q air-slot cavity based on a width-modulated line-defect in a photonic crystal slab," *Opt. Express* **16**, 13809-13817 (2008).
- [26]. M. El Beheiry, V. Liu, S. Fan, and O. Levi, "Sensitivity enhancement in photonic crystal slab biosensors," *Opt. Express* **18**, 22702-22714.
- [27]. A. Ashkin, J. M. Dziedzic, J. E. Bjorkholm, and S. Chu, "Observation of a single-beam gradient force optical trap for dielectric particles," *Opt. Lett.* **11**, 288-290 (1986).
- [28]. S. Kita, S. Hachuda, K. Nozaki, and T. Baba, "Nanoslot laser," *Applied Physics Letters* **97**, 161108-161103.
- [29]. S. Kita, S. Hachuda, S. Otsuka, T. Endo, Y. Imai, Y. Nishijima, H. Misawa, and T. Baba, "Super-sensitivity in label-free protein sensing using a nanoslot nanolaser," *Opt. Express* **19**, 17683-17690.
- [30]. B. B. Bakir, C. Seassal, X. Letartre, P. Viktorovitch, M. Zussy, L. Di Cioccio, and J. M. Fedeli, "Surface-emitting microlaser combining two-dimensional photonic crystal membrane and vertical Bragg mirror," *Applied Physics Letters* **88**, 081113-081113 (2006).
- [31]. L. Ferrier, P. Rojo-Romeo, E. Drouard, X. Letatre, and P. Viktorovitch, "Slow Bloch mode confinement in 2D photonic crystals for surface operating devices," *Opt. Express* **16**, 3136-3145 (2008).

Chapter 6: Characterization of Slot-graphite Photonic Crystal Lattice

6.1 Background

Photonic crystal structures have distinguished points with zero group velocity along the Brillouin boundary. The zero-group-velocity modes have been applied in many interesting fields, including laser emission [1-3], quantum optics [4], and sensing [5]. One interesting point with zero group velocity along the Brillouin boundary is Γ -point. The Γ -point modes are above the light line. The modes can be coupled or uncoupled to an external plane wave depending on the mode symmetry [6]. When light is normally incident upon the periodically patterned slab, it can excite Γ -point modes or as so called, guided resonance modes, which propagate in the plane of the slab while leaking partially to the surrounding air [7].

In the last Section, we have discussed utilizing Γ -point modes in a Slot-Suzuki-phase photonic crystal lattice for light-assisted, template assembly (LATS) of nanoparticles. We have pointed out that, for fixed input power, the optical forces can be enhanced by using a high-quality-factor and well-confined guided resonance modes. In other words, the assembly capability is dependent on optical quality factors. In this Section, we experimentally demonstrated the high-Q guided resonance modes in Slot-graphite lattices. The lattice is created by using regular graphite lattice [8] as the base and placing a rectangular slot into the center of each unit cell. Quality factors over 4×10^5 are predicted by theory. The Slot-graphite lattices have been fabricated on silicon-on-insulator platforms and optically characterized by transmission spectroscopy. We have observed the dependence of resonant wavelengths and Q factors on the

slot dimension. Note that by fine control of slot geometry, we can tune the Q factors by orders of magnitude. The modes have a strong field confinement within the slots, proposing potential applications in LATS.

6.2 Structure Design

The Slot-graphite photonic crystal lattice is created by using regular graphite lattice [8] as the base (See Figure 6-1 (a)). In the center of each unit cell, we place a rectangular slot oriented towards the middle point of two closest holes (see Figure 6-1 (b)). This novel structure uses the same Bravais lattice as the graphite lattice. Nevertheless the slot reduces the lattice symmetry from C_{6v} to C_{2v} [9], and the irreducible Brillouin zone changes from 1/12 of the first Brillouin zone (See Figure 6-2 (a) inset) to 1/4 (Figure 6-2 (b) inset). The irreducible Brillouin zone of graphite lattice is marked by Γ -M-K- Γ in Figure 6-2 (a) inset, while slot-graphite lattice is Γ -M-K-M1-K1- Γ in Figure 6-2 (b) inset.

Figure 6-2 (a) shows the 3D photonic band structure of a graphite lattice. The bands are calculated using guide mode expansion method [10]. We assume a lattice constant $a=800$ nm, a hole radius $r=0.157a$ and slab thickness of 250 nm laying on top of silica substrate. The device is immersed in a material of dielectric constant $\epsilon_b=1.77$.

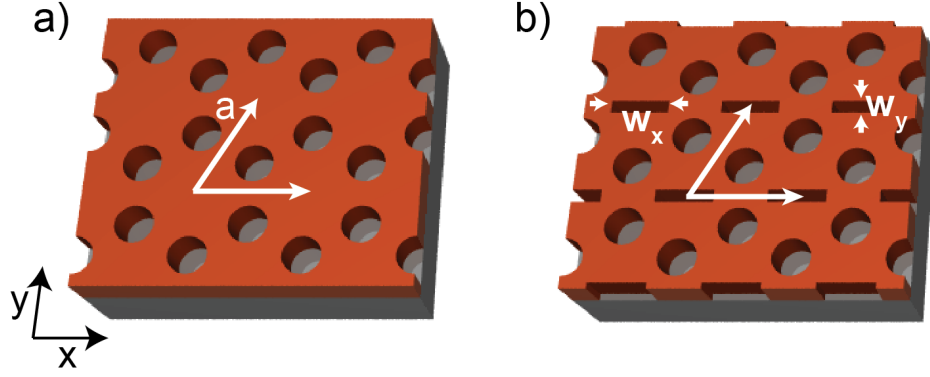


Figure 6-1 (a) Diagram of the graphite photonic crystal lattice. (b) Diagram of the Slot-graphite photonic crystal lattice. The arrows represent the primitive vectors of the Bravais lattice.

In Figure 6-2 (a), we show the band structure of the graphite lattice. At Γ -points as highlighted by dashed circles, the fourth and fifth bands are degenerate. The corresponding mode profiles are shown by Figure 6-2 (c). The H_z components of two degenerate modes have dipole-like distribution with different orientation. And we call them dipole modes. The electric field of the fourth (fifth) modes is x (y) polarized. Note that the bands are the same for the two Γ points in the M - Γ - K boundary and $M1$ - Γ - $K1$ boundary. The reason has been given in the last paragraph: in the graphite lattice, the M - Γ - K Brillouin zone is irreducible and contains all band information.

In Figure 6-2 (b), we show the band structure of our slot-graphite lattice. The slot dimension is $w_x=0.675a$ and $w_y=0.09a$. The other geometries are identical with the graphite lattice. The degeneration of the fourth and fifth band of the graphite lattice at the Γ -point is removed due to the breaking symmetry created by the slot. By adding slot in each unit cell, a sharp discontinuity of the dielectric constant is created. Due to the Maxwell continuity condition, the normal components of ϵE are conserved along the slot boundary [11, 12], so that the E_y field of the fifth band is enhanced within the slot as shown by the upper part of Figure 6-2 (d). The light

confinement within slot is not obvious for the fourth band, since this band is polarized along x direction. In the slot device, we are going to refer to the fifth band as slot mode whereas the fourth band as dipole mode. Note that the slot-mode band around the Γ -point is flat, which can be very important for specific application [13].

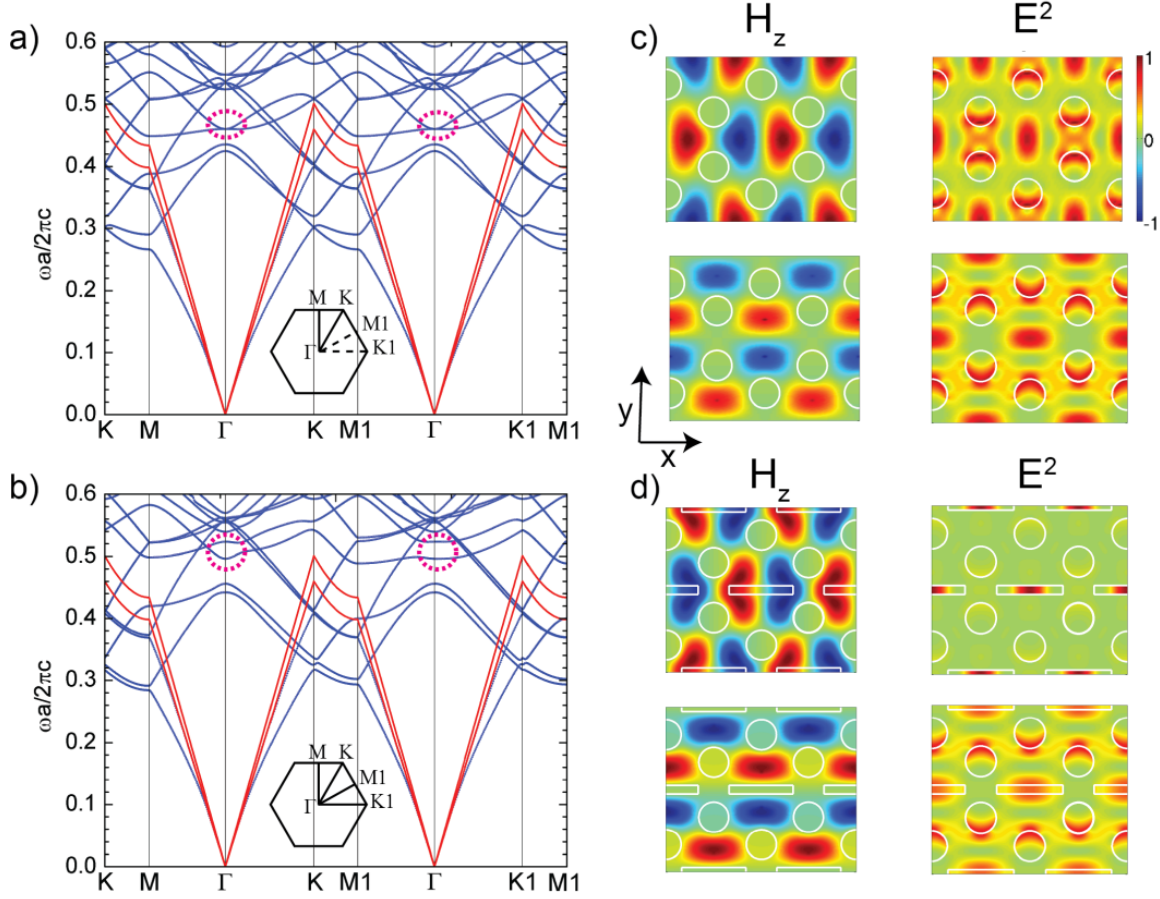


Figure 6-2 (a) Photonic band structure of the Graphite photonic crystal lattice. (b) Photonic band structure of the Slot-graphite photonic crystal lattice. The highlighted region represents the targeted bands. (c) H_z -field profile (left) and E^2 (right) profile of the fifth band (down) and fourth band (up) of the graphite photonic crystal lattice. (d) H_z -field profile (left) and E^2 (right) profile of the fourth band (down) and fifth band (up) of the Slot-graphite photonic crystal lattice.

We calculated the temporal confinement of the slot mode at the Γ -point. Figure 6-3 (a) shows the dependence of the Q factor (red curve) and wavelength (black line) on the slot height w_y , with fixed width $w_x = 0.675a$. The simulation is performed by solving the Maxwell equations using a 3D finite difference time-domain (FDTD) code, Lumerical. Interestingly, the Q factor increases from 1970 for $w_y = 0.06a$ until reaching 4.3×10^5 for $w_y = 0.0925a$. As we further increase the slot width, the Q factor decreases to 3100 for $w_y = 0.1225a$. On the other hand, the mode wavelength decreases as w_y increases, following a linear trend.

Figure 6-3 (b) shows the evolution of the Q factor (red curve) and wavelength (black line) with slot width w_x , for fixed slot height $w_y = 0.0925a$. The Q factor decreases as w_x is increasing. Note that the Q factor is less sensitive to w_x than w_y . For example, a change of w_x of 20 nm with respect to the peak preserves a Q-factor over 85000 (20% of the peak value). While changing 20 nm of w_y from the peak value decreases Q from 4.3×10^5 to 4300 (1% of the initial value). The evolution of the wavelength with w_x has two regions clearly differentiated: one with $w_x < 0.675a$ and another one with $w_x > 0.675a$. In the first region, the wavelength change is the ~ 1 nm for a 76 nm decrement in the slot length. In the second region, there is a change of ~ 9 nm for a 78 nm increment in the slot length.

After evaluating the temporal confinement, we evaluate the spatial confinement by calculating modal volume per unit cell. For the slot mode with the Q factor 4.3×10^5 , we obtain a value of $V_{eff} = 0.036(\lambda / 2n_b)^3$. This value of the spatial confinement compares well with the previous results obtained in PhC microcavities [14, 15].

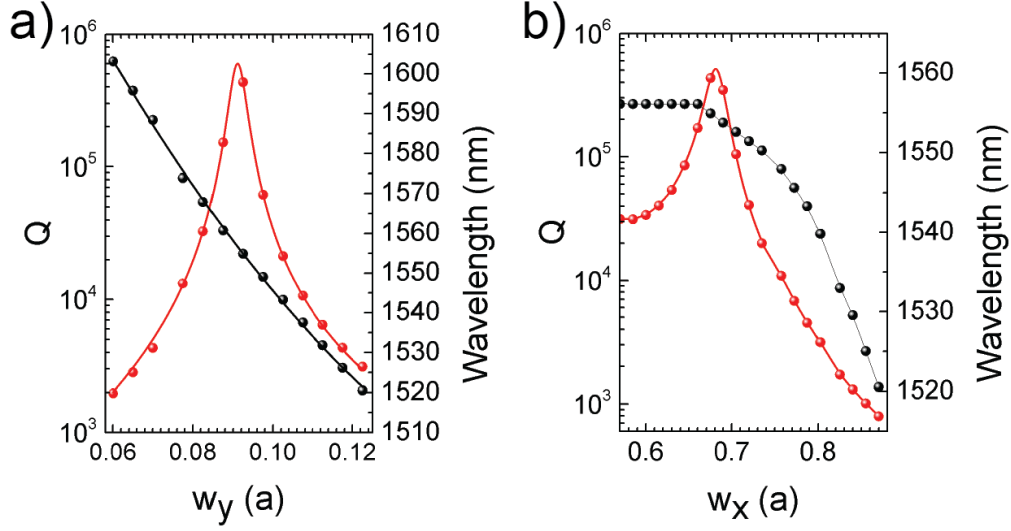


Figure 6-3 (a): Evolution of the Q and wavelength as function of w_y . (b): Evolution of the Q and wavelength as function of w_x . Red color for Q. Black for wavelength. Dots: Corresponds to the calculate values. Lines represents a guide for the eye.

6.3 Fabrication and Optical Characterization

We fabricate a group of slot-graphite photonic crystal devices in order to characterize the evolution of the slot modes with varying slot height w_y . The devices are fabricated with fixed lattice constant $a=820$ nm, radius of air holes $r/a=0.155$, and slab thickness $t=250$ nm. We adjust the device parameters so that we have a relatively low $Q < 10^5$ for easier optical characterization. We expect to see the resonant wavelengths of slot modes fall in our tunable laser range, and the Q factor will show an increasing-then-decreasing trend with increasing w_y . The computed Q factor is not far away of the highest values (Q-factor over 9800) we measured previously in the same set-up for uncoupled guided resonant modes [16].

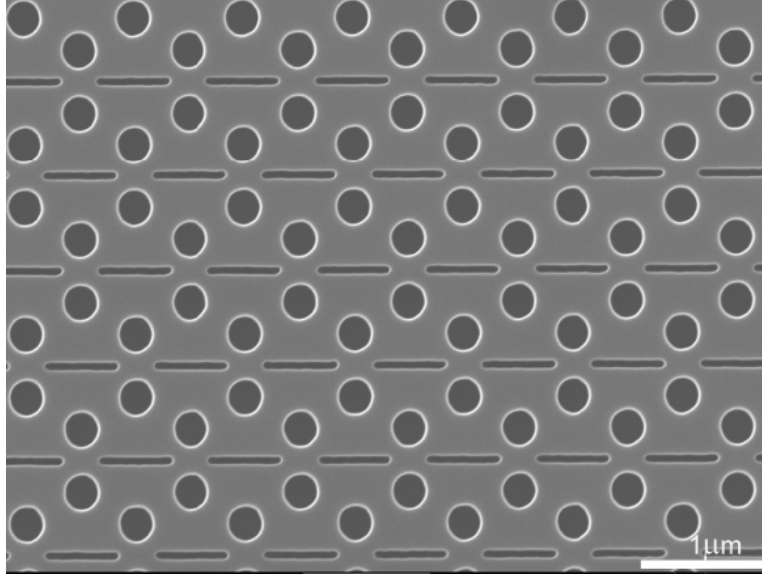


Figure 6-4 SEM image of one fabricated Slot-graphite device.

The devices have been fabricated using e-beam lithography and inductively-coupled plasma reactive ion etching (ICP-RIE). We use a 250 nm thick silicon layer on top of a 3 μm silica layer (SOITEC). The sample was spin-coated with PMMA-A4 950K. Using Raith150 e-beam system, a 50 μm diameter Slot-graphite pattern has been exposed with an acceleration voltage of 30KV. The pattern is transferred from the resist to the silicon layer by an ICP-RIE machine using a gas mixture $\text{SF}_6/\text{C}_4\text{F}_8$. Finally the remaining resist was removed using O_2 plasma etching and acetone. Figure 6-4 shows a Scanning-electron beam (SEM) image of one of the fabricated devices. We analyze the SEM images and extract geometrical parameters [17]. The slot width w_x is fixed to 550 nm, and w_y is increased gradually from 58 nm to 93 nm at 3.3 nm by each step. Note that the SEM inspection can introduce large systematic errors as much as 5–10% of the absolute dimension [18].

We characterize the transmission spectra of our fabricated samples using cross polarization configuration. The sample was immersed in deionized water. We measure the wavelength and Q factor of the slot modes using our experimental configuration as shown by Figure 6-5 (a). Incident light of a tunable laser (TL) in near-infrared range between 1500 nm and 1620 nm is collimated from fiber to free space by a lens (LS). The light is focused onto the sample on translation stage (TS) using a low numerical aperture microscope objective (MO). The light transmitted through the sample is collected using another microscope objective and focused onto a photodetector (PD). Note that two crossed polarizers (PC) are positioned before and after the microscope objectives, which can cancel out the Fabry-Perot background in the guided-resonance transmission. With the cross-polarization setup, we measured slot modes as peaks in the transmission spectrum rather than dips on the Fabry-Perot background as shown by Figure 6-5 (b) in the previous section. Figure 6-5 (b) shows a transmission spectrum measured in a slot-graphite device. The slot mode corresponding to the fifth band and the dipole mode corresponding to the fourth band are clearly visible.

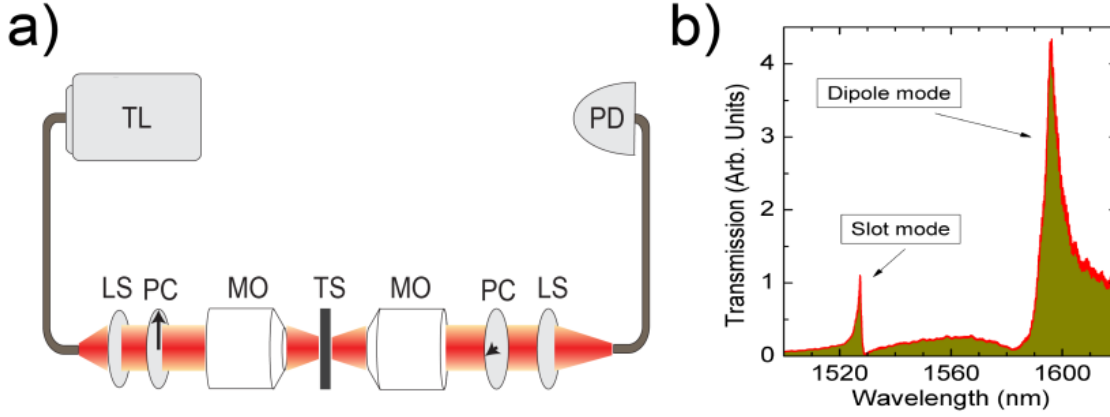


Figure 6-5 (a) Diagram of experimental setup used to characterize the optical properties of the guided resonant device. Two cross polarizers (PC) are applied before and after the device to cancel out Fabry-Perot noise. TL: tunable laser; MO: microscope objective; LS: lens; TS: translation stage; PD: photodiode. (b) One measured spectrum. The right transmission peak correspond to the slot mode, and the left peak shows the dipole mode with lower Q-factor.

The tested Q-factor and wavelength of the slot modes are plotted by black spheres in Figure 6-6. We did not plot the evolution of the dipole modes for simplicity. We compared the experimental data with the simulation shown by gray dashed curves in Figure 6-6. In FDTD simulation we take into account water absorption in the near-infrared range.

As shown by Figure 6-6 (a), within our expectation, the measured Q-factor first increased and then decreased with increasing w_y . The measured data are missing for devices with w_y between 65 nm and 71 nm. The possible reason is that the slot modes in these devices have high Q factors. For high Q modes, it is more challenging for external light to couple into the mode. We see the intensity of the transmission peaks for guided resonance comparable with the background noises. Due to the low signal-to-noise ratio, we did not obtain corresponding Q factors and wavelengths. The highest Q we measured is around 5300. Note that compared with

simulation (gray dashed curve), the tested Q is lower by a factor of 2. This offset may be due to fabrication imperfection and surface roughness.

Figure 6-6 (b) shows the tested wavelength evolution (black spheres) and the corresponding simulation (gray dashed curve). The measured wavelength monotonically decreases from 1613 nm to 1560 nm with w_y increasing from 58 nm to 93 nm. On average, the wavelength decreases by 1.5 nm if w_y is increased by 1 nm.

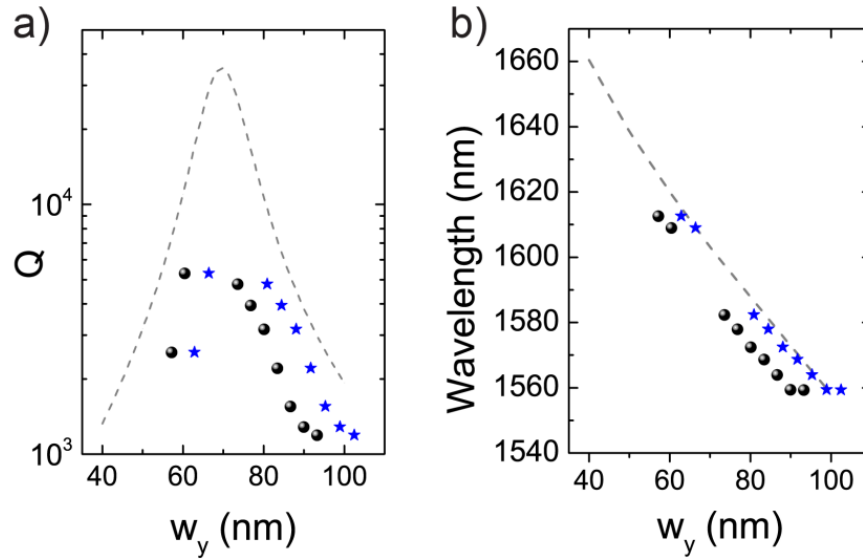


Figure 6-6 (a): Evolution of the Q factor as function of w_y . (b): Evolution of the wavelength as function w_y . Black spheres for experimental data. Gray dashed curves for simulation. Blue stars for experimental data when w_y is increased by 10% by considering SEM system errors.

The overall wavelength and Q-factor trends follow our simulation curves. However, the tested wavelength is smaller than simulated value by about 15 nm. One reason is that the wavelength is very sensitive to slot height w_y , while the w_y value we obtained through the SEM

images can have offset as much as 10% of the feature dimension [18]. We use the blue stars in Figure 6-6 to show the experimental data if the real slot height w_y is increased by 10% of the SEM size. In this case, the tested and simulated wavelengths are in good agreement.

6.4 Summary

A new photonic crystal lattice has been proposed as slot-graphite lattice. The lattice is created by using the graphite lattice as the base and placing a slot in the center of unit cell. Quality factors over 4×10^5 are predicted for guided resonance modes with light well confined within slots. The structures have been fabricated on SOI wafer and immersed in D.I. water for measurement. The modes have been characterized by cross-polarization transmission spectroscopy. The evolution of the Q factors and wavelengths follows the trend predicted by our simulations. Quality factors up to 5300 have been measured. Due to highly tunable Q factor and strong light confinement, the lattice is promising for lower-power light assisted, templated assembly.

6.5 Chapter References

- [1]. C. Monat, C. Seassal, X. Letartre, P. Regreny, P. Rojo-Romeo, P. Viktorovitch, M. L. V. d'Yerville, D. Cassagne, J. P. Albert, E. Jalaguier, S. Pocas, and B. Aspar, "InP-based two-dimensional photonic crystal on silicon: In-plane Bloch mode laser," *Applied Physics Letters* **81**, 5102-5104 (2002).
- [2]. H.-Y. Ryu, S.-H. Kwon, L. Yong-jae, Y.-H. Lee, and J.-S. Kim, "Very-low-threshold photonic band-edge lasers from free-standing triangular photonic crystal slabs," *Applied Physics Letters* **80**, 3476-3478 (2002).

- [3]. J. Mouette, C. Seassal, X. Letartre, P. Rojo-Romeo, J. L. Leclercq, P. Regreny, P. Viktorovitch, E. Jalaguier, R. Perreau, and H. Moriceau, "Very low threshold vertical emitting laser operation in InP graphite photonic crystal slab on silicon," *Electronics Letters* **39**, 526-528 (2003).
- [4]. N. Chauvin, P. Nedel, C. Seassal, B. Ben Bakir, X. Letartre, M. Gendry, A. Fiore, and P. Viktorovitch, "Control of the spontaneous emission from a single quantum dash using a slow-light mode in a two-dimensional photonic crystal on a Bragg reflector," *Physical Review B* **80**, 045315 (2009).
- [5]. M. Huang, A. A. Yanik, T.-Y. Chang, and H. Altug, "Sub-wavelength nanofluidics in photonic crystal sensors," *Opt. Express* **17**, 24224-24233 (2009).
- [6]. T. Ochiai, and K. Sakoda, "Dispersion relation and optical transmittance of a hexagonal photonic crystal slab," *Physical Review B* **63**, 125107 (2001).
- [7]. S. Fan, and J. D. Joannopoulos, "Analysis of guided resonances in photonic crystal slabs," *Physical Review B* **65**, 235112 (2002).
- [8]. D. Cassagne, C. Jouanin, and D. Bertho, "Photonic band gaps in a two-dimensional graphite structure," *Physical Review B* **52**, R2217-R2220 (1995).
- [9]. G. Alagappan, X. W. Sun, and H. D. Sun, "Symmetries of the eigenstates in an anisotropic photonic crystal," *Physical Review B* **77**, 195117 (2008).
- [10]. L. C. Andreani, and D. Gerace, "Photonic-crystal slabs with a triangular lattice of triangular holes investigated using a guided-mode expansion method," *Physical Review B* **73**, 235114 (2006).
- [11]. V. R. Almeida, Q. Xu, C. A. Barrios, and M. Lipson, "Guiding and confining light in void nanostructure," *Opt. Lett.* **29**, 1209-1211 (2004).
- [12]. T. Yamamoto, M. Notomi, H. Taniyama, E. Kuramochi, Y. Yoshikawa, Y. Torii, and T. Kuga, "Design of a high-Q air-slot cavity based on a width-modulated line-defect in a photonic crystal slab," *Opt. Express* **16**, 13809-13817 (2008).
- [13]. X. Letartre, C. Monat, C. Seassal, and P. Viktorovitch, "Analytical modeling and an experimental investigation of two-dimensional photonic crystal microlasers: defect state (microcavity) versus band-edge state (distributed feedback) structures," *J. Opt. Soc. Am. B* **22**, 2581-2595 (2005).
- [14]. J. T. Robinson, C. Manolatou, L. Chen, and M. Lipson, "Ultrasmall Mode Volumes in Dielectric Optical Microcavities," *Physical Review Letters* **95**, 143901 (2005).

- [15]. S. Kita, S. Hachuda, K. Nozaki, and T. Baba, "Nanoslot laser," *Applied Physics Letters* **97**, 161108-161103.
- [16]. L. J. Martinez Rodriguez, E. Jaquay, J. Ma, and M. L. Povinelli, "Fabrication and optical characterization of high-Q guided mode resonances in a graphite-lattice photonic crystal slab," in *CLEO: Science and Innovations*(Optical Society of America), p. JW4A.78.
- [17]. M. Skorobogatiy, G. Begin, and A. Talneau, "Statistical analysis of geometrical imperfections from the images of 2D photonic crystals," *Opt. Express* **13**, 2487-2502 (2005).
- [18]. D. M. Beggs, L. O'Faolain, and T. F. Krauss, "Accurate determination of the functional hole size in photonic crystal slabs using optical methods," *Photonics and Nanostructures - Fundamentals and Applications* **6**, 213-218 (2008).

Chapter 7: Radiation Loss in Photonic Crystal CROW

7.1 Background

Coupled resonator optical waveguides (CROWs) [1], waveguides in which light propagates by “hopping” between localized resonator modes, have been widely studied for application to on-chip optical delays [2]. CROWs provide both slow group velocity and low dispersion [3], essential features for distortion-free signal delay. In dynamically-tuned CROWs, light pulses may be stopped, stored, and released on demand [4, 5]. CROWs based on various resonator types have been investigated, including microring resonators [6-8] and photonic-crystal microcavities [9-15]. We focus here on photonic-crystal microcavity CROWs, which provide both compact resonator size and high spatial confinement; the latter is useful, for example, for achieving nonlinear effects at low power levels [16].

Minimization of propagation loss is an important aspect of CROW design. Various approaches have been used to design low-loss CROWs, including coupled-mode theory [17] and the finite-element method [18]. CROWs formed by microcavities in photonic-crystal slabs are intrinsically lossy, because the CROW mode lies above the light line of air, the mode leaks light vertically as it propagates [19]. Moreover, if the loss is uneven across the CROW band for different wavevectors, the effective transmission bandwidth is reduced, and the transmitted signal is distorted. The intrinsic loss provides a lower bound on the total loss, which may also include contributions due to fabrication imperfections and scattering.

Previous theoretical work has shown that intrinsic CROW loss can depend strongly on frequency and be up to an order of magnitude larger or smaller than that of an individual

resonator [20, 21]. At the same time, experiments have demonstrated particular CROW designs with low loss comparable to that of an individual resonator [22]. Given these considerations, it is important to understand theoretically how the CROW and resonator losses are related, as well as how to achieve low, flat loss across the entire CROW bandwidth. In this paper, we use a model based on the tight-binding approximation (TBA) to answer these questions.

TBA approaches are advantageous, as they allow the calculation of the frequency-dependent loss of a CROW from a single, full-field simulation of an individual cavity. Previously, Fussell and Dignam have used a TBA model based on the complex dispersion relation of the CROW to calculate losses [21]. Another approach is to use the TBA to relate the electromagnetic fields of the CROW to those of the isolated cavity [15]. In this case, the spatial power spectrum of the CROW fields may be obtained from that of the isolated cavity by taking discrete samples in Fourier space, as experimentally demonstrated in [15]. Reference [15] has suggested that the losses may then be calculated from the power spectrum using a light-cone picture [23]. In this paper, we explicitly demonstrate the validity of this approach by comparing the predictions of the TBA light-cone model with direct calculations. We then show that within a particular family of photonic-crystal cavities, a decrease in cavity loss also results in a decrease in CROW loss. While the CROW loss generally varies across the CROW band, we show that the TBA predicts particular cavity separations for which the loss is flat.

We expect our results to be useful for a range of applications. In the context of light-assisted self assembly above photonic-crystal slabs [24, 25], our method may facilitate the design of large-area, coupled-cavity modes with high quality factor that nevertheless couple to normally-incident radiation. For slow- and stopped-light applications, the fidelity of signal transmission at

the end of a delay line depends on achieving low, flat loss across the signal bandwidth. In coupled-cavity lasers, the ability to tailor the $Q(k)$ loss profile could provide a useful method to control the effects of mode competition and tune the directional output of the laser.

7.2 Theoretical Formulation in the Tight-binding Approximation

For concreteness, we first consider the CROW structure shown in Figure 7-1 (a). The photonic crystal slab is a triangular lattice of air holes with lattice constant a and hole radius r in a suspended, dielectric slab with height h and refractive index n (1.55 μm). The CROW waveguide consists of periodically spaced defects. Each defect is a micro-cavity with two adjacent missing holes, known as an L2 cavity. The center-to-center spacing of adjacent defects is $5a$. The separation width S , the width of the region between defects that does not contain missing holes, is $3a$. We denote the CROW as $L_m S_n$, with m being the number of missing holes of the constituent cavity and n the number of separation holes. We calculate the band structure by the guided-mode expansion method [26]. Figure 7-1 (b) shows the dispersion relations for L2S2, L2S3, and L2S4 CROWs, respectively. The band of each CROW mode displays a cosinusoidal shape [1, 3], with the center frequency close to the fundamental mode of the isolated L2 cavity, $0.26992(2\pi c/a)$. The bandwidth of a CROW mode is proportional to the coupling strength between adjacent defects. Figure 7-1 (b) shows that the coupling strength decreases as the separation is increased.

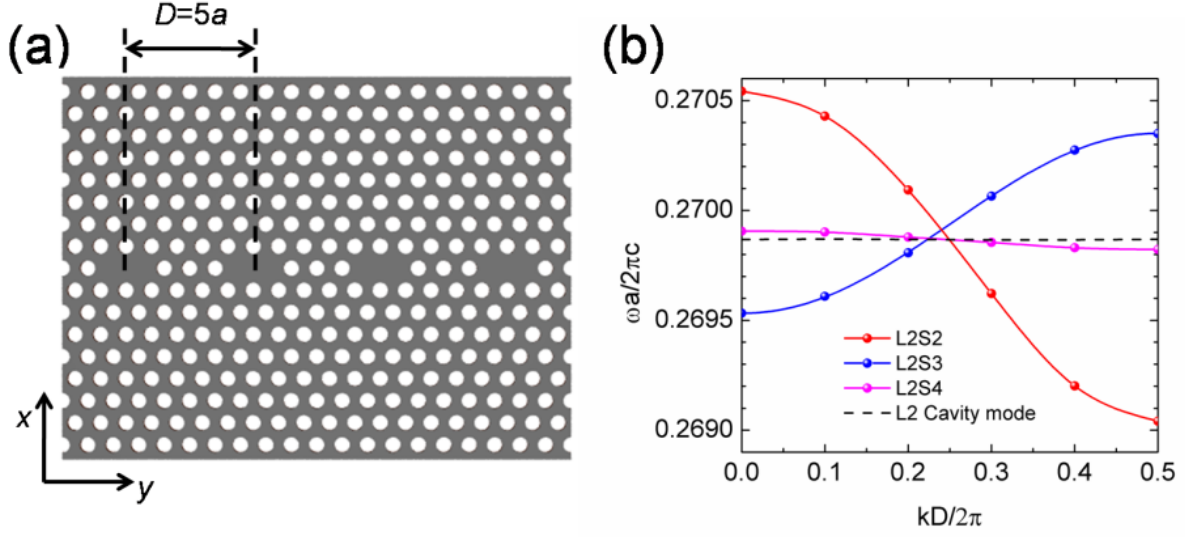


Figure 7-1 (a) Schematic diagram of CROW structure L2S3. (b) Dispersion curve of CROW mode in L2S2 (red), L2S3 (blue) and L2S4 (magenta). Dashed line shows the fundamental mode of the isolated L2 cavity.

For all three CROWs, the CROW band lies above the light line of air and is thus intrinsically lossy. The light line of air is given by $\omega = ck$, where k is the in-plane CROW wavevector. At the edge of the Brillouin zone, $k = k_{Bz} \equiv \pi / D$ and the light-line frequency $\omega = 0.125(2\pi c/a)$, $0.1(2\pi c/a)$, or $0.083(2\pi c/a)$ for $D = 4a$, $D = 5a$ or $D = 6a$, respectively. In all three cases, the upper edge of the light line lies well below the frequency range shown in Figure 7-1(b).

We define a waveguide quality factor $Q(k)$ to describe the leakage of the CROW mode:

$$Q(k) = \omega(k) \tau_{1/e} \quad (7-1)$$

where $\omega(k)$ is the dispersion relation of the CROW mode, and $\tau_{1/e}$ is the time in which the power in the waveguide mode decays by $1/e$. $Q(k)$ can be converted to a $1/e$ power-decay length in the waveguide as $L_{1/e}(k) = v_g(k)Q(k) / \omega(k)$, where $v_g(k)$ is the group velocity. Alternately, the loss

in dB/length is equal to $-4.34\text{dB}/L_{1/e}$. While the loss per unit length diverges at $k = 0$ and $0.5(2\pi/D)$ where $v_g=0$, $Q(k)$ is well defined over the entire Brillouin zone.

7.2.1 Light Line Picture

For isolated microcavities, it has been shown [23] that the cavity Q can be related to the Fourier transform of the electromagnetic fields above the surface of the slab. A similar relation is true for the waveguide quality factor $Q(k)$.

We can write:

$$Q(k) = \omega(k) \frac{\langle U(k) \rangle}{\langle P(k) \rangle} \quad (7-2)$$

where $\langle U(k) \rangle$ is the time-averaged electromagnetic field energy:

$$\langle U(k) \rangle = \frac{1}{2} \iiint_V dV \left(\epsilon_{CROW}(x, y, z) |\vec{E}_k(x, y, z)|^2 + \mu_o |\vec{H}_k(x, y, z)|^2 \right), \quad (7-3)$$

where $\epsilon_{CROW}(x, y, z)$ is the dielectric constant of the CROW, and $\vec{E}_k(x, y, z)$ and $\vec{H}_k(x, y, z)$ are the electric and magnetic fields of the CROW mode at wave vector k . $\langle P(k) \rangle$ is the time-averaged emitted power,

$$\langle P(k) \rangle = \oint_S d\vec{S} \cdot \frac{1}{2} \text{Re} \left(\vec{E}_k(x, y, z) \times \vec{H}_k^*(x, y, z) \right), \quad (7-4)$$

where the integral is over a closed surface that encloses the photonic crystal slab. For an infinitely long CROW, both $\langle U(k) \rangle$ and $\langle P(k) \rangle$ are infinite; however, the ratio $\langle U(k) \rangle / \langle P(k) \rangle$ is finite and equal to the value of the ratio for a single unit cell.

$\langle P(k) \rangle$ can be rewritten in terms of the two-dimensional (2D) spatial power spectra of the free-space fields, on any surface above the structure [23] :

$$\begin{aligned} \langle P(k) \rangle = & \frac{1}{2} \sqrt{\frac{\mu_o}{\epsilon_o}} \iint_{q_{\parallel} \leq \omega(k)/c} \frac{dq_x}{2\pi} \frac{dq_y}{2\pi} \left\{ \frac{\epsilon_o}{\mu_o} \left(\left| \tilde{E}_{k,x}(q_x, q_y) \right|^2 + \left| \tilde{E}_{k,y}(q_x, q_y) \right|^2 \right) \right. \\ & \left. + \left(\left| \tilde{H}_{k,x}(q_x, q_y) \right|^2 + \left| \tilde{H}_{k,y}(q_x, q_y) \right|^2 \right) \right\} \end{aligned} \quad (7-5)$$

where $q_{\parallel} = (q_x^2 + q_y^2)^{1/2}$ and $\tilde{E}_{k,i}(q_x, q_y)$ and $\tilde{H}_{k,i}(q_x, q_y)$ are the 2D Fourier transforms of the i th component of $\vec{E}_k(x, y, z)$ and $\vec{H}_k(x, y, z)$, and ($i \in x, y$):

$$\begin{aligned} \tilde{E}_{k,i}(q_x, q_y) &= \iint dx dy E_{k,i}(x, y) e^{-i(q_x x + q_y y)} \\ \tilde{H}_{k,i}(q_x, q_y) &= \iint dx dy H_{k,i}(x, y) e^{-i(q_x x + q_y y)} \end{aligned} \quad (7-6)$$

The Fourier-space integral includes all q_{\parallel} within the light cone ($q_{\parallel} \leq \omega/c$). Only these so-called “leaky components” contribute to radiation loss. We will refer to the quantities $\left| \tilde{E}_{k,x}(q_x, q_y) \right|^2$, $\left| \tilde{E}_{k,y}(q_x, q_y) \right|^2$, $\left| \tilde{H}_{k,x}(q_x, q_y) \right|^2$, and $\left| \tilde{H}_{k,y}(q_x, q_y) \right|^2$ appearing in Equation (7-5) as the E_x , E_y , H_x , and H_y power spectra, respectively.

Due to the periodicity of the CROW waveguide in the x -direction, Fourier transforms of the field components are only nonzero for discrete values of q_x . Using Bloch’s theorem, the CROW mode can be written as $\vec{E}_k(x, y, z) = e^{ikx} \vec{U}_k(x, y, z)$, where $\vec{U}_k(x + D, y, z) = \vec{U}_k(x, y, z)$. An analogous statement is true for $\vec{H}_k(x, y, z)$. It follows that the Fourier transforms

$\tilde{E}_{k,i}(q_x, q_y) = \tilde{H}_{k,i}(q_x, q_y) = 0$ except when $q_x = k + 2\pi n / D$. The Fourier transforms are nonzero over a continuous range of q_y values.

7.2.2 Tight-binding Approximation

The tight-binding approximation can be used to write the CROW quality factor in terms of the fields of the isolated cavity.

First, we write the CROW fields in terms of the isolated cavity fields $\vec{E}_\Omega(x, y, z)$ and $\vec{H}_\Omega(x, y, z)$:

$$\begin{aligned}\vec{E}_k(x, y) &= E_0 \sum_{n=-\infty}^{\infty} e^{inkD} \vec{E}_\Omega(x - nD, y, z) \\ \vec{H}_k(x, y) &= H_0 \sum_{n=-\infty}^{\infty} e^{inkD} \vec{H}_\Omega(x - nD, y, z)\end{aligned}\tag{7-7}$$

where E_0 and H_0 are normalization constants [1]. Taking into account that

$$\sum_{n=-\infty}^{\infty} e^{-inx} = 2\pi \sum_{l=-\infty}^{\infty} \delta(x - 2\pi l)\tag{7-8}$$

It follows that

$$\begin{aligned}\left| \tilde{E}_{k,i}(q_x, q_y) \right|^2 &= |E_0|^2 \left(\frac{2\pi}{D} \right) \sum_{m=-\infty}^{\infty} \sum_{n=-\infty}^{\infty} \delta\left(q_x - k - \frac{2\pi n}{D} \right) \left| \tilde{E}_{\Omega,i}(q_x, q_y) \right|^2 \\ \left| \tilde{H}_{k,i}(q_x, q_y) \right|^2 &= |H_0|^2 \left(\frac{2\pi}{D} \right) \sum_{m=-\infty}^{\infty} \sum_{n=-\infty}^{\infty} \delta\left(q_x - k - \frac{2\pi n}{D} \right) \left| \tilde{H}_{\Omega,i}(q_x, q_y) \right|^2\end{aligned}\tag{7-9}$$

where the sum over m can be interpreted as a sum over unit cells. This relation is schematically depicted in Figure 7-2(a). The tight-binding approximation predicts that for fixed q_y , the power spectrum of each field component of the CROW mode is given by a set of delta-function spikes weighted by the power spectrum of the isolated cavity. The spikes are shifted by k , and the separation between neighboring spikes is $2\pi / D$.

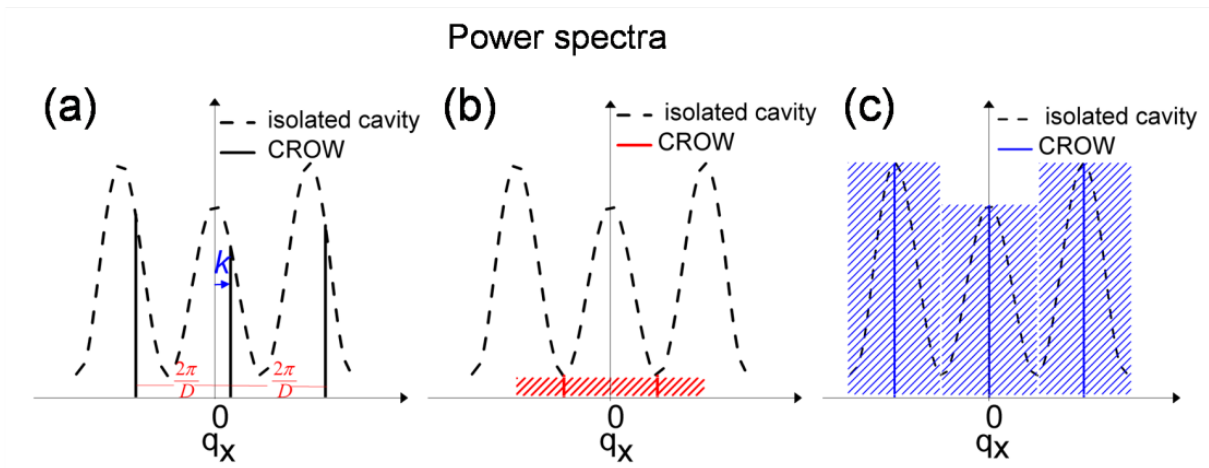


Figure 7-2 (a) Schematic picture of tight-binding prediction for the power spectrum of a CROW mode. (b) CROW power spectrum giving a large value of $Q(k)$ compared to the isolated cavity. (c) CROW Power spectrum giving a small value of $Q(k)$ compared to the isolated cavity.

Within the tight-binding approximation, $\langle P(k) \rangle$ can be found by substituting Equation (7-9) into Equation (7-5). $\langle U(k) \rangle$ can be found by substituting Equation (7-7) into Equation (7-3):

$$\begin{aligned} \langle U(k) \rangle = & \frac{1}{2} \iiint_V dV \left\{ \epsilon_{CROW}(x, y, z) E_0^2 \sum_{n=-\infty}^{\infty} \sum_{m=-\infty}^{\infty} e^{i(n-m)kD} \vec{E}_{\Omega}^*(x-nD, y, z) \vec{E}_{\Omega}(x-mD, y, z) \right. \\ & \left. + H_0^2 \sum_{n=-\infty}^{\infty} \sum_{m=-\infty}^{\infty} e^{i(n-m)kD} \vec{H}_{\Omega}^*(x-nD, y, z) \vec{H}_{\Omega}(x-mD, y, z) \right\} \end{aligned} \quad (7-10)$$

The $m = n$ terms will dominate, leading to the approximation that

$$\langle U \rangle \approx \frac{1}{2} \sum_{m=-\infty}^{\infty} \iiint_V dV \left\{ \varepsilon_{CROW}(x, y, z) E_0^2 \left| \tilde{E}_{\Omega}(x, y, z) \right|^2 + \mu_o H_0^2 \left| \tilde{H}_{\Omega}(x, y, z) \right|^2 \right\} \quad (7-11)$$

independent of k . For weak coupling between defects, we substitute ε_{Ω} , the dielectric function of the isolated cavity, for ε_{CROW} , and

$$\begin{aligned} \langle U \rangle &\approx \frac{1}{2} \sum_{m=-\infty}^{\infty} \iiint_V dV \left\{ \varepsilon_{\Omega}(x, y, z) E_0^2 \left| \tilde{E}_{\Omega}(x, y, z) \right|^2 + \mu_o H_0^2 \left| \tilde{H}_{\Omega}(x, y, z) \right|^2 \right\} \\ &\approx \sum_{m=-\infty}^{\infty} \langle U_{\Omega} \rangle \end{aligned} \quad (7-12)$$

where U_{Ω} is the field energy of the isolated cavity.

Using the expressions for $\langle P(k) \rangle$ and $\langle U(k) \rangle$, the final result is that

$$\begin{aligned} Q(k) &\approx \omega_o \langle U_{\Omega} \rangle \left[\frac{1}{2} \sqrt{\frac{\mu_o}{\varepsilon_o}} \left(\frac{2\pi}{D} \right) \iint_{q_{\parallel} \leq \omega/c} \frac{dq_x}{2\pi} \frac{dq_y}{2\pi} \sum_{n=-\infty}^{\infty} \delta \left(q_x - k - \frac{2\pi n}{D} \right) \times \right. \\ &\quad \left. \left\{ \frac{\varepsilon_o}{\mu_o} \left(\left| \tilde{E}_{\Omega,x}(q_x, q_y) \right|^2 + \left| \tilde{E}_{\Omega,y}(q_x, q_y) \right|^2 \right) + \left| \tilde{H}_{\Omega,x}(q_x, q_y) \right|^2 + \left| \tilde{H}_{\Omega,y}(q_x, q_y) \right|^2 \right\} \right]^{-1} \end{aligned} \quad (7-13)$$

Here, we have assumed that the variation in ω across the CROW band, $\Delta\omega$, is small compared to the isolated cavity frequency ω_0 . In this case, $\omega(k)$ can be approximated by ω_0 in Equation (7-13). For the numerical examples presented below, $\Delta\omega/\omega_0$ is on the order of 10^{-3} .

Equation (7-13) implies that within the tight-binding approximation, increasing Q_0 of the isolated cavity will tend to increase the $Q(k)$ of the corresponding waveguide. This is because an increase in Q_0 corresponds to a decrease in the power spectra values of the isolated cavity within the light cone. However, due to the discrete nature of the sum, $Q(k)$ can have a strong

dependence on the wave vector. This is illustrated schematically in Figures 7-2 (b) and (c). For a particular value of k , it may happen that the spikes in the CROW power spectrum line up with minima (Figure 7-2 (b)) or maxima (Figure 7-2 (c)) of the isolated cavity power spectrum. The Q_0 of the isolated cavity is inversely proportional to the area under the dashed line, while $Q(k)$ of the CROW mode is inversely proportional to the red or blue dashed areas shown. It is apparent that the dashed area can either be smaller (Figure 7-2 (b)) or larger (Figure 7-2 (c)) than the area under the curve. As a result, $Q(k)$ can be either larger or smaller than Q_0 .

In general, the validity of the TBA improves as the separation between cavities increases. For decreasing separation, as the fields of neighboring cavities interact more strongly, it becomes less accurate to write the CROW fields in terms of the isolated cavity mode (Equation (7-7)). We note that in the numerical examples below, we consider cavities in which the modes are well isolated and the spacing between modes is large compared to the width of the CROW band. In some CROW's, the simple model of a well isolated mode is not sufficient, and coupling with other modes of the isolated cavity must be considered. In this case, Equation (7-7) would be modified to include a sum over multiple cavity modes. The expansion coefficients in the sum can be found as in Reference [27], and Equations (7-10) and (7-13) would be similarly modified. In cases where nearest neighbour or next-nearest neighbor coupling are significant, the $m - n \neq 0$ terms should be included in the calculation of $\langle U(k) \rangle$ (Equation (7-10)).

7.3 Numerical Validation of the Tight Binding Approximation

To test the TBA model of the CROW quality factor, we perform three-dimensional finite-difference time-domain (FDTD) simulations [28] of $Q(k)$ for CROW structures and compare the

results with the TBA prediction of Equation (7-13). We start with CROW structures based on the L2 cavity, such as the one shown above in Figure 7-1 (a).

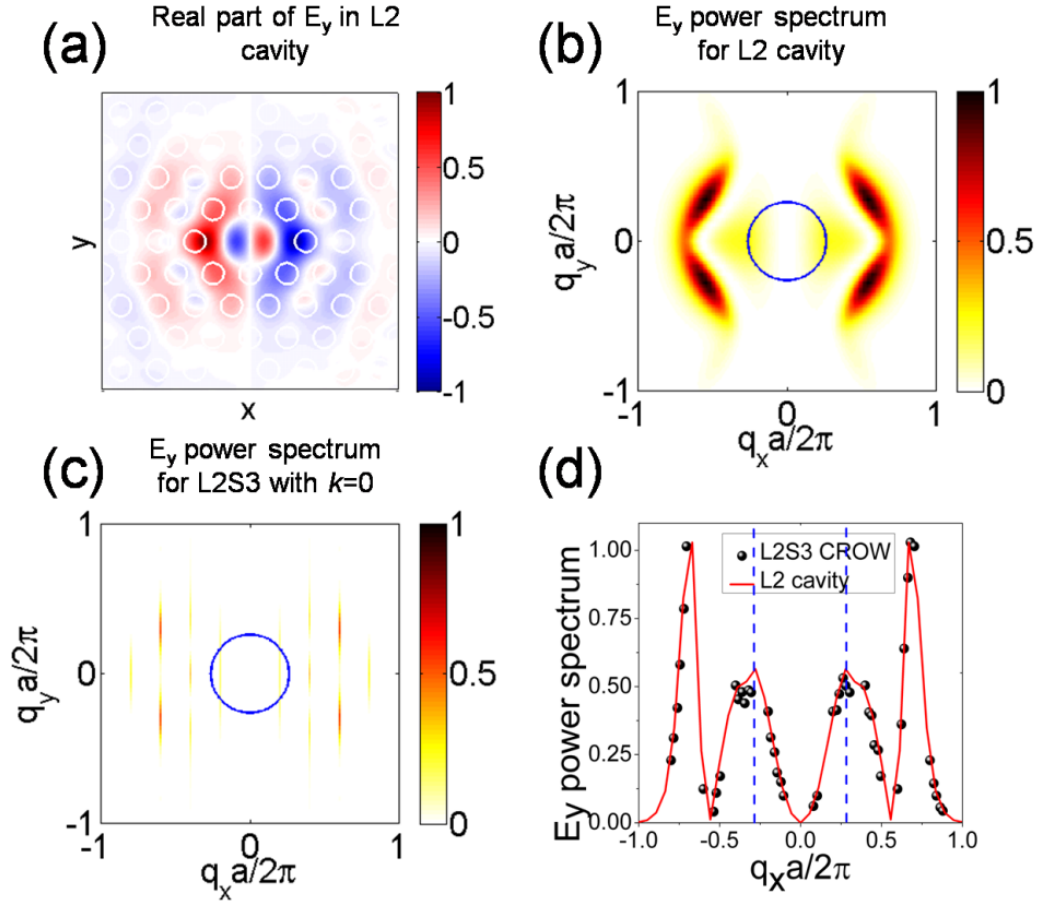


Figure 7-3 (a) Mode distribution of the real part of E_y on the x - y plane $0.2a$ above the surface of the isolated L2 cavity. (b) Power spectrum of L2 cavity. The blue circle is the light cone. (c) Power spectrum of CROW mode in L2S3 structure with $k = 0$. (d) Visual test of tight-binding approximation via comparison of CROW power spectra to that of isolated L2 cavity. The blue dashed lines indicate light lines.

For the isolated cavity simulation, a computational cell of $35a \times 10\sqrt{3}a \times 4a$ was used. Perfectly-matched layer (PML) boundaries were used in all directions, and the grid resolution was 20 grid points per a . In Figure 7-3 (a), we plot E_y for the fundamental mode of the L2 cavity on a plane $0.2a$ above the slab surface. The mode is antisymmetric with respect to both the x - z plane and y - z planes. Figure 7-3 (b) shows the E_y power spectrum, $|\tilde{E}_{\Omega,y}(q_x, q_y)|^2$ for the isolated cavity. We note that the power spectrum is zero along $q_x = 0$, due to the fact that $E_{\Omega,y}$ is odd with respect to $x = 0$. In Figures 7-3 (a) and (b), the field magnitude and power spectrum are each normalized to their maximum values.

We next calculate the full CROW fields and corresponding power spectrum. We use the FDTD method to simulate a single unit cell of the L2S3 CROW. The boundary conditions are fixed to be Bloch-periodic in the x -direction with fixed wave vector k . In the y -direction, the length of the computational cell is chosen to be large enough ($10\sqrt{3}a$) for $Q(k)$ to be independent of length. Perfectly-matched layer boundaries are applied in the y and z directions. The grid resolution was 20 points per a . We divide the calculated field components by e^{ikx} to obtain the periodic field envelopes. We then Fourier transform the envelopes and shift them by k in the q_x -direction, a procedure that can easily be shown to yield $|\tilde{E}_{k,i}(q_x, q_y)|^2$ and $|\tilde{H}_{k,i}(q_x, q_y)|^2$. In Figure 7-3 (c), we plot the E_y power spectrum of the L2S3 CROW mode for $k = 0$. The CROW power spectrum is only nonzero at discrete values of q_x separated by a distance $\Delta q_x = (1/5)(2\pi/a) = 0.2(2\pi/a)$. In this case, only three values of q_x fall within the light cone, $q_x = 0$ and $q_x = \pm 0.2(2\pi/a)$. The power spectrum is zero for $q_x = 0$, since E_y is odd with respect to $x = 0$.

Within the TBA, the CROW power spectrum can be found by using the Dirac delta function to sample the power spectrum of the isolated cavity mode (Equation (7-9)). To test this approximation quantitatively, we plot the values of the L2 isolated cavity power spectrum (red curve) and the L2S3 CROW power spectra (black dots) along $q_y = 0$ in Figure 7-3 (d). Multiple values of k are shown on the same plot, and the blue dashed lines indicate the position of the light lines. The overall agreement is quite good.

As a further check of the TBA model, we quantitatively compare the results for $Q(k)$ to those obtained by direct simulation of the full CROW structure. Figure 7-4 shows results for CROW waveguides with varying separation between cavities: Figures 7-4 (a-c) correspond to L2S2, L2S3, and L2S4 CROWs, respectively. Q_o for the isolated cavity is shown by the red lines and has a value of 1440.

The results labeled “FDTD” and “FDTD-LC” represent two different, direct methods for calculating $Q(k)$ from the full CROW structure. In both cases, a Bloch periodic unit cell with fixed k was used, as described above. A narrowband, pulsed source was used to excite the mode of interest. In the first case (“FDTD,” black lines) $Q(k)$ was calculated from the field decay time after source turn-off. In the second case (“FDTD-LC”, magenta lines), $Q(k)$ was instead calculated from an integral over the CROW fields via the light-cone approach (Equations (7-2)-(7-5)). The agreement between the two direct methods is good, indicating the validity of the light-cone formulation for CROW modes. For high-Q modes, one might expect the “FDTD” method to be more accurate than the “FDTD-LC” method, which depends on an integral over small field components and may therefore be more susceptible to numerical error than the extraction of a decay time.

The results labeled “TBA” are obtained by using the tight-binding approximation to calculate $Q(k)$ from the isolated cavity mode, via Equation (7-13) (blue lines). The TBA is shown to predict the $Q(k)$ well. The maximum difference between the TBA method and the FDTD method is 12% for L2S2, 7% for L2S3, and 3% for L2S4. As expected, the accuracy of the TBA improves with increasing cavity separation. Importantly, using the TBA allows the prediction of the entire $Q(k)$ curve for all three CROWs from only a single calculation of the isolated cavity mode.

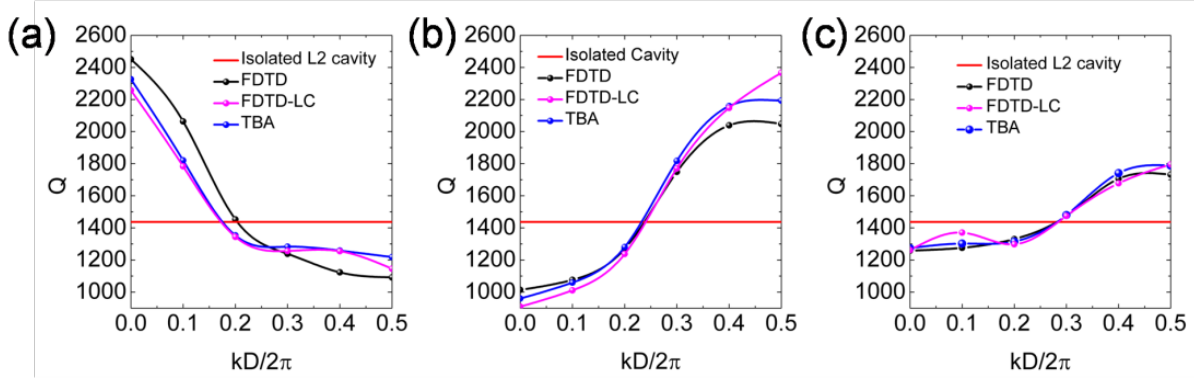


Figure 7-4 $Q(k)$ for L2 CROWs with varying cavity separations: (a) L2S2, (b) L2S3, and (c) L2S4. Dots represent calculated values. Lines represent guides for the eye.

From Figure 7-4, we notice that the k -dependence of the CROW quality factor, $Q(k)$, is not universal. Q may increase or decrease with k , depending on cavity separation. For all three cases shown (L2S2, L2S3, and L2S4), the minimum and maximum values of $Q(k)$ occur at either $k = 0$ or $k = k_{Bz} = 0.5(2\pi / D)$. Depending on k , the CROW mode can have either a higher or lower quality factor than the isolated cavity. In the middle of the Brillouin zone, the quality factors are similar. At $k = 0.25(2\pi / D)$, the difference between $Q(k)$ of the CROW and Q_o of the isolated cavity is below 10% for all three cavity separations shown.

Interestingly, while the L2 cavity mode cannot emit light vertically due to symmetry considerations [29], the CROW can. For the isolated cavity, symmetry prohibits coupling to a plane wave propagating in the z -direction. However, leakage occurs in off-normal directions, yielding a finite quality factor. For the CROW mode at $Q(k=0)$, symmetry again prohibits coupling to a z -propagating plane wave. However, translational symmetry requires that any leakage be in the z -direction. The finite value of $Q(k=0)$ indicates that vertical leakage does occur; in this case, it arises from interference between off-normal plane waves radiated from the individual cavities.

7.4 Factors Influencing the CROW Quality Factor

The results above verify that the TBA model is a good predictor of $Q(k)$ in CROWs based on the L2 cavity. Using the TBA, we can gain insight into how the CROW quality factor depends on wave vector, cavity separation, and the quality factor of the isolated cavity.

In Figure 7-5, we plot $Q(k)$ for L2 CROWs as a function of cavity separation (black lines). Triangles indicate $Q(0)$, and circles indicate $Q(k_{Bz})$. All values are calculated using the TBA. We see from the figure that $Q(0)$ and $Q(k_{Bz})$ oscillate around the Q_o of the isolated cavity, shown by the dashed line. Interestingly, $Q(0)$ and $Q(k_{Bz})$ are always on opposite sides of Q_o . As a result, it is never the case that $Q(k)$ is larger or smaller than Q_o for all k . As the number of separation holes is increased, both $Q(0)$ and $Q(k_{Bz})$ approach Q_o . This trend is intuitive; in the limit of large separation, the CROW can be viewed as a chain of isolated cavities.

We next increase the length of the cavity. Results for L3 CROWs are shown by red lines in Figure 7-5 (a). It can be seen from the figure that $Q(0)$ and $Q(k_{Bz})$ again oscillate around the

isolated cavity value. Moreover, the increase in the isolated cavity Q_o between L2 and L3 corresponds to an increase in $Q(k)$. Similarly, we can form CROWs from L4 or L5 cavities (blue and magenta lines in Figure 7-5 (a)). Within the family of L2 to L5 cavities, the CROW quality factor increases with the quality factor of the isolated cavity. This result corresponds to the intuitive argument presented above in (Section 7.2). As the quality factor of the isolated cavity increases, the components of its power spectrum inside the light line decrease. This also tends to decrease the leaky components of CROW power spectrum, which may be obtained from the cavity power spectrum via Fourier component sampling.

For each cavity length (or data color) shown in Figure 7-5 (a), we notice that there are nodes where $Q(0)$ and $Q(k_{Bz})$ cross. At these points, we expect $Q(k)$ to be flat. In Figure 7-5 (b), we plot $Q(k)$ for CROWs designed with a number of separation holes equal to the first node in Figure 7-5 (a). In all cases, the variation in $Q(k)$ is small compared to Figure 7-5 (a). For L3 and L4, the number of separation holes is equal to 3. We thus obtain designs for CROWs whose loss is similar to the isolated cavity across the entire band. For L2 and L5, the ideal separation is non-integer. While loss values can be calculated within the TBA, it is not obvious how to achieve non-integer separations in a real CROW structure. However, we have verified via direct FDTD simulations that for the L2 cavity, simply using a CROW unit cell of $4.4a$ and allowing a slight overlap of circular holes at each edge of the cell yields a similarly flat $Q(k)$ trend to that pictured, though at somewhat higher values. We have also verified via FDTD simulations (not shown) that in L3, L4 and L5 cavities, the TBA method gives accurate results for $Q(k)$ provided that the number of separation holes is greater than 2.

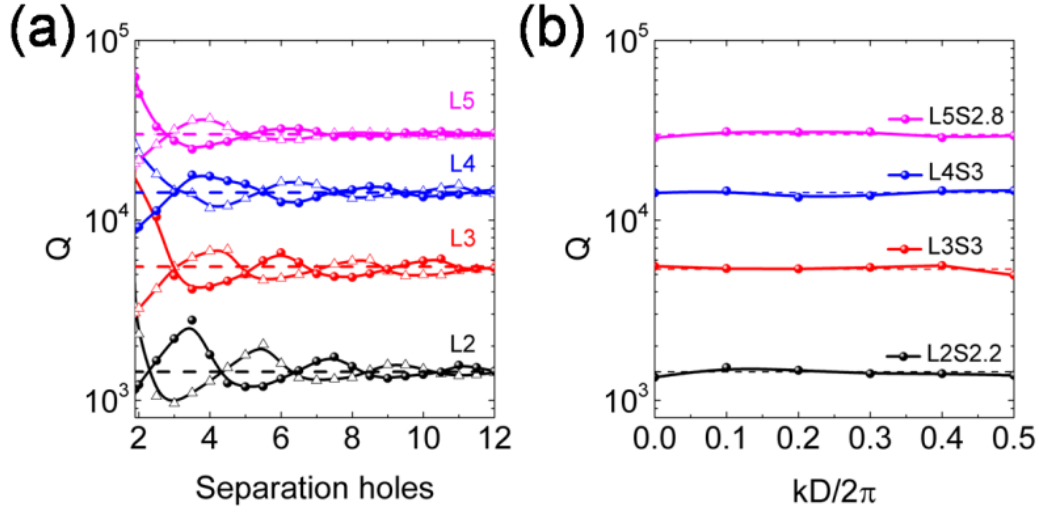


Figure 7-5 (a) Quality factor for CROWs based on different constituent cavities. Triangles indicate $Q(0)$; circles indicate $Q(k_{Bz})$. Dashed lines show Q for single cavity. Calculations are performed using the TBA method. (b) $Q(k)$ for CROWs designed with a number of separation holes equal to the first node in (a).

7.5 Summary

In conclusion, we have applied the tight-binding approximation (TBA) to predict the radiation loss of CROW waveguides in photonic crystal slabs. Our formulation shows that as the quality factor of the isolated cavity increases, the CROW quality factor tends to increase as well. This trend can be understood within the light-cone picture of radiation loss. For both isolated cavities and CROWs, the quality factor is related to the spatial power spectrum of the fields above the photonic crystal slab. As the magnitude of the components inside the light cone decrease, the quality factor increases. Within the TBA, the CROW power spectrum can be approximated by sampling the isolated cavity power spectrum in Fourier space. The loss of the CROW thus tends to follow that of the isolated cavity. We have verified the validity of the TBA by comparing predicted values of $Q(k)$ for L2 CROWs with those obtained by direct simulation.

Importantly, our method allows the calculation of the wave-vector dependent CROW quality factor for a range of cavity separations from a single simulation of the isolated cavity fields. As a result, it is possible to scan various CROW configurations with minimal computational power. In particular, we demonstrate that it is possible to design waveguides with low, flat losses across the entire Brillouin zone, even at small intercavity separations.

We expect our results to be useful for a range of applications. For slow- and stopped-light applications, the fidelity of signal transmission at the end of a delay line depends on achieving low, flat loss across the signal bandwidth. In coupled-cavity lasers, the ability to tailor the $Q(k)$ loss profile could provide a useful method to control the effects of mode competition and tune the directional output of the laser. Lastly, in the context of light-assisted self assembly above photonic-crystal slabs [24, 25], our method may facilitate the design of large-area, coupled-cavity modes with high quality factor that nevertheless couple to normally-incident radiation.

7.6 Chapter References

- [1]. A. Yariv, Y. Xu, R. K. Lee, and A. Scherer, "Coupled-resonator optical waveguide: a proposal and analysis," Opt. Lett. **24**, 711-713 (1999).
- [2]. R. M. De La Rue, "Optical delays: Slower for longer," Nat Photon **2**, 715-716 (2008).
- [3]. N. Stefanou, and A. Modinos, "Impurity bands in photonic insulators," Physical Review B **57**, 12127-12133 (1998).
- [4]. M. F. Yanik, and S. Fan, "Stopping light all optically," Physical Review Letters **92**, 083901 (2004).

- [5]. S. Sandhu, M. L. Povinelli, M. F. Yanik, and S. Fan, "Dynamically tuned coupled-resonator delay lines can be nearly dispersion free," *Opt. Lett.* **31**, 1985-1987 (2006).
- [6]. J. K. Poon, L. Zhu, G. A. DeRose, and A. Yariv, "Transmission and group delay of microring coupled-resonator optical waveguides," *Opt. Lett.* **31**, 456-458 (2006).
- [7]. F. Morichetti, A. Melloni, A. Breda, A. Canciamilla, C. Ferrari, and M. Martinelli, "A reconfigurable architecture for continuously variable optical slow-wave delay lines," *Opt. Express* **15**, 17273-17282 (2007).
- [8]. F. Xia, L. Sekaric, and Y. Vlasov, "Ultracompact optical buffers on a silicon chip," *Nat Photon* **1**, 65-71 (2007).
- [9]. S. Olivier, C. Smith, M. Rattier, H. Benisty, C. Weisbuch, T. Krauss, R. Houdré, and U. Oesterl, "Miniband transmission in a photonic crystal coupled-resonator optical waveguide," *Opt. Lett.* **26**, 1019-1021 (2001).
- [10]. E. Ozbay, M. Bayindir, I. Bulu, and E. Cubukcu, "Investigation of localized coupled-cavity modes in two-dimensional photonic bandgap structures," *Quantum Electronics, IEEE Journal of* **38**, 837-843 (2002).
- [11]. T. J. Karle, D. H. Brown, R. Wilson, M. Steer, and T. E. Krauss, "Planar photonic crystal coupled cavity waveguides," *Selected Topics in Quantum Electronics, IEEE Journal of* **8**, 909-918 (2002).
- [12]. P. Sanchis, J. Marti, W. Bogaerts, P. Dumon, D. V. Thourhout, and R. Baets, "Experimental results on adiabatic coupling into SOI photonic crystal coupled-cavity waveguides," *Photonics Technology Letters, IEEE* **17**, 1199-1201 (2005).
- [13]. D. O'Brien, M. D. Settle, T. Karle, A. Michaeli, M. Salib, and T. F. Krauss, "Coupled photonic crystal heterostructure nanocavities," *Opt. Express* **15**, 1228-1233 (2007).
- [14]. J. Jágorská, N. Le Thomas, V. Zabelin, R. Houdré, W. Bogaerts, P. Dumon, and R. Baets, "Experimental observation of slow mode dispersion in photonic crystal coupled-cavity waveguides," *Opt. Lett.* **34**, 359-361 (2009).
- [15]. J. Jágorská, H. Zhang, N. Le Thomas, and R. Houdré, "Radiation loss of photonic crystal coupled-cavity waveguides," *Applied Physics Letters* **95**, 111105-111103 (2009).

- [16]. N. Matsuda, T. Kato, K.-i. Harada, H. Takesue, E. Kuramochi, H. Taniyama, and M. Notomi, "Slow light enhanced optical nonlinearity in a silicon photonic crystal coupled-resonator optical waveguide," *Opt. Express* **19**, 19861-19874.
- [17]. H.-C. Liu, and A. Yariv, "Designing coupled-resonator optical waveguides based on high-Q tapered grating-defect resonators," *Opt. Express* **20**, 9249-9263.
- [18]. Y. Kawaguchi, K. Saitoh, and M. Koshiba, "Analysis of leakage losses in one-dimensional photonic crystal coupled resonator optical waveguide using 3-D finite element method," *Lightwave Technology, Journal of* **28**, 2977-2983.
- [19]. A. Martínez, J. García, P. Sanchis, F. Cuesta-Soto, J. Blasco, and J. Martí, "Intrinsic losses of coupled-cavity waveguides in planar-photonic crystals," *Opt. Lett.* **32**, 635-637 (2007).
- [20]. M. L. Povinelli, and S. Fan, "Radiation loss of coupled-resonator waveguides in photonic-crystal slabs," *Applied Physics Letters* **89**, 191114-191113 (2006).
- [21]. D. P. Fussell, and M. M. Dignam, "Engineering the quality factors of coupled-cavity modes in photonic crystal slabs," *Applied Physics Letters* **90**, 183121-183123 (2007).
- [22]. T. Tanabe, M. Notomi, E. Kuramochi, A. Shinya, and H. Taniyama, "Trapping and delaying photons for one nanosecond in an ultrasmall high-Q photonic-crystal nanocavity," *Nat Photon* **1**, 49-52 (2007).
- [23]. J. Vuckovic, M. Loncar, H. Mabuchi, and A. Scherer, "Optimization of the Q factor in photonic crystal microcavities," *Quantum Electronics, IEEE Journal of* **38**, 850-856 (2002).
- [24]. C. A. Mejia, A. Dutt, and M. L. Povinelli, "Light-assisted templated self assembly using photonic crystal slabs," *Opt. Express* **19**, 11422-11428 (2011).
- [25]. J. Ma, L. J. Martínez, and M. L. Povinelli, "Optical trapping via guided resonance modes in a Slot-Suzuki-phase photonic crystal lattice," *Opt. Express* **20**, 6816-6824 (2012).
- [26]. L. C. Andreani, and D. Gerace, "Photonic-crystal slabs with a triangular lattice of triangular holes investigated using a guided-mode expansion method," *Physical Review B* **73**, 235114 (2006).

- [27]. Y. Xu, R. K. Lee, and A. Yariv, "Propagation and second-harmonic generation of electromagnetic waves in a coupled-resonator optical waveguide," *J. Opt. Soc. Am. B* **17**, 387-400 (2000).
- [28]. A. Taflove, *Computational Electrodynamics: the Finite-Difference Time-Domain Method* (Artech House, Boston, 1995).
- [29]. A. R. A. Chalcraft, S. Lam, D. O'Brien, T. F. Krauss, M. Sahin, D. Szymanski, D. Sanvitto, R. Oulton, M. S. Skolnick, A. M. Fox, D. M. Whittaker, H. Y. Liu, and M. Hopkinson, "Mode structure of the L3 photonic crystal cavity," *Applied Physics Letters* **90**, 241117-241113 (2007).

Bibliography

- A. Ashkin, "History of optical trapping and manipulation of small-neutral particle, atoms, and molecules," *Selected Topics in Quantum Electronics, IEEE Journal of* 6, 841-856 (2000).
- K. C. Neuman, and S. M. Block, "Optical trapping," *Rev. Sci. Instrum.* 75, 2787-2809 (2004).
- M. L. Povinelli, M. Loncar, M. Ibanescu, E. J. Smythe, S. G. Johnson, F. Capasso, and J. D. Joannopoulos, "Evanescent-wave bonding between optical waveguides," *Opt. Lett.* 30, 3042-3044 (2005).
- S. Noda, K. Tomoda, N. Yamamoto, and A. Chutinan, "Full Three-Dimensional Photonic Bandgap Crystals at Near-Infrared Wavelengths," *Science* 289, 604-606 (2000).
- V. R. Almeida, C. A. Barrios, R. R. Panepucci, and M. Lipson, "All-optical control of light on a silicon chip," *Nature* 431, 1081-1084 (2004).
- R. A. Soref, "Silicon-based optoelectronics," *Proc. IEEE* 81, 1687-1706 (1993).
- L. Pavesi, and D. J. Lockwood, *Silicon Photonics* (Springer, Berlin ; New York, 2004).
- M. Haurylau, C. Guoqing, C. Hui, Z. Jidong, N. A. Nelson, D. H. Albonesi, E. G. Friedman, and P. M. Fauchet, "On-Chip Optical Interconnect Roadmap: Challenges and Critical Directions," *Selected Topics in Quantum Electronics, IEEE Journal of* 12, 1699-1705 (2006).
- A. Faraon, A. Majumdar, D. Englund, E. Kim, M. Bajcsy, and J. Vuckovic, "Integrated quantum optical networks based on quantum dots and photonic crystals," *New J. Phys.* 13, 13.
- W. H. P. Pernice, M. Li, D. Garcia-Sanchez, and H. X. Tang, "Analysis of short range forces in opto-mechanical devices with a nanogap," *Opt. Express* 18, 12615-12621.
- M. Li, W. H. Pernice, and H. X. Tang, "Ultrahigh-frequency nano-optomechanical resonators in slot waveguide ring cavities," *Appl. Phys. Lett.* 97, 183110.
- A. Dorsel, J. D. McCullen, P. Meystre, E. Vignes, and H. Walther, "Optical Bistability and Mirror Confinement Induced by Radiation Pressure," *Phys. Rev. Lett.* 51, 1550 (1983).
- W. H. P. Pernice, M. Li, and H. X. Tang, "Theoretical investigation of the transverse optical force between a silicon nanowire waveguide and a substrate," *Opt. Express* 17, 1806-1816 (2009).
- M. Li, W. H. P. Pernice, C. Xiong, T. Baehr-Jones, M. Hochberg, and H. X. Tang, "Harnessing optical forces in integrated photonic circuits," *Nature* 456, 480-484 (2008).

J. S. Foresi, P. R. Villeneuve, J. Ferrera, E. R. Thoen, G. Steinmeyer, S. Fan, J. D. Joannopoulos, L. C. Kimerling, H. I. Smith, and E. P. Ippen, "Photonic-bandgap microcavities in optical waveguides," *Nature* 390, 143-145 (1997).

Y. Akahane, T. Asano, B. S. Song, and S. Noda, "High-Q photonic nanocavity in a two-dimensional photonic crystal," *Nature* 425, 944-947 (2003).

B. S. Song, S. Noda, T. Asano, and Y. Akahane, "Ultra-high-Q photonic double-heterostructure nanocavity," *Nat. Mater.* 4, 207-210 (2005).

H. Y. Ryu, M. Notomi, and Y. H. Lee, "High-quality-factor and small-mode-volume hexapole modes in photonic-crystal-slab nanocavities," *Applied Physics Letters* 83, 4294-4296 (2003).

J. Chan, M. Eichenfield, R. Camacho, and O. Painter, "Optical and mechanical design of a "zipper" photonic crystal optomechanical cavity," *Opt. Express* 17, 3802-3817 (2009).

M. Eichenfield, R. Camacho, J. Chan, K. J. Vahala, and O. Painter, "A picogram- and nanometre-scale photonic-crystal optomechanical cavity," *Nature* 459, 550-555 (2009).

M. Eichenfield, J. Chan, R. M. Camacho, K. J. Vahala, and O. Painter, "Optomechanical crystals," *Nature* 462, 78-82 (2009).

H. Taniyama, M. Notomi, E. Kuramochi, T. Yamamoto, Y. Yoshikawa, Y. Torii, and T. Kuga, "Strong radiation force induced in two-dimensional photonic crystal slab cavities," *Physical Review B* 78, 165129 (2008).

M. Notomi, H. Taniyama, S. Mitsugi, and E. Kuramochi, "Optomechanical wavelength and energy conversion in high-Q double-layer cavities of photonic crystal slabs," *Phys. Rev. Lett.* 97, 4 (2006).

S. Fan, and M. L. Povinelli, "Stopping Light via Dynamic Tuning of Coupled Resonators," in *Slow Light: Science and Applications*(CRC Press, Boca Raton, 2009).

S. Fan, S. Sandhu, C. Otey, and M. Povinelli, "Slow and Stopped Light in Coupled Resonator Systems," in *Photonic Microresonator Research and Applications*(Springer Berlin / Heidelberg), pp. 165-180.

S. Fan, and J. D. Joannopoulos, "Analysis of guided resonances in photonic crystal slabs," *Physical Review B* 65, 235112 (2002).

V. Liu, M. Povinelli, and S. H. Fan, "Resonance-enhanced optical forces between coupled photonic crystal slabs," *Optics Express* 17, 21897-21909 (2009).

Y. G. Roh, T. Tanabe, A. Shinya, H. Taniyama, E. Kuramochi, S. Matsuo, T. Sato, and M. Notomi, "Strong optomechanical interaction in a bilayer photonic crystal," *Physical Review B* 81, 4 (2010).

J. Rosenberg, Q. Lin, and O. Painter, "Static and dynamic wavelength routing via the gradient optical force," *Nat Photon* 3, 478-483 (2009).

A. W. Rodriguez, A. P. McCauley, P.-C. Hui, D. Woolf, E. Iwase, F. Capasso, M. Loncar, and S. G. Johnson, "Bonding, antibonding and tunable optical forces in asymmetric membranes," *Opt. Express* 19, 2225-2241 (2011).

A. W. Rodriguez, D. Woolf, P. C. Hui, E. Iwase, A. P. McCauley, F. Capasso, M. Loncar, and S. G. Johnson, "Designing evanescent optical interactions to control the expression of Casimir forces in optomechanical structures," *Applied Physics Letters* 98, 3.

S. A. Maier, *Plasmonics: Fundamentals and Applications* (Springer, New York, 2007).

D. Woolf, M. Loncar, and F. Capasso, "The forces from coupled surface plasmon polaritons in planar waveguides," *Optics Express* 17, 19996-20011 (2009).

X. D. Yang, Y. M. Liu, R. F. Oulton, X. B. Yin, and X. A. Zhang, "Optical Forces in Hybrid Plasmonic Waveguides," *Nano Lett.* 11, 321-328.

C. G. Huang, and L. Zhu, "Enhanced optical forces in 2D hybrid and plasmonic waveguides," *Optics Letters* 35, 1563-1565.

B. E. A. Saleh, and M. C. Teich, *Fundamentals of Photonics* (1991).

K. Y. Fong, W. H. P. Pernice, M. Li, and H. X. Tang, "Tunable optical coupler controlled by optical gradient forces," *Opt. Express* 19, 15098-15108.

M. Eichenfield, C. P. Michael, R. Perahia, and O. Painter, "Actuation of micro-optomechanical systems via cavity-enhanced optical dipole forces," *Nat Photon* 1, 416-422 (2007).

G. S. Wiederhecker, S. Manipatruni, S. Lee, and M. Lipson, "Broadband tuning of optomechanical cavities," *Opt. Express* 19, 2782-2790.

P. T. Rakich, M. A. Popovic, M. Soljagic, and E. P. Ippen, "Trapping, corralling and spectral bonding of optical resonances through optically induced potentials," *Nat Photon* 1, 658-665 (2007).

M. A. Popovic, and P. T. Rakich, "Optonomechanical self-adaptive photonic devices based on light forces: a path to robust high-index-contrast nanophotonic circuits," in *Optoelectronic Integrated Circuits XI*, L. A. Eldada, and E. H. Lee, eds. (SPIE-Int Soc Optical Engineering, Bellingham, 2009).

A. H. Safavi-Naeini, T. P. M. Alegre, J. Chan, M. Eichenfield, M. Winger, Q. Lin, J. T. Hill, D. E. Chang, and O. Painter, "Electromagnetically induced transparency and slow light with optomechanics," *Nature* 472, 69-73.

- D. E. Chang, A. H. Safavi-Naeini, M. Hafezi, and O. Painter, "Slowing and stopping light using an optomechanical crystal array," *New J. Phys.* 13, 26.
- S. E. Harris, "Electromagnetically induced transparency," *Phys. Today* 50, 36-42 (1997).
- M. F. Yanik, W. Suh, Z. Wang, and S. H. Fan, "Stopping light in a waveguide with an all-optical analog of electromagnetically induced transparency," *Phys. Rev. Lett.* 93, 4 (2004).
- M. F. Yanik, and S. H. Fan, "Stopping and storing light coherently," *Phys. Rev. A* 71, 10 (2005).
- S. H. Fan, M. F. Yanik, Z. Wang, S. Sandhu, and M. L. Povinelli, "Advances in theory of photonic crystals," *J. Lightwave Technol.* 24, 4493-4501 (2006).
- T. P. M. Alegre, R. Perahia, and O. Painter, "Optomechanical zipper cavity lasers: theoretical analysis of tuning range and stability," *Optics Express* 18, 7872-7885.
- W. H. P. Pernice, M. Li, and H. X. Tang, "A mechanical Kerr effect in deformable photonic media," *Applied Physics Letters* 95, 123507-123503 (2009).
- A. Ashkin, J. M. Dziedzic, J. E. Bjorkholm, and S. Chu, "Observation of a single-beam gradient force optical trap for dielectric particles," *Opt. Lett.* 11, 288-290 (1986).
- A. Ashkin, J. M. Dziedzic, and T. Yamane, "OPTICAL TRAPPING AND MANIPULATION OF SINGLE CELLS USING INFRARED-LASER BEAMS," *Nature* 330, 769-771 (1987).
- A. Ashkin, "Optical trapping and manipulation of neutral particles using lasers," *Proc. Natl. Acad. Sci. U. S. A.* 94, 4853-4860 (1997).
- S. Lin, J. Hu, L. Kimerling, and K. Crozier, "Design of nanoslotted photonic crystal waveguide cavities for single nanoparticle trapping and detection," *Opt. Lett.* 34, 3451-3453 (2009).
- K. Okamoto, and S. Kawata, "Radiation Force Exerted on Subwavelength Particles near a Nanoaperture," *Phys. Rev. Lett.* 83, 4534-4537 (1999).
- B. K. Wilson, T. Mentele, S. Bachar, E. Knouf, A. Bendoraite, M. Tewari, S. H. Pun, and L. Y. Lin, "Nanostructure-enhanced laser tweezers for efficient trapping and alignment of particles," *Opt. Express* 18, 16005-16013.
- M. Righini, A. S. Zelenina, C. Girard, and R. Quidant, "Parallel and selective trapping in a patterned plasmonic landscape," *Nat Phys* 3, 477-480 (2007).
- A. N. Grigorenko, N. W. Roberts, M. R. Dickinson, and Y. Zhang, "Nanometric optical tweezers based on nanostructured substrates," *Nat. Photonics* 2, 365-370 (2008).
- M. L. Juan, M. Righini, and R. Quidant, "Plasmon nano-optical tweezers," *Nat Photon* 5, 349-356 (2011).

- B. J. Roxworthy, K. D. Ko, A. Kumar, K. H. Fung, E. K. C. Chow, G. L. Liu, N. X. Fang, and K. C. Toussaint, "Application of Plasmonic Bowtie Nanoantenna Arrays for Optical Trapping, Stacking, and Sorting," *Nano Lett.* 12, 796-801 (2012).
- A. H. J. Yang, S. D. Moore, B. S. Schmidt, M. Klug, M. Lipson, and D. Erickson, "Optical manipulation of nanoparticles and biomolecules in sub-wavelength slot waveguides," *Nature* 457, 71-75 (2009).
- S. Lin, E. Schonbrun, and K. Crozier, "Optical Manipulation with Planar Silicon Microring Resonators," *Nano Lett.* 10, 2408-2411 (2010).
- S. Mandal, X. Serey, and D. Erickson, "Nanomanipulation Using Silicon Photonic Crystal Resonators," *Nano Lett.* 10, 99-104 (2010).
- Y. F. Chen, X. Serey, R. Sarkar, P. Chen, and D. Erickson, "Controlled Photonic Manipulation of Proteins and Other Nanomaterials," *Nano Lett.* 12, 1633-1637.
- C. Renaut, J. Dellinger, B. Cluzel, T. Honegger, D. Peyrade, E. Picard, F. de Fornel, and E. Hadji, "Assembly of microparticles by optical trapping with a photonic crystal nanocavity," *Applied Physics Letters* 100, 101103-101103 (2012).
- C. A. Mejia, A. Dutt, and M. L. Povinelli, "Light-assisted templated self assembly using photonic crystal slabs," *Opt. Express* 19, 11422-11428 (2011).
- E. Jaquay, L. J. Martinez, C. A. Mejia, and M. L. Povinelli, "Light-Assisted, Templated Self-Assembly Using a Photonic-Crystal Slab," *Nano Lett.* 13, 2290-2294 (2013).
- M. M. Burns, J.-M. Fournier, and J. A. Golovchenko, "Optical Matter: Crystallization and Binding in Intense Optical Fields," *Science* 249, 749-754 (1990).
- P. Korda, G. C. Spalding, E. R. Dufresne, and D. G. Grier, "Nanofabrication with holographic optical tweezers," *Rev. Sci. Instrum.* 73, 1956-1957 (2002).
- J. D. Jackson, *Classical Electrodynamics* (Wiley, New York, 1999).
- M. L. Povinelli, M. Ibanescu, S. G. Johnson, and J. D. Joannopoulos, "Slow-light enhancement of radiation pressure in an omnidirectional-reflector waveguide," *Applied Physics Letters* 85, 1466-1468 (2004).
- A. Mizrahi, and L. Schachter, "Mirror manipulation by attractive and repulsive forces of guided waves," *Opt. Express* 13, 9804-9811 (2005).
- J. Ng, C. T. Chan, P. Sheng, and Z. Lin, "Strong optical force induced by morphology-dependent resonances," *Opt. Lett.* 30, 1956-1958 (2005).
- M. I. Antonoyiannakis, and J. B. Pendry, "Electromagnetic forces in photonic crystals," *Physical Review B* 60, 2363 (1999).

- M. L. Povinelli, S. G. Johnson, M. Loncar, M. Ibanescu, E. Smythe, F. Capasso, and J. D. Joannopoulos, "High-Q enhancement of attractive and repulsive optical forces between coupled whispering-gallery- mode resonators," *Opt. Express* 13, 8286-8295 (2005).
- P. T. Rakich, M. A. Popovic, and Z. Wang, "General Treatment of Optical Forces and Potentials in Mechanically Variable Photonic Systems," *Optics Express* 17, 18116-18135 (2009).
- H. A. Haus, and W. P. Huang, "Coupled-mode theory," *Proc. IEEE* 79, 1505-1518 (1991).
- D. Van Thourhout, and J. Roels, "Optomechanical device actuation through the optical gradient force," *Nat Photon* 4, 211-217 (2010).
- F. Riboli, A. Recati, M. Antezza, and I. Carusotto, "Radiation induced force between two planar waveguides," *The European Physical Journal D - Atomic, Molecular, Optical and Plasma Physics* 46, 157-164 (2008).
- A. Mizrahi, and L. Schachter, "Electromagnetic forces on the dielectric layers of the planar optical Bragg acceleration structure," *Physical Review E* 74, 036504 (2006).
- A. Mizrahi, and L. Schachter, "Two-slab all-optical spring," *Opt. Lett.* 32, 692-694 (2007).
- M. Li, W. H. P. Pernice, and H. X. Tang, "Tunable bipolar optical interactions between guided lightwaves," *Nat Photon* 3, 464-468 (2009).
- J. Roels, I. De Vlaminck, L. Lagae, B. Maes, D. Van Thourhout, and R. Baets, "Tunable optical forces between nanophotonic waveguides," *Nat Nano* 4, 510-513 (2009).
- G. S. Wiederhecker, L. Chen, A. Gondarenko, and M. Lipson, "Controlling photonic structures using optical forces," *Nature* 462, 633-636 (2009).
- J. Ma, and M. L. Povinelli, "Large tuning of birefringence in two strip silicon waveguides via optomechanical motion," *Opt. Express* 17, 17818-17828 (2009).
- J. Chan, M. Eichenfield, R. Camacho, and O. Painter, "Optical and mechanical design of a "zipper" photonic crystal optomechanical cavity," *Opt. Express* 17, 3802-3817 (2009).
- J. D. Joannopoulos, R. D. Meade, and J. N. Winn, *Photonic crystals : molding the flow of light* (Princeton University Press, Princeton, N.J., 1995).
- S. G. Johnson, and J. D. Joannopoulos, "Block-iterative frequency-domain methods for Maxwell's equations in a planewave basis," *Opt. Express* 8, 173-190 (2001).
- S. Timoshenko, *Theory of elasticity* (McGraw-Hill, New York, London,, 1934).
- A. R. Day, K. A. Snyder, E. J. Garboczi, and M. F. Thorpe, "The elastic moduli of a sheet containing circular holes," *Journal of the Mechanics and Physics of Solids* 40, 1031-1051 (1992).

P. T. Rakich, M. A. Popovic, and Z. Wang, "General treatment of optical forces and potentials in mechanically variable photonic systems," *Opt. Express* 17, 18116-18135 (2009).

J. Ma, and M. L. Povinelli, "Effect of periodicity on optical forces between a one-dimensional periodic photonic crystal waveguide and an underlying substrate," *Applied Physics Letters* 97, 151102-151103 (2010).

P. Meystre, E. M. Wright, J. D. McCullen, and E. Vignes, "Theory of radiation-pressure-driven interferometers," *J. Opt. Soc. Am. B* 2, 1830-1840 (1985).

M. Soljacic, C. Luo, J. D. Joannopoulos, and S. Fan, "Nonlinear photonic crystal microdevices for optical integration," *Opt. Lett.* 28, 637-639 (2003).

M. L. Povinelli, "Microphotonics - Under pressure," *Nat. Photonics* 1, 370-371 (2007).

S. H. Yang, M. L. Cooper, P. R. Bandaru, and S. Mookherjea, "Giant birefringence in multi-slotted silicon nanophotonic waveguides," *Optics Express* 16, 8306-8316 (2008).

C. Kerbage, P. Steinvurzel, P. Reyes, P. S. Westbrook, R. S. Windeler, A. Hale, and B. J. Eggleton, "Highly tunable birefringent microstructured optical fiber," *Optics Letters* 27, 842-844 (2002).

C. Kerbage, and B. J. Eggleton, "Numerical analysis and experimental design of tunable birefringence in microstructured optical fiber," *Optics Express* 10, 246-255 (2002).

T. Woliński, A. Czapla, S. Ertman, M. Tefelska, A. Domański, E. Nowinowski-Kruszelnicki, and R. Dąbrowski, "Tunable highly birefringent solid-core photonic liquid crystal fibers," *Optical and Quantum Electronics* 39, 1021-1032 (2007).

K. K. Tsia, S. Fathpour, and B. Jalali, "Electrical tuning of birefringence in silicon waveguides," *Applied Physics Letters* 92, 061109-061103 (2008).

M. Kumar, T. Sakaguchi, and F. Koyama, "Wide tunability and ultralarge birefringence with 3D hollow waveguide Bragg reflector," *Opt. Lett.* 34, 1252-1254 (2009).

V. R. Almeida, Q. Xu, C. A. Barrios, and M. Lipson, "Guiding and confining light in void nanostructure," *Opt. Lett.* 29, 1209-1211 (2004).

Q. Xu, V. R. Almeida, R. R. Panepucci, and M. Lipson, "Experimental demonstration of guiding and confining light in nanometer-size low-refractive-index material," *Opt. Lett.* 29, 1626-1628 (2004).

V. A. Parsegian, *Van der Waals forces : a handbook for biologists, chemists, engineers, and physicists* (Cambridge University Press, New York, 2006).

A. H. Rose, N. Feat, and S. M. Etzel, "Wavelength and Temperature Performance of Polarization-Transforming Fiber," *Appl. Opt.* 42, 6897-6904 (2003).

M. R. Watts, and H. A. Haus, "Integrated mode-evolution-based polarization rotators," *Opt. Lett.* 30, 138-140 (2005).

Y. Shani, R. Alferness, T. Koch, U. Koren, M. Oron, B. I. Miller, and M. G. Young, "Polarization rotation in asymmetric periodic loaded rib waveguides," *Applied Physics Letters* 59, 1278-1280 (1991).

J. J. G. M. Van der Tol, F. Hakimzadeh, J. W. Pedersen, D. Li, and H. Van Brug, "A new short and low-loss passive polarization converter on InP," *Photonics Technology Letters, IEEE* 7, 32-34 (1995).

K. Bayat, S. K. Chaudhuri, and S. Safavi-Naeini, "Ultra-compact photonic crystal based polarization rotator," *Opt. Express* 17, 7145-7158 (2009).

C. Fietz, and G. Shvets, "Nonlinear polarization conversion using microring resonators," *Opt. Lett.* 32, 1683-1685 (2007).

R. J. Manning, A. Antonopoulos, R. Le Roux, and A. E. Kelly, "Experimental measurement of nonlinear polarisation rotation in semiconductor optical amplifiers," *Electronics Letters* 37, 229-231 (2001).

H. Soto, D. Erasme, and G. Guekos, "Cross-polarization modulation in semiconductor optical amplifiers," *Photonics Technology Letters, IEEE* 11, 970-972 (1999).

R. W. Boyd, *Nonlinear optics* (Academic Press, Amsterdam ; Boston, 2008).

C. Fietz, and G. Shvets, "Simultaneous fast and slow light in microring resonators," *Opt. Lett.* 32, 3480-3482 (2007).

F. Morichetti, A. Melloni, A. Breda, A. Canciamilla, C. Ferrari, and M. Martinelli, "A reconfigurable architecture for continuously variable optical slow-wave delay lines," *Opt. Express* 15, 17273-17282 (2007).

F. Morichetti, C. Ferrari, A. Melloni, and M. Martinelli, "Polarization-Selective Tunable Delay in Coupled-Resonator Optical Delay-Lines," in *Integrated Photonics and Nanophotonics Research and Applications*(Optical Society of America, 2008), p. IWG1.

A. Ashkin, "Acceleration and Trapping of Particles by Radiation Pressure," *Phys. Rev. Lett.* 24, 156-159 (1970).

D. G. Grier, "A revolution in optical manipulation," *Nature* 424, 810-816 (2003).

J. Guck, R. Ananthakrishnan, H. Mahmood, T. J. Moon, C. C. Cunningham, and J. Kas, "The Optical Stretcher: A Novel Laser Tool to Micromanipulate Cells," *Biophysical Journal* 81, 767-784 (2001).

D. Erickson, X. Serey, Y.-F. Chen, and S. Mandal, "Nanomanipulation using near field photonics," *Lab on a Chip* 11, 995-1009.

M. Barth, and O. Benson, "Manipulation of dielectric particles using photonic crystal cavities," *Applied Physics Letters* 89, 253114-253113 (2006).

A. Rahmani, and P. C. Chaumet, "Optical trapping near a photonic crystal," *Opt. Express* 14, 6353-6358 (2006).

X. Serey, S. Mandal, and D. Erickson, "Comparison of silicon photonic crystal resonator designs for optical trapping of nanomaterials," *Nanotechnology* 21, 305202.

A. R. Alija, L. J. Martinez, P. A. Postigo, J. Sanchez-Dehesa, M. Galli, A. Politi, M. Patrini, L. C. Andreani, C. Seassal, and P. Viktorovitch, "Theoretical and experimental study of the Suzuki-phase photonic crystal lattice by angle-resolved photoluminescence spectroscopy," *Opt. Express* 15, 704-713 (2007).

C. Monat, C. Seassal, X. Letartre, P. Regreny, M. Gendry, P. R. Romeo, P. Viktorovitch, M. L. V. d'Yerville, D. Cassagne, J. P. Albert, E. Jalaguier, S. Pocas, and B. Aspar, "Two-dimensional hexagonal-shaped microcavities formed in a two-dimensional photonic crystal on an InP membrane," *Journal of Applied Physics* 93, 23-31 (2003).

M. Li, X. Hu, Z. Ye, K.-M. Ho, J. Cao, and M. Miyawaki, "Higher-order incidence transfer matrix method used in three-dimensional photonic crystal coupled-resonator array simulation," *Opt. Lett.* 31, 3498-3500 (2006).

S. Fan, W. Suh, and J. D. Joannopoulos, "Temporal coupled-mode theory for the Fano resonance in optical resonators," *J. Opt. Soc. Am. A* 20, 569-572 (2003).

T. Ochiai, and K. Sakoda, "Dispersion relation and optical transmittance of a hexagonal photonic crystal slab," *Physical Review B* 63, 125107 (2001).

M. Galli, M. Agio, L. C. Andreani, M. Belotti, G. Guizzetti, F. Marabelli, M. Patrini, P. Bettotti, L. Dal Negro, Z. Gaburro, L. Pavesi, A. Lui, and P. Bellutti, "Spectroscopy of photonic bands in macroporous silicon photonic crystals," *Physical Review B* 65, 113111 (2002).

A. Taflove, *Advances in computational electrodynamics : the finite-difference time-domain method* (Artech House, Boston, 1998).

L. J. Martinez, A. R. Alija, P. A. Postigo, J. F. Galisteo-Lopez, M. Galli, L. C. Andreani, C. Seassal, and P. Viktorovitch, "Effect of implementation of a Bragg reflector in the photonic band structure of the Suzuki-phase photonic crystal lattice," *Opt. Express* 16, 8509-8518 (2008).

X. Letartre, J. Mouette, J. L. Leclercq, P. R. Romeo, C. Seassal, and P. Viktorovitch, "Switching Devices With Spatial and Spectral Resolution Combining Photonic Crystal and MOEMS Structures," *J. Lightwave Technol.* 21, 1691 (2003).

- L. J. Martinez, B. Alen, I. Prieto, J. F. Galisteo-Lopez, M. Galli, L. C. Andreani, C. Seassal, P. Viktorovitch, and P. A. Postigo, "Two-dimensional surface emitting photonic crystal laser with hybrid triangular-graphite structure," *Opt. Express* 17, 15043-15051 (2009).
- V. Almeida, Q. Xu, C. Barrios, and M. Lipson, "Guiding and confining light in void nanostructure," *Optics Letters* 29, 1209-1211 (2004).
- T. Yamamoto, M. Notomi, H. Taniyama, E. Kuramochi, Y. Yoshikawa, Y. Torii, and T. Kuga, "Design of a high-Q air-slot cavity based on a width-modulated line-defect in a photonic crystal slab," *Opt. Express* 16, 13809-13817 (2008).
- M. El Beheiry, V. Liu, S. Fan, and O. Levi, "Sensitivity enhancement in photonic crystal slab biosensors," *Opt. Express* 18, 22702-22714.
- S. Kita, S. Hachuda, K. Nozaki, and T. Baba, "Nanoslot laser," *Applied Physics Letters* 97, 161108-161103.
- S. Kita, S. Hachuda, S. Otsuka, T. Endo, Y. Imai, Y. Nishijima, H. Misawa, and T. Baba, "Super-sensitivity in label-free protein sensing using a nanoslot nanolaser," *Opt. Express* 19, 17683-17690.
- B. B. Bakir, C. Seassal, X. Letartre, P. Viktorovitch, M. Zussy, L. Di Cioccio, and J. M. Fedeli, "Surface-emitting microlaser combining two-dimensional photonic crystal membrane and vertical Bragg mirror," *Applied Physics Letters* 88, 081113-081113 (2006).
- L. Ferrier, P. Rojo-Romeo, E. Drouard, X. Letatre, and P. Viktorovitch, "Slow Bloch mode confinement in 2D photonic crystals for surface operating devices," *Opt. Express* 16, 3136-3145 (2008).
- C. Monat, C. Seassal, X. Letartre, P. Regreny, P. Rojo-Romeo, P. Viktorovitch, M. L. V. d'Yerville, D. Cassagne, J. P. Albert, E. Jalaguier, S. Pocas, and B. Aspar, "InP-based two-dimensional photonic crystal on silicon: In-plane Bloch mode laser," *Applied Physics Letters* 81, 5102-5104 (2002).
- H.-Y. Ryu, S.-H. Kwon, L. Yong-jae, Y.-H. Lee, and J.-S. Kim, "Very-low-threshold photonic band-edge lasers from free-standing triangular photonic crystal slabs," *Applied Physics Letters* 80, 3476-3478 (2002).
- J. Mouette, C. Seassal, X. Letartre, P. Rojo-Romeo, J. L. Leclercq, P. Regreny, P. Viktorovitch, E. Jalaguier, R. Perreau, and H. Moriceau, "Very low threshold vertical emitting laser operation in InP graphite photonic crystal slab on silicon," *Electronics Letters* 39, 526-528 (2003).
- N. Chauvin, P. Nedel, C. Seassal, B. Ben Bakir, X. Letartre, M. Gendry, A. Fiore, and P. Viktorovitch, "Control of the spontaneous emission from a single quantum dash using a slow-light mode in a two-dimensional photonic crystal on a Bragg reflector," *Physical Review B* 80, 045315 (2009).

- M. Huang, A. A. Yanik, T.-Y. Chang, and H. Altug, "Sub-wavelength nanofluidics in photonic crystal sensors," *Opt. Express* 17, 24224-24233 (2009).
- D. Cassagne, C. Jouanin, and D. Bertho, "Photonic band gaps in a two-dimensional graphite structure," *Physical Review B* 52, R2217-R2220 (1995).
- G. Alagappan, X. W. Sun, and H. D. Sun, "Symmetries of the eigenstates in an anisotropic photonic crystal," *Physical Review B* 77, 195117 (2008).
- L. C. Andreani, and D. Gerace, "Photonic-crystal slabs with a triangular lattice of triangular holes investigated using a guided-mode expansion method," *Physical Review B* 73, 235114 (2006).
- X. Letartre, C. Monat, C. Seassal, and P. Viktorovitch, "Analytical modeling and an experimental investigation of two-dimensional photonic crystal microlasers: defect state (microcavity) versus band-edge state (distributed feedback) structures," *J. Opt. Soc. Am. B* 22, 2581-2595 (2005).
- J. T. Robinson, C. Manolatou, L. Chen, and M. Lipson, "Ultrasmall Mode Volumes in Dielectric Optical Microcavities," *Physical Review Letters* 95, 143901 (2005).
- L. J. Martinez Rodriguez, E. Jaquay, J. Ma, and M. L. Povinelli, "Fabrication and optical characterization of high-Q guided mode resonances in a graphite-lattice photonic crystal slab," in *CLEO: Science and Innovations*(Optical Society of America), p. JW4A.78.
- M. Skorobogatiy, G. Begin, and A. Talneau, "Statistical analysis of geometrical imperfections from the images of 2D photonic crystals," *Opt. Express* 13, 2487-2502 (2005).
- D. M. Beggs, L. O'Faolain, and T. F. Krauss, "Accurate determination of the functional hole size in photonic crystal slabs using optical methods," *Photonics and Nanostructures - Fundamentals and Applications* 6, 213-218 (2008).
- A. Yariv, Y. Xu, R. K. Lee, and A. Scherer, "Coupled-resonator optical waveguide: a proposal and analysis," *Opt. Lett.* 24, 711-713 (1999).
- R. M. De La Rue, "Optical delays: Slower for longer," *Nat Photon* 2, 715-716 (2008).
- N. Stefanou, and A. Modinos, "Impurity bands in photonic insulators," *Physical Review B* 57, 12127-12133 (1998).
- M. F. Yanik, and S. Fan, "Stopping light all optically," *Physical Review Letters* 92, 083901 (2004).
- S. Sandhu, M. L. Povinelli, M. F. Yanik, and S. Fan, "Dynamically tuned coupled-resonator delay lines can be nearly dispersion free," *Opt. Lett.* 31, 1985-1987 (2006).

- J. K. Poon, L. Zhu, G. A. DeRose, and A. Yariv, "Transmission and group delay of microring coupled-resonator optical waveguides," *Opt. Lett.* 31, 456-458 (2006).
- F. Xia, L. Sekaric, and Y. Vlasov, "Ultracompact optical buffers on a silicon chip," *Nat Photon* 1, 65-71 (2007).
- S. Olivier, C. Smith, M. Rattier, H. Benisty, C. Weisbuch, T. Krauss, R. Houdré, and U. Oesterl, "Miniband transmission in a photonic crystal coupled-resonator optical waveguide," *Opt. Lett.* 26, 1019-1021 (2001).
- E. Ozbay, M. Bayindir, I. Bulu, and E. Cubukcu, "Investigation of localized coupled-cavity modes in two-dimensional photonic bandgap structures," *Quantum Electronics, IEEE Journal of* 38, 837-843 (2002).
- T. J. Karle, D. H. Brown, R. Wilson, M. Steer, and T. E. Krauss, "Planar photonic crystal coupled cavity waveguides," *Selected Topics in Quantum Electronics, IEEE Journal of* 8, 909-918 (2002).
- P. Sanchis, J. Marti, W. Bogaerts, P. Dumon, D. V. Thourhout, and R. Baets, "Experimental results on adiabatic coupling into SOI photonic crystal coupled-cavity waveguides," *Photonics Technology Letters, IEEE* 17, 1199-1201 (2005).
- D. O'Brien, M. D. Settle, T. Karle, A. Michaeli, M. Salib, and T. F. Krauss, "Coupled photonic crystal heterostructure nanocavities," *Opt. Express* 15, 1228-1233 (2007).
- J. Jágerská, N. Le Thomas, V. Zabelin, R. Houdré, W. Bogaerts, P. Dumon, and R. Baets, "Experimental observation of slow mode dispersion in photonic crystal coupled-cavity waveguides," *Opt. Lett.* 34, 359-361 (2009).
- J. Jágerská, H. Zhang, N. Le Thomas, and R. Houdré, "Radiation loss of photonic crystal coupled-cavity waveguides," *Applied Physics Letters* 95, 111105-111103 (2009).
- N. Matsuda, T. Kato, K.-i. Harada, H. Takesue, E. Kuramochi, H. Taniyama, and M. Notomi, "Slow light enhanced optical nonlinearity in a silicon photonic crystal coupled-resonator optical waveguide," *Opt. Express* 19, 19861-19874.
- H.-C. Liu, and A. Yariv, "Designing coupled-resonator optical waveguides based on high-Q tapered grating-defect resonators," *Opt. Express* 20, 9249-9263.
- Y. Kawaguchi, K. Saitoh, and M. Koshiba, "Analysis of leakage losses in one-dimensional photonic crystal coupled resonator optical waveguide using 3-D finite element method," *Lightwave Technology, Journal of* 28, 2977-2983.
- A. Martínez, J. García, P. Sanchis, F. Cuesta-Soto, J. Blasco, and J. Martí, "Intrinsic losses of coupled-cavity waveguides in planar-photonic crystals," *Opt. Lett.* 32, 635-637 (2007).

- M. L. Povinelli, and S. Fan, "Radiation loss of coupled-resonator waveguides in photonic-crystal slabs," *Applied Physics Letters* 89, 191114-191113 (2006).
- D. P. Fussell, and M. M. Dignam, "Engineering the quality factors of coupled-cavity modes in photonic crystal slabs," *Applied Physics Letters* 90, 183121-183123 (2007).
- T. Tanabe, M. Notomi, E. Kuramochi, A. Shinya, and H. Taniyama, "Trapping and delaying photons for one nanosecond in an ultrasmall high-Q photonic-crystal nanocavity," *Nat Photon* 1, 49-52 (2007).
- J. Vuckovic, M. Loncar, H. Mabuchi, and A. Scherer, "Optimization of the Q factor in photonic crystal microcavities," *Quantum Electronics, IEEE Journal of* 38, 850-856 (2002).
- J. Ma, L. J. Martínez, and M. L. Povinelli, "Optical trapping via guided resonance modes in a Slot-Suzuki-phase photonic crystal lattice," *Opt. Express* 20, 6816-6824 (2012).
- Y. Xu, R. K. Lee, and A. Yariv, "Propagation and second-harmonic generation of electromagnetic waves in a coupled-resonator optical waveguide," *J. Opt. Soc. Am. B* 17, 387-400 (2000).
- A. Taflove, *Computational Electrodynamics: the Finite-Difference Time-Domain Method* (Artech House, Boston, 1995).
- A. R. A. Chalcraft, S. Lam, D. O'Brien, T. F. Krauss, M. Sahin, D. Szymanski, D. Sanvitto, R. Oulton, M. S. Skolnick, A. M. Fox, D. M. Whittaker, H. Y. Liu, and M. Hopkinson, "Mode structure of the L3 photonic crystal cavity," *Applied Physics Letters* 90, 241117-241113 (2007).

Appendix:

Force Calculation in Time Domain

The Maxwell stress tensor (MST) is a general formalism which allows to calculate the force exerted on an object for a given electromagnetic field distribution. To evaluate optical force exerting on a component, the MST is numerically integrated over a closed surface surrounding the object:

$$F_\alpha = \oint_S \sum T_{\alpha\beta} n_\beta da \quad (\text{A-1})$$

where α and β indicate direction x , y or z , \mathbf{n} is the outward normal to the closed surface S , and the stress tensor,

$$T_{\alpha\beta} = \epsilon E_\alpha E_\beta + \mu H_\alpha H_\beta - \frac{1}{2} \delta_{\alpha\beta} (\epsilon \mathbf{E} \cdot \mathbf{E} + \mu \mathbf{H} \cdot \mathbf{H}) .$$

To calculate the stress tensor $T_{\alpha\beta}$, full electromagnetic field distributions are needed, which can be obtained from an appropriate full-vectorial electromagnetic solver. We show an example of using a FDTD solver and the MST method to solve for optical force on polystyrene particle by the enhanced light of guided resonance mode in Slot-Suzuki-phase lattice. An artificial surface is taken to enclose the polystyrene nanoparticle. As shown by Figure A-1, here an integration cube is taken with 20 nm away from the particle (refractive index~1.60). It is highly recommended to check *if the calculated force was significantly varied with different integration surface*. A force dependence on surface indicates questionable modeling.

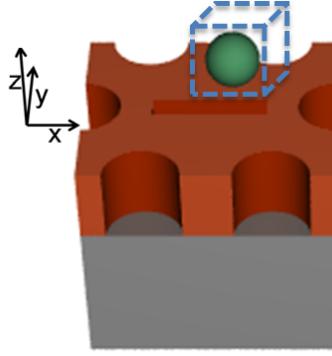


Figure A-1 Schematic of one unit cell of Slot-Suzuki-phase lattice. A cube is taken enclosing the particle as marked by blue dashed lines for integrating the Maxwell Stress tensor.

Optical forces are correlated with optical performance. As a starting point, the device without particles are simulated to get an idea of critical optical performance including resonance wavelength, quality factor and mode profile. A test of mesh size should be conducted to check how parameters converge. Generally speaking, finer meshes are favorable for more accurate calculation in the cost of computational resource. By convergence test, a reasonable mesh size could be decided to achieve acceptable results without occupying too much resource.

For force calculation, a particle is included in the computational cell. Finer meshes are required in the region of the particle and small features like slots in the device. In this case, it is advantageous to use a FDTD package which can define un-uniform meshes. One FDTD implementation, Lumerical, is applied in our modeling for force calculation of particles with radius of 25 nm.

Light distribution varies with wavelength, and thus, optical force is dependent on wavelength. Using frequency-domain solver, a group of calculations are needed to scan over the wavelength of interest. By using time-domain solver like FDTD, we can obtain the entire frequency spectrum

of force in a single simulation, by Fourier-transforming the response to a short pulse. The frequency resolution is decided by the total running time. For narrow-bandwidth features like high-Q resonance, FDTD simulation needs to be run by long time to accurately compute the fields and forces. If the resonance is excited by achromatic light source with different frequencies, force at each frequency contributes to the effective force.

For high-Q resonance mode, it is convenient to perform the force calculation in the *time domain* rather than the frequency domain. In FDTD, we excite the mode using a dipole source inside the slab. For efficient excitation, the bandwidth of the dipole source is larger than the resonance linewidth. A couple of dipole sources may be positioned at positions with expected strongest intensity. To have an idea of the mode profile, an eigenmode solver, e.g. MPB or GME, can be used before FDTD calculation. After the source is tuned off, the fields in the resonator start to decay. The decaying rate can be described by quality factor Q. The instantaneous electromagnetic fields on the *integration cube* are recorded for several optical periods. Equation (A-1) is utilized to calculate the time-dependent force. Typically, the time scale for mechanical response is longer than the optical period, and the time-averaged force over the optical periods may be considered. No long running time is needed. Another advantage of time-domain method is that all frequency components are taken into account for force calculation.

The force can be normalized over electromagnetic field energy U . After the source is tuned off, the instantaneous electromagnetic fields in the *unit cell* are recorded for several optical periods. The time-dependent field energy is calculated by taking the volume integration over the unit cell:

$$U = \frac{1}{2} \iiint_V dV \left(\epsilon(x, y, z) |E(x, y, z)|^2 + \mu_o |H(x, y, z)|^2 \right) \quad (\text{A-2})$$

The time-averaged energy over the optical periods can be calculated, and the corresponding F/U is obtained.

The force can also be normalized by emission power $P=\omega U/Q$.

$$\frac{F}{P} = \frac{F}{U} \times \frac{Q}{\omega} \quad (\text{A-2})$$

In steady state, the emission power is equal to incident power. The F/P can be calculated by the value of F/U and Equation (A-3).

Manipulating Nanowires by Optical Forces

In the thesis, different configurations have been discussed to achieve optical forces to either reposition waveguides, resonators and nanoparticles. It will be also interesting to manipulate nanowire arrays and tune optical performance by optomechanical effects.

Nanowire arrays, as shown by Figure A-2, is a 2D grating structure. It is known that when light is normally incident upon a 1D- or 2D-periodically patterned structure, it can excite guided resonance modes with increased electromagnetic field intensity within the grating. It is expected that the enhanced field intensity between two closely-positioned nanowires will give rise to an optical force on the nanowires.

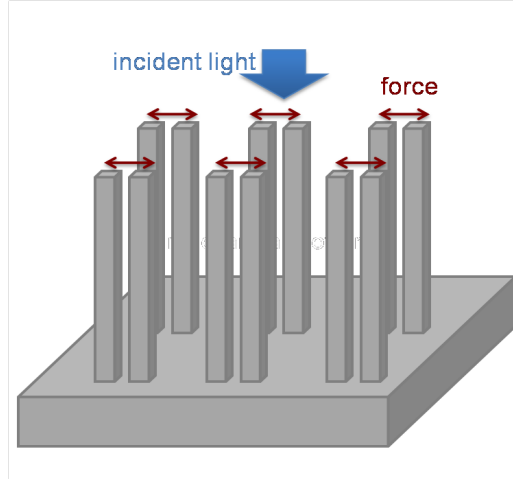


Figure A-2 Schematic of square-lattice nanowire arrays standing on substrate. In each unit, there are two closely-positioned nanowires. Assume the material is InP. Light is normally incident into the array from free space.

An example design is shown in Figure A-3 (a). For simplicity, one unit cell is plotted. An air gap of 68 nm is between two nanowires with dimensions of $135 \times 135 \times 2700 \text{ nm}^3$. Assume the material is InP. The transmission spectrum (black curve in Figure A-3 (b)) is calculated by three-dimensional FDTD method. Guided resonance modes are identified by transmission dips imposed on Fabry-perot fringes. The optical force as function of wavelength is plotted by the red curve in Figure A-3 (b). The force is calculated by Maxwell Stress Tensor method. It is notable that force magnitude is significantly enhanced on guided resonance, especially for the resonance mode at 1550 nm. The negative sign means an attractive force. Figure A-3 (c) shows a side view of the E_x -component distribution at wavelength 1550 nm. Note that the field intensity is enhanced in the air gap. It is expected the field confinement will generate large optical force on both nanowires.

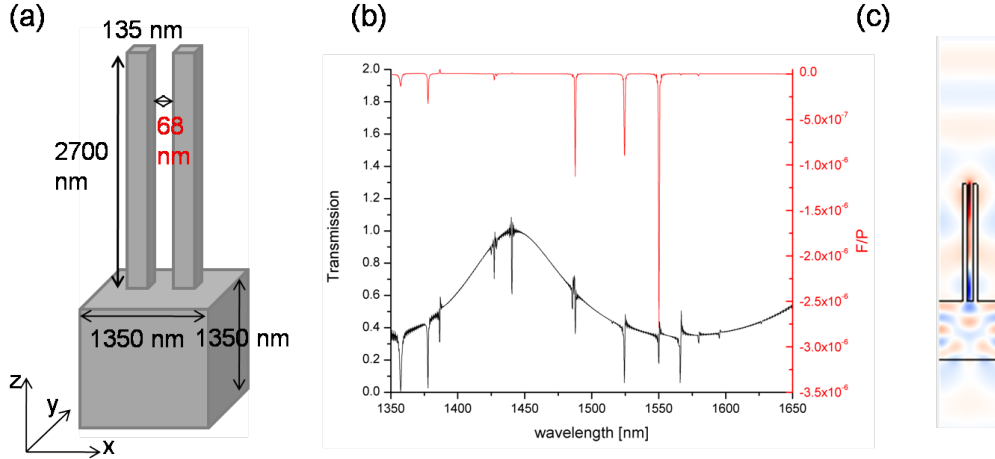


Figure A-3 (a) Schematic of one unit cell. Dimensions are as given. The air gap between two nanowires is 68 nm. (b) Transmission (black curve) for normal incidence. Guided resonance modes are identified by transmission dips imposed on Fabry-perot fringes. Force spectrum (red curve) in the same wavelength window. (c) Side view. The blue and red color are for the E_x component.

If 1550-nm laser light is normally incident with power of 1 mW per unit cell, the optical force is around -2 nN on each nanowire, causing a maximum bending of 2 nm at the nanowire top. The transmission spectrum can be modified by adjusting air gap. With the air gap reduced by 2 nm, the resonance wavelength will be red shifted by around 0.3 nm, one third of the resonance linewidth. Larger change in the air gap is desirable for easier optical probing by reading transmission shift. For fixed input power, larger displacements can be obtained by modulating the incident optical power at the mechanical resonance frequency.

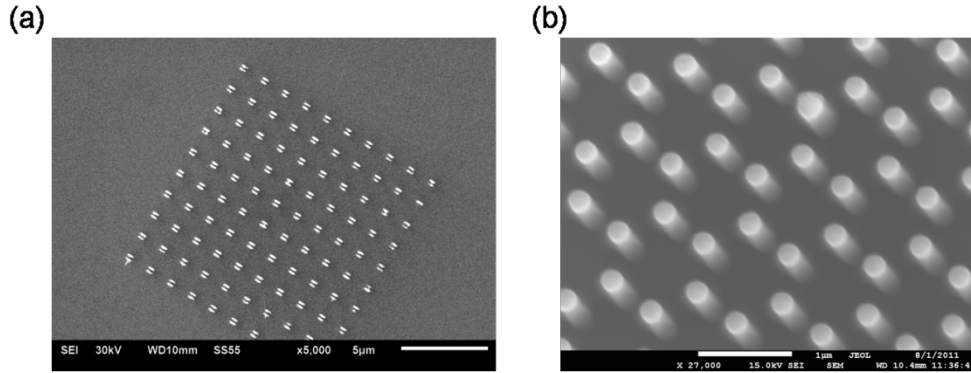


Figure A-4 SEM image of top-down fabricated silicon (a) square lattice of nanowires, and (b) graphite lattice of nanowires.

Nanowires can be fabricated by top-down method. An array of 600-nm-tall silicon nanowires have been fabricated using e-beam lithography and inductively-coupled plasma reactive ion etching (ICP-RIE). We use a 2-μm thick silicon layer on top of a 2 μm silica layer (Ultrasil). The sample was spin-coated at 3000 rpm with HSQ (XR-1541), a negative e-beam resist. Using Raith150 e-beam system, a square-lattice pattern has been exposed with an acceleration voltage of 30 KV and dose of 2000 $\mu\text{A}\cdot\text{s}/\text{cm}^2$. The sample is developed in NaOH (1 wt%) / NaCl (4 wt%). The pattern is transferred from the resist to the silicon layer by an ICP-RIE machine using a gas mixture $\text{SF}_6/\text{C}_4\text{F}_8$. HSQ is very sensitive to temperature and moisture. It is highly recommended to prepare, exposure and develop quickly. HSQ requires longer e-beam exposure time than PMMA. Under our etching conditions, the etching selectivity of HSQ over Si is 1:8.5. Figure A-4 (a) and (b) respectively show a square lattice and graphite lattice of nanowire arrays.

